

DEPOSITIONAL ENVIRONMENTS, DIAGENESIS, AND RESERVOIR DELINEATION
OF THE FCU 1947 UPPER CLEAR FORK CORED INTERVAL
– AN SEM IMAGE ANALYSIS APPROACH TO
PORE SYSTEM CHARACTERIZATION

by

TORE RAY WIKSVEEN

Presented to the Faculty of the Graduate School of
The University of Texas at Arlington in Partial Fulfillment
of the Requirements
for the Degree of

MASTER OF SCIENCE IN GEOLOGY

THE UNIVERSITY OF TEXAS AT ARLINGTON

DECEMBER 2013

Acknowledgements

I would first like to thank XTO Energy for granting me the resources, both tangible and intangible, to conduct and complete this study. My time at XTO Energy has brought me a wealth of knowledge and experience. I am indebted to the company and my mentors for all they have provided me with. Particularly, I'd like to thank Wayne R. Gibson and Jason P. Slayden, who have both been close by my side, providing assistance and guidance throughout this study.

I would like to thank John Wickham, Merlynd Nestell, and Qinhong Hu at the University of Texas at Arlington, for providing me counsel and direction over the course of my graduate studies. Several students at University of Texas at Arlington are also to be thanked for their support and ability to keep me moderately sane. Jillian Rowley, Paul Monahan, Johnathon Bogacz, and Shariva Darmaoen have been instrumental in keeping me motivated during defeating times.

Most importantly, I would like to thank my mom, dad, sister Karissa Plusko, brother Randy Hosey, and Rene Finical. The emotional support, love, and selflessness they have provided has allowed me to thrive in any endeavor I have pursued. I could not have finished this study without them.

November 21st, 2013

Abstract

DEPOSITIONAL ENVIRONMENTS, DIAGENESIS, AND RESERVOIR DELINEATION
OF THE FCU 1947 UPPER CLEAR FORK CORED INTERVAL
– AN SEM IMAGE ANALYSIS APPROACH TO
PORE SYSTEM CHARACTERIZATION

Tore Ray Wiksveen, M.S.

The University of Texas at Arlington, 2013

Supervising Professor: John Wickham

Delineating reservoir facies in heterogeneous tidal-flat carbonates is a challenge which requires analysis at greater resolutions than wireline logs can provide. Such depositional environments are documented in the upper Clear Fork deposits of Fullerton Field in West Texas. This study examined lithofacies and depositional facies of core to gain understanding of the best reservoir facies. Whole-core examination, Core Laboratories and wireline log analysis, thin section microscopy and SEM image analysis were used to delineate reservoirs.

Subtidal facies were deemed the poorest of reservoirs because compaction, anhydrite plugging, and burial diagenesis obliterated pore space. Intertidal facies were determined as the best reservoirs, particularly those directly beneath shallowing-upwards cycle tops. Grainier fabric and fabric selective dissolution of these facies increased porosity. Supratidal facies were determined as the second best reservoirs because eogenetic dolomitization protected them from compaction. Furthermore, these depositional facies can be correlated to nearby wells via distinct wireline signatures.

Table of Contents

Acknowledgements	ii
Abstract	iii
Table of Figures	vii
Chapter 1 Introduction.....	1
Purpose	1
Nomenclature Disclaimer	2
Previous studies	2
Methods	4
Core and Thin Sections	5
Pore Classification	6
Pore Quantification and Analysis	6
Borehole Logs and the Segregation of Cored Interval	10
Chapter 2 Geological Setting	12
Paleogeography.....	12
Tectonic Evolution and Basin Filling.....	13
Stratigraphy	16
Depositional Environment.....	21
Study Location	24
Chapter 3 Analysis of Fullerton 1947 Core	28
Core Interpretation.....	28
Results.....	30
Discussion	33
Depositional Model	52
Core Laboratories Analysis of Reservoir Properties	54

Porosity Analysis Results	54
Porosity Analysis Discussion.....	55
Permeability Analysis Results	57
Permeability Analysis Discussion	58
Grain Density Analysis Results	59
Grain Density Analysis Discussion	59
Chapter 4 Microscopic Examination	61
Thin Section Examination.....	61
Results.....	61
Discussion	63
Diagenetic History of FCU 1947 Core	72
Results.....	72
Discussion	75
Chapter 5 Porosity	81
Pore Types	81
Results.....	81
Discussion- Major Pore Types	81
SEM Image Analysis.....	91
Results.....	91
Discussion	102
Limitations and Considerations	109
Chapter 6 Reservoir Exploitation	114
Wireline Log Responses.....	114
Results.....	114
Discussion	117

Perforation Targets and Completions Practices	118
Results.....	118
Discussion	119
Chapter 7 Conclusions.....	124
Appendix A Thin Section Data	129
Appendix B SEM Image Analysis Data.....	151
References.....	171
Biographical Information	181

Table of Figures

Figure 1: Flowchart of SEM image analysis methodology.....	7
Figure 2: Middle Permian paleogeographic map with field outline. Dark blue colors are oceans and deep seas. Light blue colors represent shallow seas. Tan/Brown colors represent terrestrial environments. Modified from Blakey (2013).....	13
Figure 3: (A) Main structural provinces of the Permian Basin. Modified from Frenzel et al. (1988). (B) Major Fault Trends of the Permian Basin. Modified from Yang and Dorobek (1995).....	15
Figure 4: Stratigraphic chart of respective Leonardian stage of the Lower Permian (Cisuralian) Series. Yellow box highlights interval of study. Modified from Ruppel and Jones (2004).	17
Figure 5: Illustration of Leonardian sequences in neighboring North Robertson Field. Modified from Atchley et al. (1999).	20
Figure 6: Illustration of changing Fullerton Field environments and their resultant stratigraphic stacking patterns during upper Clear Fork deposition. Modified from Silver and Todd (1969).....	23
Figure 7: Structural map of the upper Clear Fork and well location. Structural depths are in feet below sea level. Star shows the position of well FCU 1947 and circles represent the wells shown in the cross section. Yellow is the unitized field area (XTO Energy, 2013).	25
Figure 8: Stratigraphic cross section of FCU 1947 and nearby wells. Cross section is hung on the top of the upper Clear Fork, which is the base of sub-interval A in this study (XTO Energy, 2013).	26

Figure 9: Structural cross section of FCU 1947 and nearby wells. Black number above well corresponds to well number, green corresponds to KB elevation (XTO Energy, 2013).	27
Figure 10: Core photograph of rudstone from depth 6129'. Notice the mud intraclasts probably transported from nearby environments.	38
Figure 11: Core photograph of burrow or root structures at depth 6129' MD.	39
Figure 12: Core photograph of non-parallel algal mats at depth 6128'.	40
Figure 13: Core photograph of a large anhydrite nodule, a diagenetic feature, and heavily altered depositional facies (depth of 6106').	41
Figure 14: Core photograph of recrystallized mudstone/wackestone facies from the bottom of sub-interval C displaying well developed stylolites.	42
Figure 15: Skeletal packstone/grainstone facies suggesting a high-energy beach face environment.	43
Figure 16: Core photograph (6050') documenting abrupt change from organic rich mudstone (bottom) to supratidal, grain (fine) rich wackestone.	44
Figure 17: Core photograph of pyrite nodule in organic rich shaley mudstone. Pyrite nodule is an indication of anoxic conditions, like a result of lagoonal starvation where algal mats could grow but carbonate production is limited.	45
Figure 18: Core photograph of diapiric anhydrite (6038').	46
Figure 19: Core photograph of prominent mudcracks indicating desiccation (6023').	47
Figure 20: Core photograph of algal mat with interbedded dolomite and nodular anhydrite (6021').	48
Figure 21: Core photograph of red/brown silty dolomite with wispy laminations indicating oxidizing conditions (6016').	49

Figure 22: Core photograph of algal mat overlain by a thin organic rich siltstone and capped by bedded and chicken-wire anhydrite. Diagnostic features of transition from intertidal to supratidal depositional realm.....	50
Figure 23: Core photograph of nodular anhydrite in a red/brown silty dolomite (6015')...	51
Figure 24: Depositional model of the Fullerton Field as determined from core analysis. .	53
Figure 25: Bar chart of average porosity for each sub-interval.....	55
Figure 26: Bar chart of average permeability for each sub-interval.....	58
Figure 27: Bar chart of average grain density values for each sub-interval.	59
Figure 28: Thin section analysis results. Ms = Mudstone, Ws = Wackestone, Ps = Packstone.	62
Figure 29: Photomicrograph of supratidal facies displaying fine skeletal grains and mudcracks. Sample A1-6042 - 12.5x CPL. Arrow indicates stratigraphically up.....	64
Figure 30: Photomicrograph of sample L1-6125. Mottled fabric of intertidal deposits. 40x PPL – Diameter of field of view is 4 mm.	66
Figure 31: Photomicrograph of finely laminated intertidal deposits bound by an algal mat. Sample L3-6134. 40x PPL – Diameter of field of view is 4 mm. Blue colors indicate pore space.....	67
Figure 32: Photomicrograph of intertidal facies with micritized peloids and skeletal grains. Sample I2-6120. 100x CPL – Diameter of field of view is 2 mm.	68
Figure 33: Photomicrograph of stylolites in subtidal facies. Formation of stylolites in crystalline dolomite matrix indicates mechanical compaction and pressure dissolution. Sample G3-6099. 40x PPL – Diameter of field of view is 4 mm.	70
Figure 34: Microphotograph of subtidal facies with black conodont P element (dark blue oval) in a planar subhedral dolomite matrix. High birefringence colors are pore filling (red	

circle) and poikilotopic anhydrite (yellow circle). Sample E2-6073 40x CPL – Diameter of FOV is 4 mm.	71
Figure 35: High magnification image of subtidal subhedral/euhedral matrix. Dolomite rhombs are approximately 2 μm in diameter. Sample G2-6090. 200x CPL. Arrow points to depositional orientation.	72
Figure 36: Diagenetic history of the upper Clear Fork determined from cross cutting relationships.. The different stages are explained in chapter 5. Similar to work from Montgomery (1998).	74
Figure 37: Photomicrograph of pore filling anhydrite (high birefringence colors) in a dolomite matrix. The anhydrite occludes much of the secondary pore space. Sample G2-6090. 12.5x CPL. Arrow indicates stratigraphically up.	79
Figure 38: SEM photo of grain and peloid dissolution molds. Green is pore space. Sample C2-6053 at 75x magnification. Dark black areas were determined to be pore filling anhydrite.	83
Figure 39: SEM photo sample of moldic pore with dolomite cement rhombs lining pore walls. Sample C1-6052 at 750x. In some cases the pore is nearly completely occluded by dolomite or sulfate cement. Pore space is green.	84
Figure 40: Photomicrograph of partial dissolution of grains and later stage obliteration of shelter porosity within a foraminifera test by dolomite cryptocrystalline cement sample. Pore space is blue. Sample B1-4046 PPL 100X.	85
Figure 41: Photomicrograph of moldic porosity partially reduced by dolomite cement in multiple stages. Red grain in right center of photo is calcite (Alizarin stain), suggesting preferential dissolution of grains. Sample B2-6048 CPL 200x. Pore space is black.	86

Figure 42: SEM photo of intercrystalline matrix porosity and fracture filaments. Green is pore space. Sample E1-6069 at 750x. Matrix porosity nearly invisible using optical microscopy.	87
Figure 43: SEM photo of solution enlarged vugs (larger) and intercrystalline porosity (smaller pores). Sample G1-6084 at 75x magnification. Darker black areas determined to be pore filling anhydrite.	88
Figure 44: Photomicrograph displaying complex pore evolution. Pore space (blue) originated as a fenestral pore enlarged by meteoric solutions during early burial then reduced by dolomite cement during at least two different time intervals (small and large dolomite rhombs). Sample L3-6134 200x PPL.	89
Figure 45: Crossplot of SEM porosity versus gas expansion Helium porosity.	93
Figure 46: Image analysis porosity results. Highlighted cells indicate samples with equal to or greater than 0.03 md permeability.	94
Figure 47: Pore size distributions from A1-6042, B1-6046, B2-6048, C1-6052, C2-6053, C3-6054. A1-6042 has a different vertical scale to fit bar chart.	95
Figure 48: Pore size distributions from subtidal samples E1-6069, E2-6073, G1-6084, G2-6090, G3-6099.	96
Figure 49: Pore size distributions from I1-6116, I2-6120, I3-6143, K1-6117, K2-6126. K1-6117 has different vertical scale.	97
Figure 50: Pore size distributions from intertidal samples L1-6125, L2-6127, L3-6134, M1-6128, M2-6137.	98
Figure 51: Crossplot of permeability versus overall pore shape parameter (\bar{y}).	99
Figure 52: Crossplot of permeability versus macropore shape parameter (\bar{y}).	99
Figure 53: Crossplot of permeability versus micropore shape parameter (\bar{y}).	100
Figure 54: Crossplot of permeability versus (SEM) total porosity.	100

Figure 55: Crossplot of permeability versus (SEM) macroporosity.	101
Figure 56: Crossplot of permeability versus (SEM) microporosity.	101
Figure 57: SEM photo of round pores with low $\bar{\gamma}$ values. Sample B1-6046 at high magnification (750x) displaying moldic pores (green). This sample has a $\bar{\gamma}$ value of 2.0 for both micropores and macropores.	105
Figure 58: SEM photo of intercrystalline pores which have higher $\bar{\gamma}$ values. Sample A1-6042 at high magnification (750x). This sample has a $\bar{\gamma}$ value of 3.9 for micropores and 2.0 for macropores (not in field of view).	106
Figure 59: Crossplot of Helium porosity and SEM porosity. Samples with less than 0.03 millidarcies were omitted which dramatically increased the r^2 coefficient.	110
Figure 60: Core photograph of homogenous lithology. Sample E2-6073 which contains very similar SEM and whole-core helium porosity values.	112
Figure 61: Wireline log responses and core analysis measurements of the FCU 1947 cored interval (XTO Energy, 2013).	116
Figure 62: Proposed perforation intervals for FCU 1947. Red rectangle outlines suggested perforation interval directly below a shallowing upwards cycle top. Secondary perforation interval is the orange rectangle (XTO Energy, 2013).	122
Figure 63: Suggested perforation intervals in structural cross section of FCU 1947 and nearby wells (XTO Energy, 2013).	123

Chapter 1

Introduction

Purpose

The complexity and heterogeneity of carbonate reservoirs makes the exploitation of their resources both a geological and engineering challenge. Discovered in 1942, the Fullerton Field of West Texas is no exception to these challenges. The Wichita Formation and the lower part of the Clear Fork Group are the primary producing zones in the field. The field covers 29,000 acres and is located 20 miles northwest of Andrews, TX (Bane et al., 1994). The field has an estimated original oil in place of between 1.6 and 1.9 billion stock tank barrels (BSTB) and, as of 2012, had only produced around 310 million barrels (XTO Energy Estimates, 2012). The ratio of recovered oil to original oil in place yields a recovery factor of around 19%, which is remarkably low in comparison to other Clear Fork producing reservoirs on the Central Basin Platform (CBP). Low recovery efficiencies can be related to an array of attributes but are generally believed to be a reflection of complex carbonate heterogeneity as well as poor log resolution.

Oil production from the lower Clear Fork and Wichita reservoirs has declined from the peak production of 44,000 BOPD in 1948 to only 3,850 BOPD as of 2012 (Bane et al., 1994; XTO Energy Estimate, 2012). Considering these steady declines, the current operator, XTO Energy, is looking for bypassed potential within the unitized area. This study aims to evaluate the reservoir characteristics with an emphasis on porosity attributes and vertical stacking patterns of the upper Clear Fork interval in well *FCU 1947*. By examining core, thin sections, and applying SEM image analysis of pore systems, depositional facies and lithofacies could be studied in relation to their vertical successions. Understanding these reservoir characteristics will help to exploit the oil reserves within the upper Clear Fork and to maximize recovery efficiency of the studied

well and its neighboring offset wells. Furthermore, characterization of the interval will help guide future work into a field wide study. New technologies and reduced costs of work-over well operations and completions make this study even more desirable.

Nomenclature Disclaimer

Throughout this study, the terms “upper Clear Fork formation”, “upper part of the Clear Fork formation”, “lower Clear Fork formation”, “lower part of the Clear Fork formation”, and “Tubb formation” are used. However, the upper, lower and Tubb sand portions of the Clear Fork Group, have not been formally divided into the lithostratigraphic unit of “Formations” and should therefore not be formally named as so. The informal nomenclatures are used frequently by the oil and gas industry and have also gained routine acceptance in work by Silver and Todd (1969), Mazzullo (1982, 1995), Bane et al. (1994), Atchley et al. (1999), Ruppel (1992, 2002), Ruppel and Ariza (2002), Ruppel and Jones (2006), as well as Harrington and Lucia (2011).

To overcome nomenclature inaccuracy of the upper, lower and Tubb portions of the Clear Fork Group, a lower case “f” for formation, as well as a lower case “l” or “u” for lower and upper, were used. By not capitalizing “lower”, “upper” or “formation”, this study accepts that these lithostratigraphic units are not formal subdivisions and should not be capitalized as so. Furthermore, any mentions of other informal formations throughout this study are also spelled with a lower case “f”.

Previous studies

Geologically, the Clear Fork Group has not been studied in depth due to limited outcrops of a section encompassing the entire group. Rather, the informal subdivisions of the group have been studied at varying locations throughout the Permian Basin. The depositional systems and stratigraphy of the lower Leonardian Abo and Wichita Formations of the Wichita Group and the lower part of the Clear Fork Group were studied

by Mazzullo (1982) in the northern part of the Midland Basin. Upper Leonardian facies from the Texas panhandle were found by Presley and McGillis (1982) to be predominantly evaporites, interbedded with dolomites. Outcrop equivalents of Clear Fork reservoirs in the Sierra Diablo Mountains of West Texas were studied by Ruppel et al. (2000).

Because the upper part of the Clear Fork Group (upper Clear Fork formation) is an economically valuable reservoir in many fields on the Central Basin Platform (including Goldsmith, Flanagan, Riley, Robertson, and other smaller fields), much attention has been given to its characterization. Lucia (1972) studied the carbonate shoreline facies within the upper Clear Fork interval from both of the Flanagan and Robertson Fields. The subsurface study provided detailed descriptions of upper Clear Fork deposits in the fields which are approximately 20 and 25 miles north-northwest of Fullerton. More recently, a host of studies have revisited the upper Clear Fork reservoirs of these fields, with nearby fields showing remarkably different characteristics (Montgomery, 1998; Atchley et al., 1999; Ruppel, 2002, 2004, 2006). Ruppel (1992, 2002) and Atchley et al. (1999) also studied diagenesis, facies and cyclicity of the upper Clear Fork interval and the Glorieta Formation at both Monahan and Robertson Fields.

The Fullerton Field itself has been studied extensively since the initial discovery in 1942 (Bane et al., 1994; Lucia et al., 2006; Ruppel and Jones, 2006; Harrington and Lucia, 2011). In addition, the Bureau of Economic Geology received a contract from the Department of Energy to study the Fullerton Field and other carbonate reservoirs from 2001-2004 (Ruppel, 2004). However, within the Fullerton Field, most attention was directed at the lower Clear Fork and Wichita reservoirs. The upper Clear Fork was almost entirely omitted from these studies. An extensive search of literature pertaining to the

upper Clear Fork interval within the Fullerton Field returned little results with only a brief mention of the upper Clear Fork interval with conflicting descriptions.

Methods

The data to model carbonate reservoirs includes the spatial distribution of pores, saturation fluids of pores, and connectivity of pores (Lucia et al., 2003). Complex carbonate pore systems require analysis at varying resolutions ranging from macroporosity ($>500 \mu\text{m}^2$) to microporosity ($<500 \mu\text{m}^2$). The quantification of these varying pore sizes and their connectivity can help explain variations in permeability in carbonate samples with a variety of pore structures (Anselmetti et al., 1998).

The use of core and thin sections with digital image analysis at varying magnifications provided data of pore measurements which were then evaluated statistically. The characterization of the pore measurements were correlated with varying lithofacies of the interval. Using these methods, productive and non-productive reservoirs can be distinguished within the cored interval. Additionally, the vertical continuity of the reservoirs and their depositional sequences could be determined. A general outline of methodology for this study is listed below.

1. Divide cored interval into sub-intervals based on wireline log responses of overall shifts in depositional environments.
2. Examine and describe core macroscopically to determine depositional sequence (from vertical stacking patterns), depositional facies and lithofacies.
3. Determine dominant depositional facies for each sub-interval.
4. Examine and describe core analysis of reservoir properties measured by Core Laboratories.
5. Fabricate thin sections from repeating lithofacies and depositional facies.

6. Microscopically examine and describe thin sections to qualitatively understand pore properties and connectivity with respect to lithofacies, depositional facies, and diagenetic history.
7. Use SEM Image analysis to quantitatively characterize porosity with respect to depositional facies and lithofacies.
8. Determine ideal sub-interval(s) target(s) for reservoir exploitation based on macroscopic, microscopic, and SEM findings.

Core and Thin Sections

Core descriptions were carried out using Dunham's classification scheme (Dunham, 1962). A 10x hand lens and a low-powered binocular microscope were used to describe the dominant lithofacies for each foot (12 inches), for the entire length of the core, totaling 130 feet. A detailed log showing the cored interval for well FCU 1947, as well as petrophysical measurements, can be seen in Figure 7. After careful examination of the core, intervals of similar rock characteristics were lumped into 14 lithofacies based on their attributes. Attributes include: Dunham's (1962) classification, mineralogy, grain size, angularity, cement, fossil content, matrix, color, and sedimentary structures.

Twenty-one standard thin sections from 9 of the 14 lithofacies were fabricated. Several thin sections were made for each of the representative lithofacies. Alizarin red stain was applied to the thin sections to differentiate dolomite from calcite. The thin sections were also impregnated with blue epoxy to highlight porosity. Furthermore, the sections were highly polished for SEM analysis using 1 μ m grit. A petrographic microscope was used to describe all 21 thin sections in both plain and cross polarized light.

Pore Classification

Pores in carbonate rocks can generally be divided into primary and secondary types, based on the timing of porosity formation (Choquette and Pray, 1970). Primary pores are depositional in nature and include: interparticle, intercrystal, intraparticle, intracrystal, fenestral, shelter, and growth framework. Secondary pores are formed post-depositional and include: modified primary types, pores created by dissolution occurring after deposition, vugs and dissolution-enlarged fractures. In this study, the classification and nomenclature scheme presented by Choquette and Pray (1970) was used to describe pore types. Pore types were described and classified for each lithofacies. The pore types helped to qualitatively understand permeability, porosity evolution, diagenetic history, and depositional environment.

Pore Quantification and Analysis

Porosity quantification via digital image analysis has been employed in several previous studies (Ehlich et al., 1984, 1991a, 1991b; McCreesh et al., 1991; Gerard et al., 1992; Anselmetti et al., 1998) and has become a well-established method. Slightly modified from work by Anselmetti et al. (1998), porosity data acquisition, quantification, and analysis was followed as outlined (Figure 1):

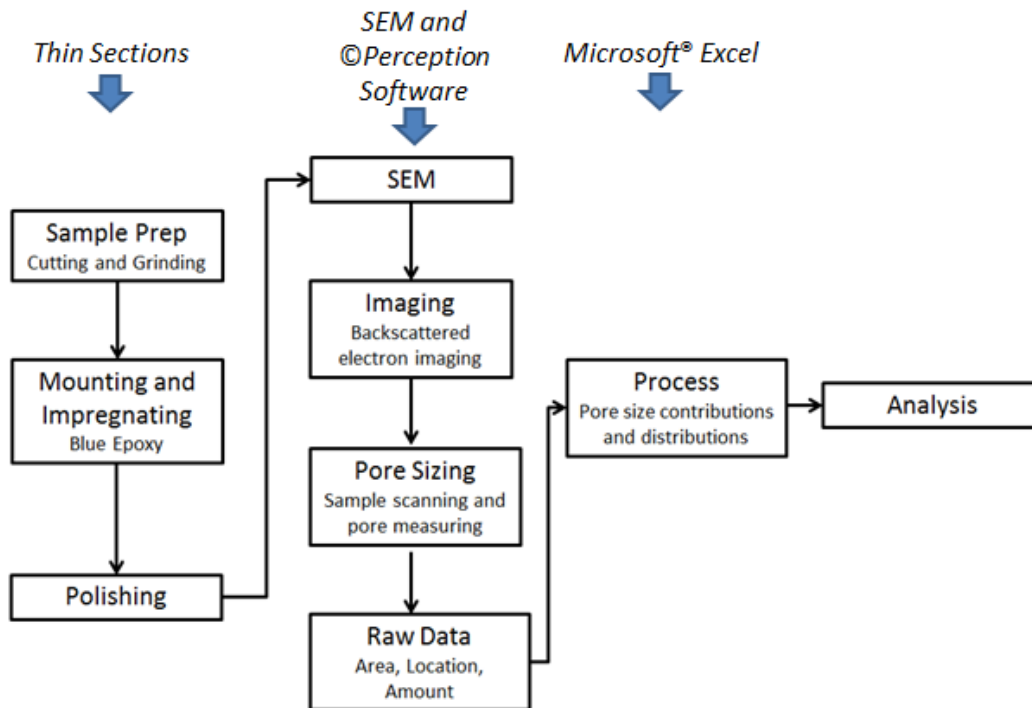


Figure 1: Flowchart of SEM image analysis methodology.

- 1.) Using epoxy impregnated thin sections, samples were inserted into a SEM. The SEM was run at high gain under variable pressure, similar to an ESEM (environmental scanning electron microscope). The benefit of using a variable pressure SEM is that you do not need to coat the samples in gold.
- 2.) Thin sections were scanned for pore space at both high and low magnifications. Pore space was identified by applying a gray level threshold which separated pore space from solid matter. The threshold was studied meticulously for each sample to ensure that pore space was accurately separated from solid matter. Sixteen scanning points (fields of view) across each thin section were selected by the user. Eight points were run at high magnification (750x) to identify micropores, and eight points were run at low

magnification (75x) to identify macropores. The high and low magnification runs were denoted *HMSEM* and *LMSEM*, respectively, in included equations.

3.) Separate stage files were created for the low and high magnification runs. The high magnification stage file was created so scanning software (*©Perception Software*) would not pick up pores with an area of less than $0.5 \mu\text{m}^2$, or greater than $499.9 \mu\text{m}^2$. The low magnification stage file was created so the software would not pick up pores less than $500.0 \mu\text{m}^2$, but had no limit on how large the pores could be. The different stage files were created to ensure pores were not counted twice if a low magnification field of view were to overlap a high magnification field of view. Additionally, the stage files categorized each scanned pore into a pore class, based on their individual area. The six pore classes, each composing one order of magnitude, were : a) $0.5 \mu\text{m}^2 \leq A < 5.0 \mu\text{m}^2$; b) $5.0 \mu\text{m}^2 \leq A < 50.0 \mu\text{m}^2$; c) $50.0 \mu\text{m}^2 \leq A < 499.9 \mu\text{m}^2$; d) $500.0 \mu\text{m}^2 \leq A < 5,000.0 \mu\text{m}^2$; e) $5,000.0 \mu\text{m}^2 \leq A < 50,000 \mu\text{m}^2$; f) $A \geq 50,000 \mu\text{m}^2$, where A = the area of the pore. The first three classes represent micropores, the latter three represent macropores.

4.) All pore area measurements were output from the software into a database (*Microsoft® Excel*) for processing. To calculate microporosity (Φ_{mic}), the total high magnification scanned area ($A_{tot\ HMSEM}$) was divided by the sum of the micropore areas (ΣA_{mic}). To calculate microporosity Equation 1 (below) was used and is written as:

Equation 1

$$\phi_{mic} = \Sigma A_{mic} / A_{tot\ HMSEM}$$

To calculate macroporosity (Φ_{mac}), the total low magnification scanned area ($A_{tot\ LMSEM}$) was divided by the sum of the macropore areas (ΣA_{mac}). To calculate macroporosity Equation 2 (below) was used and is written as:

Equation 2

$$\phi_{mac} = \Sigma A_{mac} / A_{tot\ LMSEM}$$

To calculate total porosity (Φ_{tot}), the microporosity (Φ_{mic}) is added to the macroporosity (Φ_{mac}). To calculate total porosity Equation 3 (below) was used and is written as:

Equation 3

$$\phi_{tot} = \phi_{mic} + \phi_{mac}$$

For greater detail, individual pore class contributions were calculated so pore size distribution could be examined. To determine the porosity contribution of each class (Φ_n), the sum of the area for the individual class (ΣA_n) is divided by the area of the representative total scanned area ($A_{tot\ LMSEM}$ or $A_{tot\ HMSEM}$). To calculate pore size contributions for macropores Equation 4 (below) was used and is written as:

Equation 4

$$\phi_n = \Sigma A_n / A_{tot\ LMSEM}$$

To calculate pore size contributions for micropore classes Equation 5 (below) was used and is written as:

Equation 5

$$\phi_n = \Sigma A_n / A_{tot\ HMSEM}$$

5.) Pore shape analysis was also employed using the data acquired. Along with porosity, pore shape also has a large effect on rock properties, particularly in relation to permeability. To obtain a pore shape (y) for each pore, the perimeter of the pore (P) was divided by the circumference of a circle of the pore area (P'), which becomes dimensionless and normalizes the value such that a perfect circle will equal 1. In theory, an elongate pore will have a higher y than a circular pore. To calculate the shape parameter of each pore Equation 6 (below) was used and is written as:

Equation 6

$$y = P/P' ; \text{ where } P' = 2\sqrt{\pi A}$$

However, a single pore does not have any significant effect on a sample, so the average value of y for a sample was calculated by weighing the individual y by the pore area (A). To calculate the average shape parameter of a sample Equation 7 (below) was used and is written as:

Equation 7

$$\bar{y} = \frac{\sum_i (A_i \times y_i)}{\sum_i A_i}$$

6.) Histograms of pore size distributions were generated and analyzed to characterize the major lithofacies and depositional facies. Crossplots of various attributes with permeability were also created for further analysis. The crossplots include: 1) Permeability vs. Total Porosity; 2) Permeability vs. Microporosity; 3) Permeability vs. Macroporosity; and 4) Permeability vs. Shape Parameter (y).

Borehole Logs and the Segregation of Cored Interval.

Wireline logs used in this study were neutron, density, laterolog (shallow, medium and deep), and spectral gamma ray. Neutron and density logs measure the porosity and density of the rock. Laterologs measure the resistivity of fluids and rock around the sonde and include the mudcake, and the flushed as well as unflushed zones of the formation. Spectral gamma ray measures the radioactivity contributions of Thorium, Potassium, and Uranium.

Water saturation is also displayed in cross sections and in Plate 1; however, it is not a direct measurement from a wireline tool but is calculated from resistivity and porosity measurements using Archie's equation (Archie, 1942). For the purpose of this study, lithofacies from core descriptions were correlated by wireline logs to nearby wells at similar structural position.

For the purpose of this study, the cored interval was divided into 5 sub-intervals. Each sub-interval was bounded by mudstone(s) or siltstone(s) above it, below it both.

The gamma ray tool was used to identify the radioactive deposits, which are interpreted as overall shifts in depositional environments. Therefore, each sub-interval has a dominant depositional facies and general lithofacies.

Chapter 2

Geological Setting

Paleogeography

The area of this study is located within the central portion of the Central Basin Platform (CBP). The CBP is one of four structural provinces that occur in the Permian Basin. Located in West Texas and the southeastern portion of New Mexico, the Permian Basins' four provinces are the Midland Basin in the East, Delaware Basin in the West, Val Verde Basin in the South, and the CBP in the middle which separates all of the sub-basins. The Permian Basin encompasses a total area of about 115,000 square miles (Mazzullo, 1995). A middle Permian paleogeographic reconstruction by Blakey (2013), along with the study location, is illustrated in Figure 2.



Figure 2: Middle Permian paleogeographic map with field outline. Dark blue colors are oceans and deep seas. Light blue colors represent shallow seas. Tan/Brown colors represent terrestrial environments. Modified from Blakey (2013).

Tectonic Evolution and Basin Filling

Prior to the formation of the Permian Basin, the ancestral Tobosa Basin was situated in its place. The moderately shallow feature was postulated by Adams and Keller (1996) to be an intracontinental sag basin. Upper Cambrian to Lower Mississippian strata were deposited there. These strata represent sequences of shallow marine carbonate, with some minor siliciclastic deposits, a total thickness of up to 6,500 feet (Mazzullo, 1995).

The Tobosa Basin started to deform when the incipient Permian Basin began to develop in the Early to Middle Pennsylvanian. Beginning as a passive margin, pre-

existing structural elements were reactivated, forming a sequence of foreland uplifts during the Marathon-Ouachita collision (Atchley et al., 1999). Strong compressional forces from the southern Marathon fold belt produced by plate convergence caused rapid subsidence of the Permian Basin to the north as well as an increase of sedimentation into the basin. The compressional forces along pre-existing, Precambrian fault zones caused propagation of a series of high angle reverse faults, ultimately uplifting the CBP (Mosley, 1990). The collision of the North American plate with the South American plate was part of the late Paleozoic formation of Pangaea. Key structural provinces as well as major fault trends of the Permian Basin are illustrated in Figure 3.

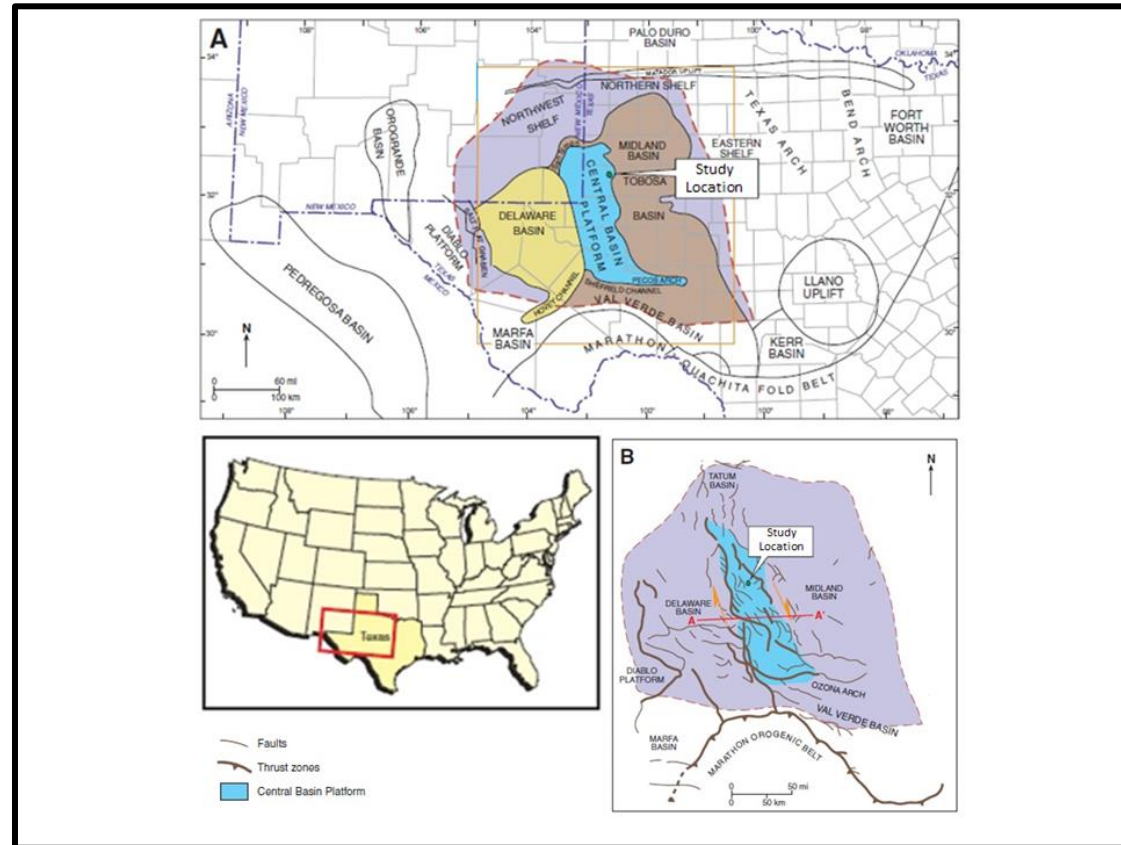


Figure 3: (A) Main structural provinces of the Permian Basin. Modified from Frenzel et al. (1988). (B) Major Fault Trends of the Permian Basin. Modified from Yang and Dorobek (1995).

By the Middle Pennsylvanian, the Permian Basin had been completely segmented by the uplift of the CBP, into the separate Midland and Delaware sub-basins (No Author, 1998). Tectonic activity ceased in the early Permian and was followed by gradual subsidence and the spread of shallow water carbonate platforms around the margins of the basin (Mosley, 1990). Through the Guadalupian, fluctuating sea levels and basin subsidence caused clastic sedimentation as well as carbonate debris flows into the basin from surrounding highs. Turbiditic sedimentation from reefal complexes occurred intermittently between marine carbonate deposition to fill the basin. Turbidity and debris flow sedimentation ceased once topographic highs were eroded to non-positive features. Ochoan time marked the termination of the Permian Basin as the progradation of the carbonate shelves coupled with evaporite deposition caused basin starvation. The evolution and rapid subsidence of the Permian Basin yielded sequences of Permian strata ranging from 4,500-9,500ft on the CBP to as thick as 12,500-24,000ft in the Delaware Basin, and around 5,000ft in the starved Midland Basin (Mazzullo, 1995).

Locally, the Fullerton Field is characterized as a large anticlinal structure that includes two closures named the north dome and the south dome. Tectonic activity within the field ceased before deposition, with faulting and folding occurring between Mississippian to Pennsylvanian time (Bane et al., 1994). Due to this pre-depositional faulting, the Permian strata are draped across the older structures, which give the field both structural and stratigraphic traps.

Stratigraphy

Within North America, four standard series of the Permian system are recognized: Wolfcampian, Leonardian, Guadalupian, and Ochoan, from oldest to youngest. A general stratigraphic chart of the Leonardian Stage of the Lower Permian (Cisuralian) Series and respective strata is shown in Figure 4. Atop the CBP an

unconformity occurs between middle Pennsylvanian and early Permian strata. Erosion and non-deposition are due to uplift of the CBP initiated in the Early to Middle Pennsylvanian, as mentioned previously. Prior to uplift, the thickness of Middle Pennsylvanian and older strata on the platform were similar to thickness of strata in the Delaware and Midland Basins, due to uniform ancestral Tobosa Basin deposition.

SERIES	STAGE	SUBSURFACE			OUTCROP				
		CENTRAL BASIN PLATFORM		NORTHERN SHELF	GUADALUPE MOUNTAINS/ SIERRA DIABLO				
		NEW MEXICO	TEXAS		PLATFORM	MARGIN	SEQUENCE		
Lower Permian	LEONARDIAN	San Andres	San Andres	San Andres	San Andres	Cutoff	Quad 1		
		Glorieta	Glorieta	Glorieta	Glorieta	Victorio Peak	Leo 7-8		
		Paddock	upper Clear Fork	Clear Fork Group	upper Clear Fork		Victorio Peak	Leo 6	
		Blinebry						middle Clear Fork	Leo 5
		Tubb						Tubb	Leo 4
		Drinkard	lower Clear Fork	Clear Fork Group	lower Clear Fork		Victorio Peak	Leo 3	
		Abo	Wichita	Wichita	Wichita	Bone Spring	Leo 2		
			Abo	Abo	Abo		Leo 1		
		Wolfcamp	Wolfcamp	Wolfcamp	Hueco	Hueco	Wolf 3		

Figure 4: Stratigraphic chart of respective Leonardian stage of the Lower Permian (Cisuralian) Series. Yellow box highlights interval of study. Modified from Ruppel and Jones (2004).

The first rocks deposited atop the Middle to Late Pennsylvanian unconformity are dark black shale of the Wolfcampian Stage. Unfortunately, this shale interval is not within the unitized interval and is therefore understudied within the field. The unitized interval at Fullerton includes deposits from the Abo and Wichita Formations (Wichita Group); lower and upper portion of the Clear Fork Group as well as the Tubb formation which lies between the two; and the Glorieta Formation which is the stratigraphically shallowest and

youngest formation. The gross unitized reservoir interval is an average of 2000ft thick. The Abo Formation represents the system tract of the oldest Leonardian sequence (L1) in the Permian Basin and is at the base of the unitized interval (Ruppel and Jones, 2006). The Abo facies consist primarily of fusulinid-crinoid packstone and wackestone alternating with peloidal packstone (XTO Energy, 2012). The Abo rocks are dolomitized and show high porosity; but due to an oil/water contact within the formation, they have not been explored, so little information on lithology exists. The thickness of the Abo Formation is not known due to poor well control but is estimated to be a minimum of 300ft thick.

The Wichita Formation is also dolomitized but consists of interbedded lime mudstone and local grainstone as well as thinly-bedded shallow water shale (Bane et al., 1994). Facies are a diversified aggregation of supratidal/tidal-flat as well as intertidal deposits. Total thickness of the Wichita Formation ranges from 110ft to 300ft within the study area (Ruppel and Jones, 2006).

First described by Dumble and Cummins (1890) from exposures of limestone, calcareous clay, and sandstone near the Clear Fork of the Brazos River in Shackelford and Jones counties of Texas, the Clear Fork Group was later extended elsewhere within the basin. From the eastern shelf region of Shackelford and Jones counties, the group was correlated with unnamed limestone deposits in the subsurface of the Midland Basin (Dunbar et al., 1960; Mosley, 1990). The upper Clear Fork, the interval of interest in this study, remains an informal component within the Clear Fork Group. Recent studies have subdivided the group into lower, middle, and upper units and the terms “upper Clear Fork formation” and “upper part of the Clear Fork formation” have been recognized by Silver and Todd (1969), Mazzullo (1982, 1995), Bane et al. (1994), Atchley et al. (1999), Ruppel (1992, 2002), Ruppel and Jones (2006), as well as Harrington and Lucia (2011).

The lower part of the Clear Fork formation within the study area is composed of subtidal, skeletal wackestone and packstone, alternating with peritidal (intertidal) and tidal-flat deposits. The alternating deposits document sea level rise and fall at both the cycle and high-frequency scales. Above the lower Clear Fork, the Tubb formation separates the lower and upper parts of the Clear Fork Group. The Tubb formation is comprised of fine-grained siliciclastics and believed to represent eolian sourced deposits (Ruppel et al., 2000). Ruppel et al. (2000) and Ruppel (2002) interpret the Tubb formation to be the base of a major Leonardian sequence (L3). The Tubb formation encompasses the top of the L2 or the base of the L3 and represents the maximum flooding surface terminating the end of a low-order transgression, and beginning the onset of a low-order highstand (Atchley et al., 1999). Figure 5 illustrates identified sequence sets within the Leonardian aged rocks from core in the neighboring North Robertson Field. However, not all sequences can be traced from North Robertson to the study area because of the Fullerton Field's higher structural position during deposition. It is important to note that sequences identified in work by Atchley et al. (1999) are not the major Leonardian sequences documented in outcrop studies by Ruppel et al. (2000). The Tubb formation acts as a seal to the lower Clear Fork and Wichita reservoirs. Later oxidation from exposure produced iron cement as shown on mudlogs, and is believed to give the eolian sourced sand its sealing properties.

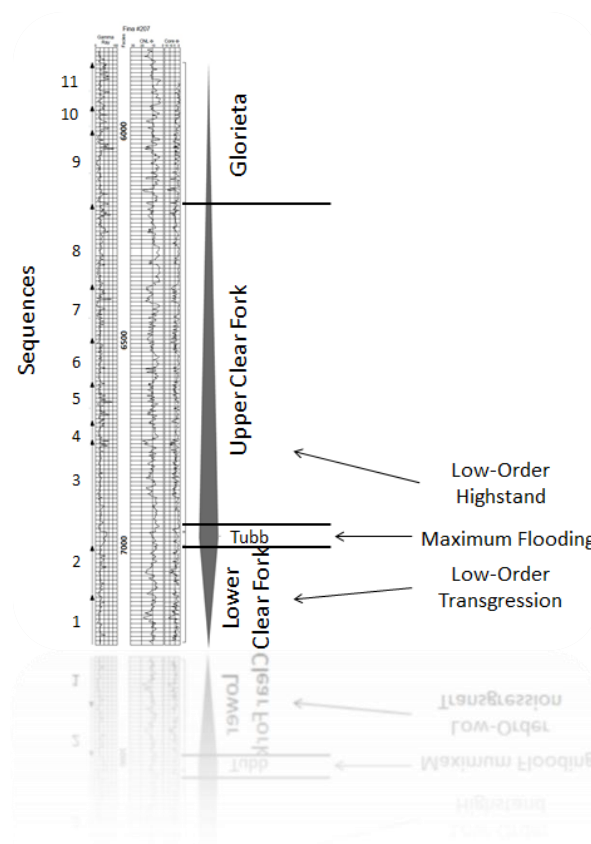


Figure 5: Illustration of Leonardian sequences in neighboring North Robertson Field.

Modified from Atchley et al. (1999).

In contrast to the lower Clear Fork formation, the base of the upper Clear Fork formation contains more continuous and permeable beds. The bottom of the upper Clear Fork is dominated by partially dolomitized packstone/grainstone shoals and subtidal packstone, in shoal-capped parasequences (No Author, 1998). Stratigraphically up section, towards the top of the formation, tidal-flat and sabkha deposits repeat in a parasequencing fashion, likely the result of sea level fluctuations. The dominance of algal mats and evaporite beds toward the top of the formation indicate a shallowing upward sequence. The shallowing upward sequence marks a transition from a platform-lagoonal

type environment to an algal flat environment and finally into an arid sabkha, supratidal environment, likely the result of an ensuing major regression.

The Glorieta Formation marks the youngest and shallowest strata of the Fullerton unitized interval. The Glorieta Formation is mainly siliciclastic but also contains nodular and bedded anhydrite, as well as dolomite. Red/brown staining of siltstone from the Glorieta is shown in Figure 21. The iron cement in the formation is believed, similar to the Tubb formation, to act as a seal to migrating hydrocarbons, at least in the local area of the study. Correlation of the Glorieta Formation using well logs in the field indicates the formation progrades towards the basin.

Depositional Environment

Similar to the northwestern shelf, the environmental setting of the Central Basin Platform during late Leonardian (upper Clear Fork) time was characterized by expansive, shallow water lagoons. However, these lagoons formed within carbonate bank complexes on the platform boundary and therefore isolated much of the interior CBP from terrestrial sediment input. The carbonate bank complexes at the shelf margin stood approximately 2,000 feet above the adjoining Midland Basin floor to the west (Hanford, 1981). Shelf margins from upper Clear Fork rocks are on average 3-5 miles wide but reach 10 miles on the northwestern shelf in Lubbock County, Texas (Silver and Todd, 1969).

The upper Clear Fork interior shelf inherited low relief depositional topography (Silver and Todd, 1969) whereas the shelf margins show a trend of aggradational deposition. Environmental settings ranged from arid supratidal, to restricted marine and rarely open marine (Figure 6). Lack of water input on the shelves, coupled with arid climates produced tidal-flat environments parallel with the shoreline during much of the late Leonardian. As with the northwestern shelf, these environments migrated both landward, towards the Central Basin Platform interior producing ankle-deep hypersaline

ponds and low relief mud flat coastal plains (Presley and McGillis, 1982) and seaward, toward the shelf edge depending on the rate of sedimentation. Modern analogues of these depositional environments include Qatar and the Trucial Coast of the Persian Gulf.

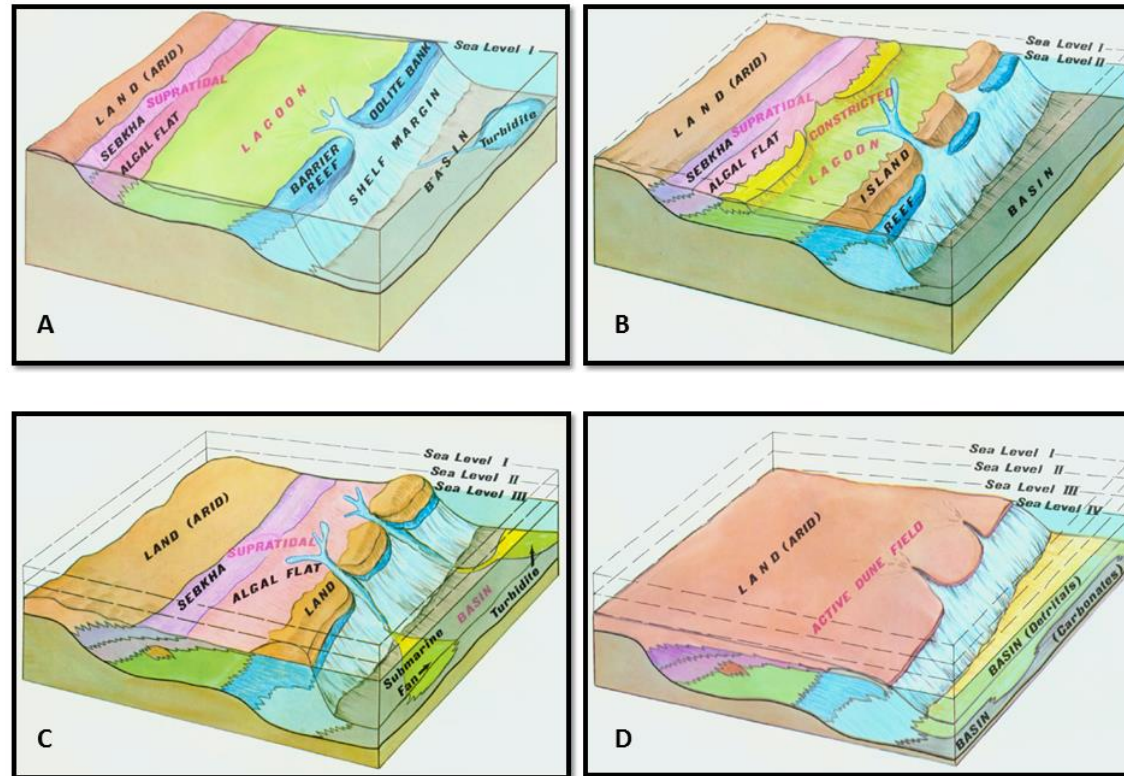


Figure 6: Illustration of changing Fullerton Field environments and their resultant stratigraphic stacking patterns during upper Clear Fork deposition. Modified from Silver and Todd (1969).

Study Location

The Fullerton Field encompasses around 29,000 acres and is considered one of the giant carbonate reservoirs in the Permian Basin. The location of the field is about 20 miles northwest of Andrews, Texas in Andrews County, near the border of Gaines County. The location of the core used in this study is on the northern flank of the eastern nose of the north dome anticline. The location is highlighted by a blue star in Figure 7.

A wireline log cross section, shown in Figure 8, shows the cored interval, along with 3 other wells. The 3 other wells wrap around the nose of the anticline and follow strike as closely as possible. Wells were chosen based on the available log suite and structural position. The cross section ties the differentiated sub-intervals to nearby wells for the use of reservoir exploitation. The identified core sub-intervals follow a nomenclature beginning with “*UCF*”, which stands for the upper Clear Fork, followed by a letter that corresponds to its relative position with “*A*” being the top (youngest) and “*E*” being the bottom (oldest). The zones are therefore labeled *UCF_A*; *UCF_B*; *UCF_C*; *UCF_D*; and *UCF_E*. A structural and stratigraphic cross section of the wells illustrating the representative sub-intervals can be seen in Figures 8 and 9.

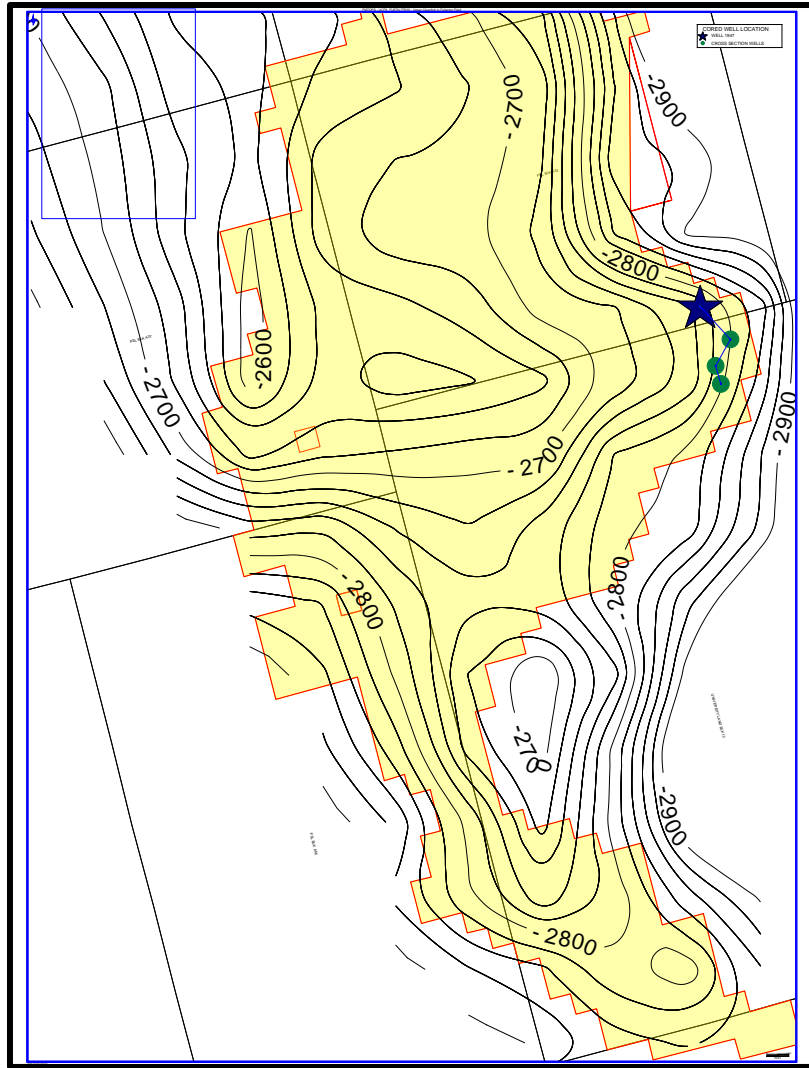


Figure 7: Structural map of the upper Clear Fork and well location. Structural depths are in feet below sea level. Star shows the position of well FCU 1947 and circles represent the wells shown in the cross section. Yellow is the unitized field area (XTO Energy, 2013).

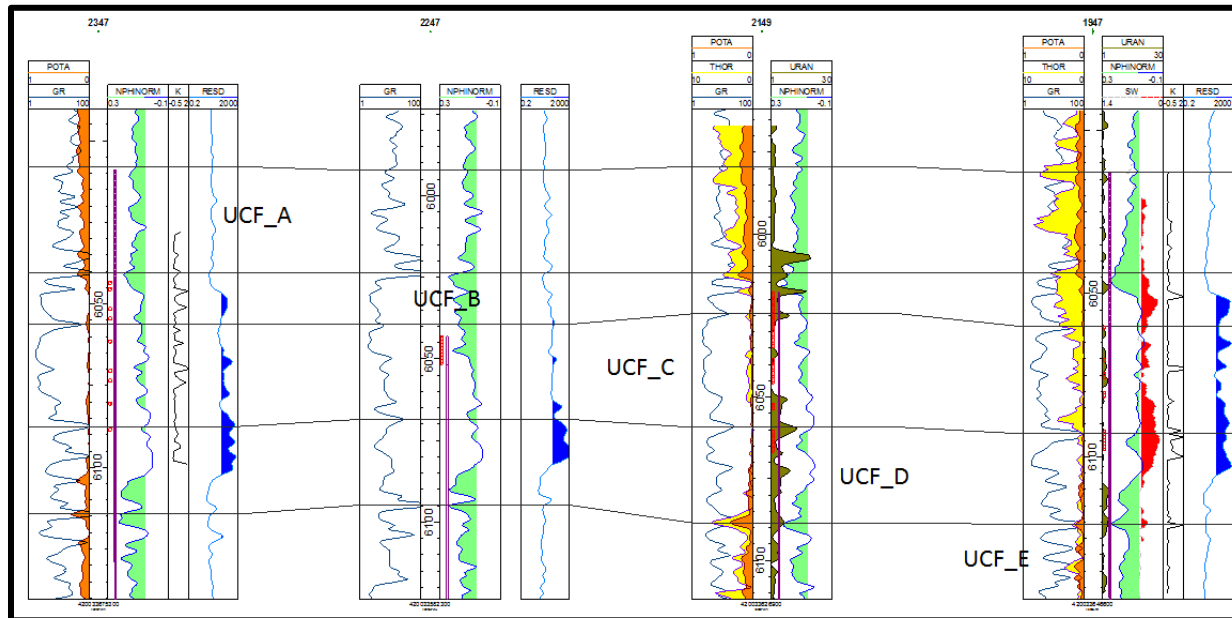


Figure 8: Stratigraphic cross section of FCU 1947 and nearby wells. Cross section is hung on the top of the upper Clear Fork, which is the base of sub-interval A in this study (XTO Energy, 2013).

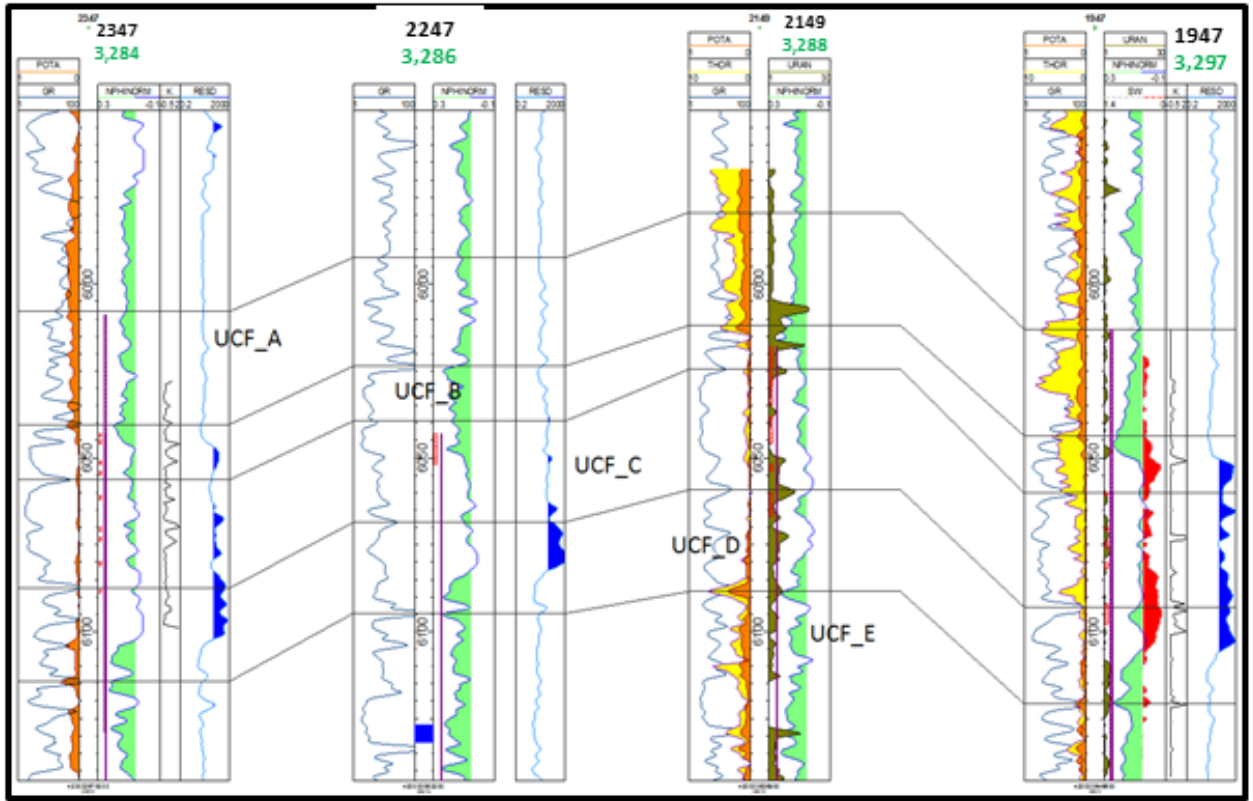


Figure 9: Structural cross section of FCU 1947 and nearby wells. Black number above well corresponds to well number, green corresponds to KB elevation (XTO Energy, 2013).

Chapter 3

Analysis of Fullerton 1947 Core

Core Interpretation

Macroscopic examination of the 1947 core shows an overall shallowing-upwards succession. This shallowing sequence is probably the product of rapid carbonate deposition filling the accommodation space due to the Central Basin Platform subsidence. The majority of the core is dominated by recrystallized mud and lacks grain supported textures. Reaction to 10% HCL acid was none to mild for the entire core, and dolomite was the primary mineral phase, followed by anhydrite.

Fossil assemblages were scarce and only skeletal debris was visible. However, microscopic investigation did find intact fossil specimens of foraminifers and conodont elements (Figure 34). Near surface dolomitization, evaporite precipitation, compaction and pressure dissolution all destroyed many depositional textures. The fine-grained, muddy nature of the core made microscopic lithofacies delineation difficult at best. Color and the textures used in the Dunham's (1962) classification were recognizable in the core and were used to distinguish the different lithofacies. Mudstone, wackestone, and packstone constitute the bulk of the core, suggesting dominantly restricted environments protected from wave action by basinward reefs prograding into the Midland Basin during middle Leonardian time. Rare grainstone facies suggest a few short lived switches to shallow, open-marine deposition.

Identifiable lithofacies in the core show parasequences and thin sections were taken from a majority of repeating facies. Parasequences are the smallest elemental building blocks of larger system tracts such as lowstands, transgressive tracts, and highstands. The individual parasequences can be distinguished by their vertical stacking patterns, and their bounding surfaces (Flügel, 2010). The parasequences documented

within the 1947 core are probably due to environmental changes occurring between fourth (10^3 years) and fifth (10^4 years) order cycles, suggested by their thicknesses (Flügel, 2010). The sea level fluctuations are inferred to be the tail end of a low-order highstand, as postulated by Atchley et al. (1999). Although sea level fluctuations are probably the most important control on parasequences within the core, Wright (1984) documents other important controls on cyclic development in intertidal and muddy tidal-flat environments such as tides and waves, hydrology and climate, sediment supply, and topography.

Mention of sea level changes below are not intended to delineate major sequences within the cored interval with the exception of the onset of the Leonardian 6 sequence at the top of the upper Clear Fork interval. Rather, their mention implies changing depositional realms through time in response to gradual sea level fluctuations within the study area.

The use of only one core in this study limits the ability to assemble a sequence stratigraphic framework in either 2 or 3 dimensions. However, the cored interval was divided into 5 sub-intervals (plate 1) which each probably represent fifth order cycles (10^4 years). The segregation of the core was done so that correlations to adjacent wells could be made via wireline logs. These sub-intervals are bounded by shallow water mudstone intervals interpreted as shifts in depositional environments from fluctuating sea levels. As mentioned previously, these sub-intervals are labeled as UCF (upper Clear Fork) followed by a letter from A to E that corresponds to stratigraphic position, with the former being the youngest and the latter being the oldest. The sub-intervals are described from oldest to youngest to represent depositional history in appropriate sequence. Their slabbed depth intervals are: 6145'-6123', 6122'-6095', 6094'-6062', 6061'-6046', and 6045'-6015' respectively.

All units of depth are in feet (') and depth (MD) is measured from the Kelly Bushing (KB). All slabbed core is 3¼" wide in photographs. In plate 1, distinguishable lithofacies are assigned a letter from A to N (which do not correspond to sub-interval letters) as well as a color. Assignment of letters and colors to unique lithofacies was done to illustrate individual bed parasequences and vertical stacking patterns of the core. Lithofacies were examined microscopically in thin sections using a petrographic microscope (see Chapter 4).

Results

Sub-Interval UCF_E (6145'-6123')

At the bottom of the cored interval, from 6142'-6121', beds are extremely cyclic, and range from 1-2 feet thick. Beds cycle between lime mudstone and packstone; the mudstone lithology displays relatively high organic content and gray to dark gray colors. Skeletal-peloidal wackestone and packstone in the lower (deeper) section show moderate to highly bioturbated sediment including several beds with poorly preserved fossil fragments. Rudstone with mud intraclasts is present at 6141', 6131', and 6129' (Figure 10). The rudstone lithofacies are overlain by a gray, finely laminated siltstone/mudstone. At 6130', small burrows or root structures, filled with anhydrite, are found in a light beige mudstone (Figure 11). Algal laminations at 6128' (Figure 12) grade up section into a light beige, slightly mottled mudstone. There are three repeating sequences of these facies (lithoclasts, mudstone, laminations) within the sub-interval which terminates at 6123'.

Sub-Interval UCF_D (6124'-6095')

The base of sub-interval D is bounded by a dark gray, organic rich shale at 6123' which grades into a tan mudstone. From depths 6120' to 6107', lithofacies are nearly identical to sub-interval E, with cycling packstone and mudstone. The upper portion of

sub-interval D, from 6106' to 6095', displays facies analogous to those in the sub-interval C, above it. Bedding thicknesses are similar to facies in sub-interval E but thicken up section. At 6119', 6114', and 6107', small mud intraclasts and fossil fragments are deposited. Facies gradually become more muddy, and anhydrite rich up section. From 6106' to 6095', most of the depositional textures have been completely destroyed, and large anhydrite nodules are precipitated. A stylolitic mudstone/wackestone is deposited at 6095' and marks the top of sub-interval D.

Sub-Interval UCF_C (6094'-6062')

From the base of sub-interval C at 6094', to 6091', a skeletal packstone/grainstone (rudstone) facies is deposited. Orientation of skeletal grains in the deposits is random and poorly sorted. Above the packstone/grainstone facies, starting at 6089', lithofacies gradationally become more muddy and less grain-rich. The muddy facies up section grade from their base as very mottled and burrowed to more massive, homogenous and less burrowed mudstone with anhydrite of both nodular and pore filling types. Facies also grade to more crystalline and loose almost all depositional texture up section.

Furthermore, nodules of anhydrite progressively become greater in size up section with nodules at 6067' showing sizes greater than 3 inches. Mud dominated rocks continue up to 6066', where they become skeletal grain dominated once more within the sub-interval. Skeletal fragments, very similar to the grainstone facies at 6091'-6094', include crinoid, ostracode and bivalve angular grains. At the base of 6063', rocks abruptly become finely laminated gray mudstone and grade into a slightly silty mudstone with wispy laminations. The mudstone interval at 6062' marks the top of sub-interval C.

Sub-Interval UCF_B (6061'-6046')

An organic rich mudstone bounds the bottom of sub-interval B at a depth of 6061' MD. Directly atop, large nodular and anhydrite crystals are deposited from 6060' to 6057' in recrystallized mudstone beds. From 6056'-6054', mudstone beds are inclined between 5° and 8°. From 6053' to 6051', dominant lithofacies are recrystallized mudstone with unrecognizable depositional textures. At 6050', facies abruptly terminate from dark gray mudstone into light beige recrystallized supratidal wackestone/packstone (Figure 16). The wackestone facies grade up section from no laminations to wispy laminations, and display small mudcracks. At 6046', a dark gray mudstone/siltstone is deposited which is also the final deposit of sub-interval B.

Sub-Interval UCF_A (6045'-6015')

At the base of sub-interval A, from 6046' to 6044.5', a siltstone is deposited. Directly atop it, beige wackestone with discontinuous, wispy laminations are layered from 6044.5' to 6043'. Light beige heavily bioturbated packstone with medium sized nodules of anhydrite, and few laminations are deposited directly above it to the top of 6042'. From 6041' to 6039', a highly organic rich, siltstone/mudstone, displaying no bioturbation and pyrite nodules (Figure 17) is deposited. The organic rich interval is terminated at the top by diapiric (enterolithic) anhydrite (Figure 18). The diapiric anhydrite continues up through 6038' where light beige wackestone with small discontinuous laminations truncate the anhydrite. Laminations cycle to more parallel at 6037' and represent varves. Varves grade into wispy but slightly continuous laminations at 6036', and finally terminate at 6035' where facies become algal. Algal facies considered to be a type of bindstone are interbedded with dolomite and anhydrite deposits from 6035' to the base of 6032'.

Finely laminated shale with vertical fractures is deposited from 6032' to 6030'. Massive light beige mudstone is deposited above the shale until 6028.5' where mudstone

becomes bioturbated and mottled. A switch to continuous, non-parallel laminations in a dark beige mudstone, begin at 6027' and continue through 6026', where a sharp contact from mudstone to bedded anhydrite is seen. The bedded anhydrite is a foot thick and displays a "chicken wire" texture at the top. From 6025' to 6023', beige mudstone/wackestone facies grade from thin wispy laminations to thicker, less frequent organic laminations. Prominent mudcracks are documented in 6023' (Figure 19). Truncated laminations and mudcracks continue to 6021' where they become algal bindstone once more (Figure 20). The algal mats are interbedded with large anhydrite nodules and dolomite layers similar to lithofacies at 6035'. Algal facies grade into thin fenestral laminations from 6021' to 6019' where they are again abruptly terminated by massive anhydrite. The massive anhydrite is slightly thicker than its 6026' counterpart, constituting 2 feet of total thickness. Above the massive anhydrite, there is a sharp erosional contact at 6018'. A red/brown silty dolomite is deposited from 6018' to 6016' (Figure 21) where it becomes interbedded with nodular anhydrite. The nodular anhydrite marks the top of the core at 6015' (Figure 23).

Discussion

Sub-Interval UCF_E (6145'-6123')

Relative to other sub-intervals, the E sub-interval displays thinner beds, and repeating laminations. There is also less anhydrite in comparison to the other sub-interval facies which could be an indication of higher energy and/or less lagoonal restriction. Cyclic packstone and mudstone, and the presence of carbonate intraclasts (Figure 10) in the basal portions of the rudstone, was probably the product of a rapid transgression. A greater amount of bioturbation is also documented in the sub-interval. As postulated by Scholle et al. (1983), features such as gray colors interbedded with tan colors, grainier fabric, fossil fragments, burrow/root structures (Figure 11), thin laminations switching

between nonparallel and parallel, algal laminations (Figure 12), and the limited amount of anhydrite all suggest that this sub-interval was deposited in a restricted to open-marine lagoonal environment, behind reefs, but within normal tide range. The intertidal facies are terminated at the top by a highly organic mudstone as a result of an ensuing transgression.

Sub-Interval UCF_D (6124'-6095')

The relatively more massive beds in the upper portion of the sub-interval are characterized as recrystallized mudstone that has been subjected to immense dolomitization creating an almost entirely crystalline texture. Prior to dolomitization, this mudstone was likely pelleted. The lack of sedimentary structures can also be attributed to the homogenizing of sediment via burrowing, before compaction, as documented in work from Scholle et al. (1983). Fossil fragments deposited in facies further suggest the process of homogenizing.

The presence of anhydrite in the upper beds is probably the result of lagoonal restriction and consequent seawater evaporation. The nodular anhydrite (Figure 13) is not a depositional feature but rather a diagenetic feature formed from the precipitation of anhydrite within the interstitial water of the sediment (Lucia, 1972).

The base of the D sub-interval is interpreted to be a repeating parasequence of sub-interval E. Therefore, its depositional environment is dominantly intertidal. The upper portion of sub-interval D is believed to be a presequence of sub-interval C, bounded at the top by a highly stylolitic mudstone. Therefore, its depositional environment is subtidal. The abundance of stylolites indicates compaction of sediment and the concentration of insoluble matter. The change in facies, as well as bedding thickness, from the base to the top further exemplifies a rising sea level (transgression).

Sub-Interval UCF_C (6094'-6062')

The recrystallized mudstone/wackestone facies (Figure 14) at the base of this sub-interval and the formation of stylolites within the facies indicates deep burial. Deep burial introduced a mechanical component of diagenesis and consequent chemical component of pressure dissolution. The combination of these two components caused depositional facies to be obliterated. Ranging from less than a millimeter to several millimeters in thickness, the stylolites consist of concentrated insoluble organic matter and clays. Their presence is believed to be a product of compaction and burial diagenesis of great volumes of mud. Orientation of debris in skeletal packstone/grainstone facies (Figure 15) deposited at 6094'-6091' suggests deposition in a chaotic fashion, resultant of a switch from a low-energy restricted subtidal environment to a short lived open marine environment.

The C sub-interval of the upper Clear Fork core is determined to have been deposited in a largely subtidal environment, most likely of open marine to restricted lagoonal position. Relatively more massive mud-dominated bedding and lack of laminations indicate little exposure and quiet, low energy settings, where thick sequences of pelleted carbonate mud could accumulate. Anhydrite emplacement in the facies is likely the result of lagoonal restriction, similar to facies in sub-interval D. The brine rich interstitial water is probably the result of seawater evaporation in these restricted lagoons. However, another less accepted theory states that hypersaline brines originated from up-dip tidal-flat environments, as mentioned in work by Shields and Brady (1995). The thick sequence of mud-rich deposits between grain-rich skeletal packstone/grainstone deposits is believed to be the result of a sea level highstand.

Sub-Interval UCF_B (6061'-6046')

The sub-Interval B was determined to be an overall transition from shallow subtidal, to intertidal, and finally supratidal deposition. Organic rich mudstone at the base of the sub-interval with anhydrite rich deposits grading up section, are interpreted to be a product of regression of a sea level highstand. Inclined bedding from 6053' to 6051' is assumed to dip towards the basin, resultant of a falling sea level. The gradation from no laminations, to wispy laminations, beginning at 6050', along with abundant small mudcracks, conclude a switch to supratidal deposition as documented in work by Lucia (1972). The silt rich interval deposited above the supratidal facies is interpreted to be a result of rapid sea level fall.

Sub-Interval UCF_A (6045'-6015')

The stratigraphically highest sub-interval in the section was determined to contain dominantly supratidal and very shallow intertidal facies. The base of sub-interval A is the top of the upper part of the Clear Fork formation and above it strata of the basal part of the Glorieta Formation is deposited. The termination of the upper Clear Fork deposition is believed to be documented by final tidal-flat sequencing. The repeating supratidal facies concludes this shallowing-upwards succession. Parallel laminations seen in mudstone are believed to represent varves deposited in sitting bodies of shallow water. Bodies of water were likely restricted lagoons or tidal pools within the supratidal realm or the far reaches of an intertidal realm. Nonparallel laminations were determined to be current induced. Mudcracks indicate long periods of arid exposure where desiccation of sediment took place. Algal laminations and fenestrae without anhydrite nodules were likely deposited in intertidal environments as algal mats. Algal laminations with interbedded anhydrite nodules were probably deposited in a highly saline restricted lagoonal environment where only algae could thrive.

Bedded and “chicken-wire” anhydrite is found at two intervals within sub-interval A and are the only two beds found in the cored interval. Dissimilar to nodular, and replacement forms, bedded anhydrite is a depositional feature rather than a diagenetic feature (Lucia, 1972). The thick beds were formed when large volumes of sea water were evaporated from restricted lagoons. Pyrite nodules (Figure 17) in silty intervals at the bottom of the sub-interval suggest anoxic conditions, whereas red/brown staining (Figure 21) in dolomitic mudstone at the top indicates an oxidizing environment. Overall the colors of the beds in this sub-interval grade from slightly reduced gray to oxidized red/brown further suggesting a switch from an intertidal to supratidal environment. In conclusion, mudcracks, bedded anhydrite, fenestrae, as well as storm, algal, truncated, and wispy laminations are all diagnostic of supratidal environments, as postulated by Scholle et al. (1983) and Lucia (1972). This transition is believed to correlate with the base of the major Leonardian sequence 6 identified from outcrops in the Sierra Diablo Mountains in work by Ruppel et al. (2000).



Figure 10: Core photograph of rudstone from depth 6129'. Notice the mud intraclasts probably transported from nearby environments.



Figure 11: Core photograph of burrow or root structures at depth 6129' MD.



Figure 12: Core photograph of non-parallel algal mats at depth 6128'.



Figure 13: Core photograph of a large anhydrite nodule, a diagenetic feature, and heavily altered depositional facies (depth of 6106').



Figure 14: Core photograph of recrystallized mudstone/wackestone facies from the bottom of sub-interval C displaying well developed stylolites.

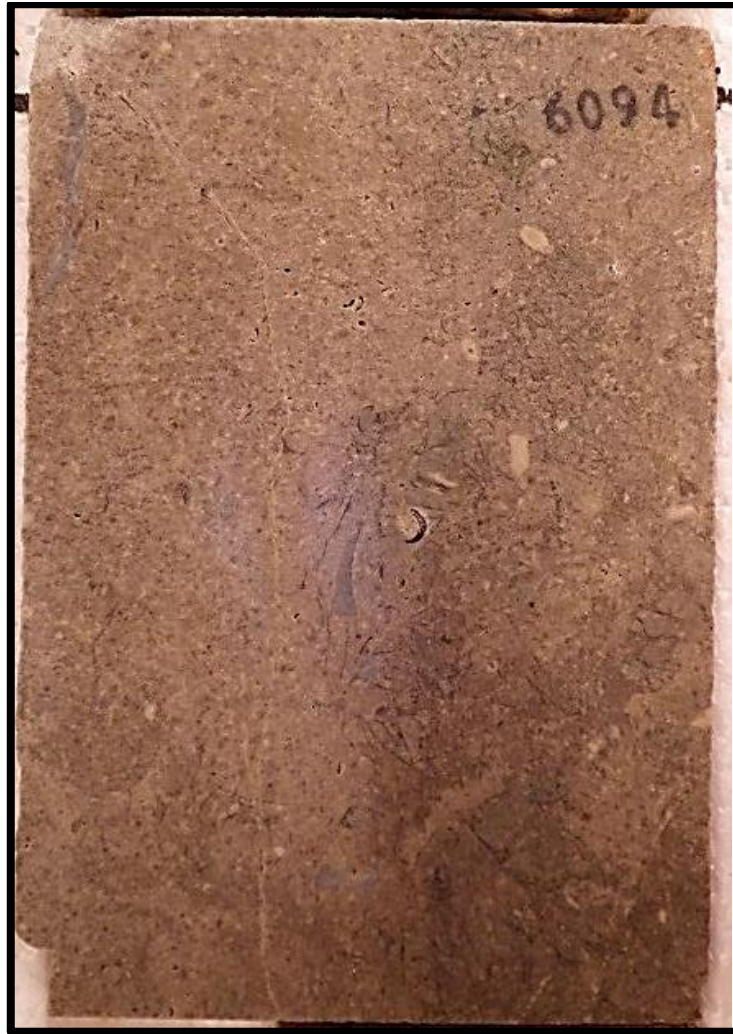


Figure 15: Skeletal packstone/grainstone facies suggesting a high-energy beach face environment.



Figure 16: Core photograph (6050') documenting abrupt change from organic rich mudstone (bottom) to supratidal, grain (fine) rich wackestone.



Figure 17: Core photograph of pyrite nodule in organic rich shaley mudstone. Pyrite nodule is an indication of anoxic conditions, like a result of lagoonal starvation where algal mats could grow but carbonate production is limited.



Figure 18: Core photograph of diapiric anhydrite (6038').



Figure 19: Core photograph of prominent mudcracks indicating desiccation (6023').



Figure 20: Core photograph of algal mat with interbedded dolomite and nodular anhydrite (6021').



Figure 21: Core photograph of red/brown silty dolomite with wispy laminations indicating oxidizing conditions (6016').



Figure 22: Core photograph of algal mat overlain by a thin organic rich siltstone and capped by bedded and chicken-wire anhydrite. Diagnostic features of transition from intertidal to supratidal depositional realm.



Figure 23: Core photograph of nodular anhydrite in a red/brown silty dolomite (6015').

Depositional Model

From the core interpretation, a depositional model was generated for the study area (Figure 24). All inferred depositional environments are in the shallow water, low-energy realm. The environments were protected from reefal developments toward the basin. The low-energy setting helped contribute large amounts of mud to the systems. Work from Atchley et al. (1999) suggests upper Clear Fork deposition in nearby Robertson Field, to have taken place in humid, wet climates which had abundant plant matter. Examination of the Fullerton 1947 core found no plant matter, but did document what appear to be small root traces. However, the presence of large volumes of evaporite indicates more arid climate such those in the Persian Gulf (Ahr, 2008). The lack of plant matter and abundance of evaporite within the core concludes that deposition took place in dominantly arid conditions.

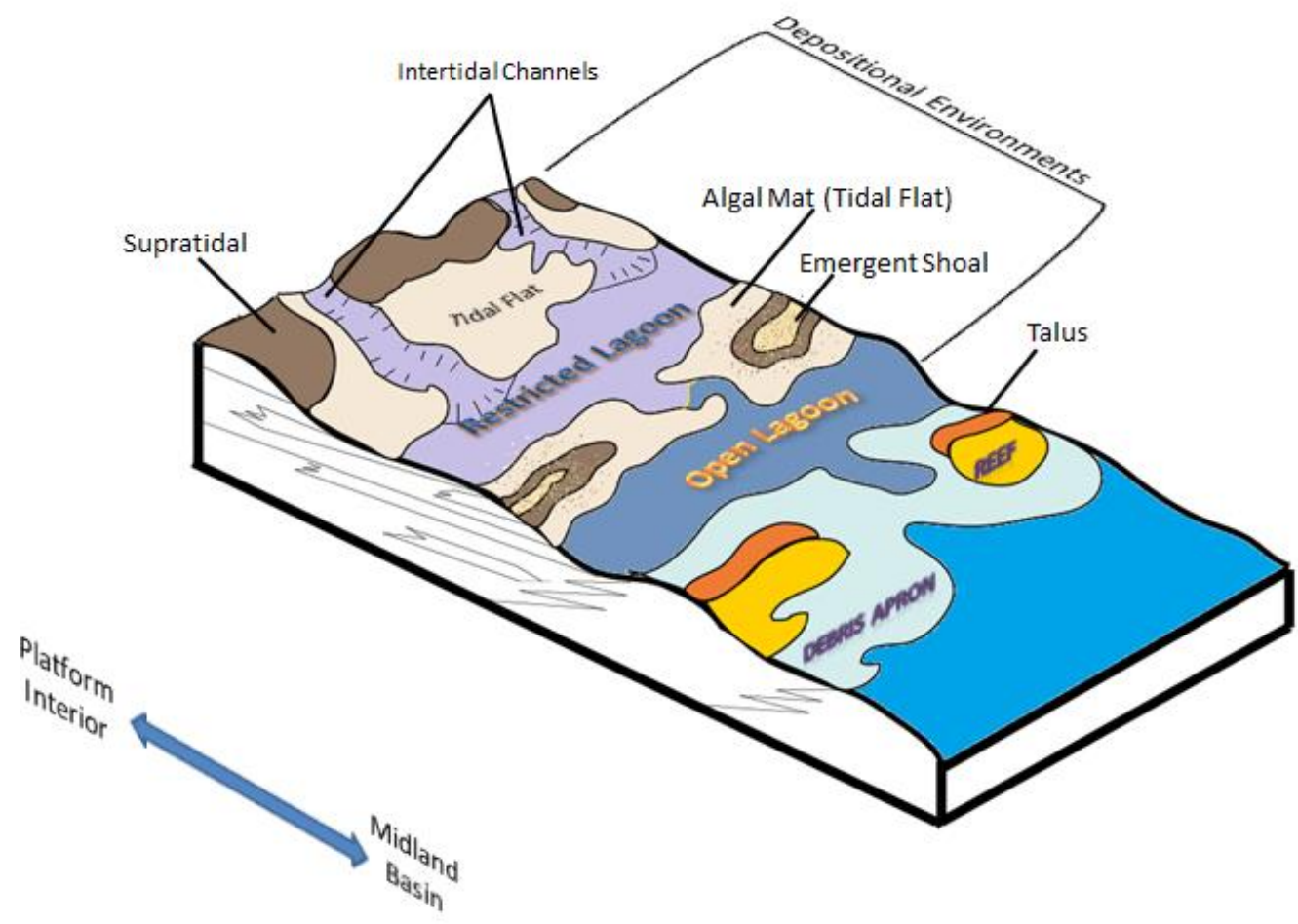


Figure 24: Depositional model of the Fullerton Field as determined from core analysis.

Core Laboratories Analysis of Reservoir Properties

The well in this study was cored using diamond coring equipment and brine to obtain 4 inch diameter cores from depths of 6015' to 6145' MD (6013'-6143' corrected depth-discussed in chapter 6) of the upper part of the Clear Fork formation. The core was preserved at the well site in a CO₂ atmosphere and transported to Midland, TX by Core Laboratories personnel. Fluid saturations were determined using the Dean Stark Technique. Gas expansion grain density and porosity were determined using Boyle's Law. Air permeability was measured whereas the core was held in a Hassler rubber sleeve.

Measurements of core attributes yielded widely changing values from foot to foot. Abruptly changing values is indicative of carbonate reservoirs and further concludes the complications of their characterization. To overcome the complex nature of these reservoirs, geometric averages of each representative sub-interval were computed. The averaging of these sub-intervals can aid in their exploitation. Moreover, averaging of sub-intervals was done because neither wireline logs nor completions practices have the resolution to target individual beds when highly cyclic systems are in place.

Porosity Analysis Results

Plate 1 includes measured porosity values for each individual foot measured by Core Laboratories. Porosity values between each foot vary widely. Values of porosity range from 1.1 to 16.4 percent. By averaging the values for each sub-interval, trends between dominant depositional environments were inferred. Figure 25 shows a bar chart of average porosity values for each sub-interval.

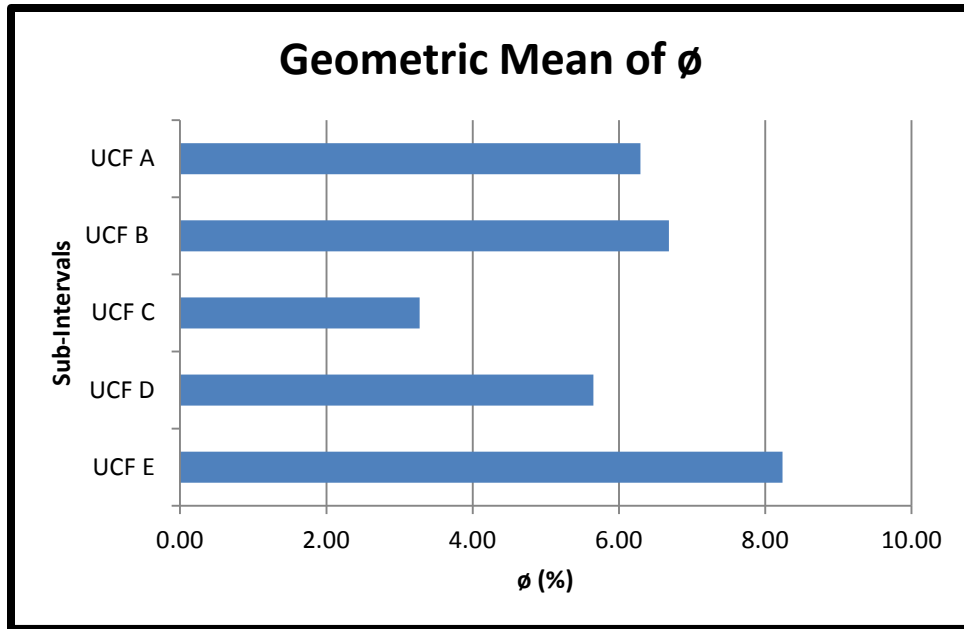


Figure 25: Bar chart of average porosity for each sub-interval.

Porosity Analysis Discussion

Sub-Interval UCF_E

From the chart it is apparent that sub-interval E has the highest average porosity, calculated to be 8.2 percent over an interval of 22 feet. From core examination it was determined that most facies in sub-interval E were deposited in an intertidal environment. The lowest and highest porosity values in the sub-interval are 4.2 and 12.7 percent, respectively. The higher average porosity is believed to be a reflection of two attributes. First, daily tidal exposure and cover protected sediment from excess evaporite deposition. Second, the intertidal deposits show a grain-rich fabric consisting of lithoclasts, micritized peloids, and skeletal fragments.

Sub-Interval UCF_D

Sub-interval D shows the second to lowest average porosity within the core, calculated at 5.7 percent over an interval of 28 feet. Determined from core examination, the bottom half of the sub-interval was deposited in the intertidal realm and the top half in the subtidal realm. Similar to sub-interval E, the intertidal facies show good porosity. Oppositely, the subtidal facies in the upper portion of the sub-interval show little porosity with values as low as 1.2 percent. The subtidal facies consist of mostly mudstone which was tightened and recrystallized by compaction diagenesis.

Sub-Interval UCF_C

The sub-interval C has the lowest average porosity with a value of 3.3 percent over an interval of 33 feet. As with the top of sub-interval D, the subtidal facies in sub-interval C have much less porosity. The subtidal facies, documented through almost all of sub-interval C, have significant amounts of anhydrite. The anhydrite within the facies includes nodular, poikilotopic and pore filling. These types of anhydrite are diagenetic rather than depositional. The anhydrite in the sub-interval is thought to have two sources. The main source is believed to be from interstitial hypersaline water deposited with the sediment at burial. The second source, believed to contribute to the pore filling type, is thought to have precipitated during early diagenesis from percolating sulfate rich waters from up-dip tidal-flat environments (Ahr, 2008). The precipitated anhydrite occluded most depositional and secondary porosity and is the major contributor to poor reservoir quality.

Sub-Interval UCF_B

Sub-interval B has the second highest average porosity within the core with a value of 6.7 percent over an interval of 16 feet. Subtidal, intertidal and supratidal facies are all deposited in sub-interval B. As with the subtidal facies of other sub-intervals, their recrystallized and anhydrite nature give them low porosity. The intertidal and supratidal

facies show the highest porosity values in the core. The high porosity values supratidal facies is believed to be caused from several factors. One factor is the angular but fine-grained nature of their skeletal deposits which leaves them with interparticle and intercrystal pore space. The skeletal deposits were likely transported to their depositional location during storm events. Secondly, the physiographic position of the supratidal environments exposed them to freshwater diagenesis. The freshwater aided in dissolution of soluble carbonate grains. This dissolution process is evident in thin sections from the top sub-interval B (Figures 40 and 41). The process aided in the development of secondary porosity.

Sub-Interval UCF_A

The third highest average porosity is found in sub-interval A, calculated at 6.3 percent over an interval of 31 feet. The dominant facies type was determined from core examination to be supratidal, although some intertidal facies do exist. As with sub-interval B, the grain-rich nature of the supratidal facies adds to the overall porosity of the sub-interval. However, the deposition of bedded anhydrite reduces the overall porosity.

Permeability Analysis Results

Similar to the porosity analysis, permeability measurements showed widely variable values from foot to foot. One measurement, from a measured depth of 6075 feet, was omitted from the data set. The measurement was thrown out because of its extremely large value of 3820 millidarcies. Such a large value was determined to be an erroneous measurement, likely the result of a broken or damaged sample. A bar chart of average permeability for each sub-interval is show in Figure 26.

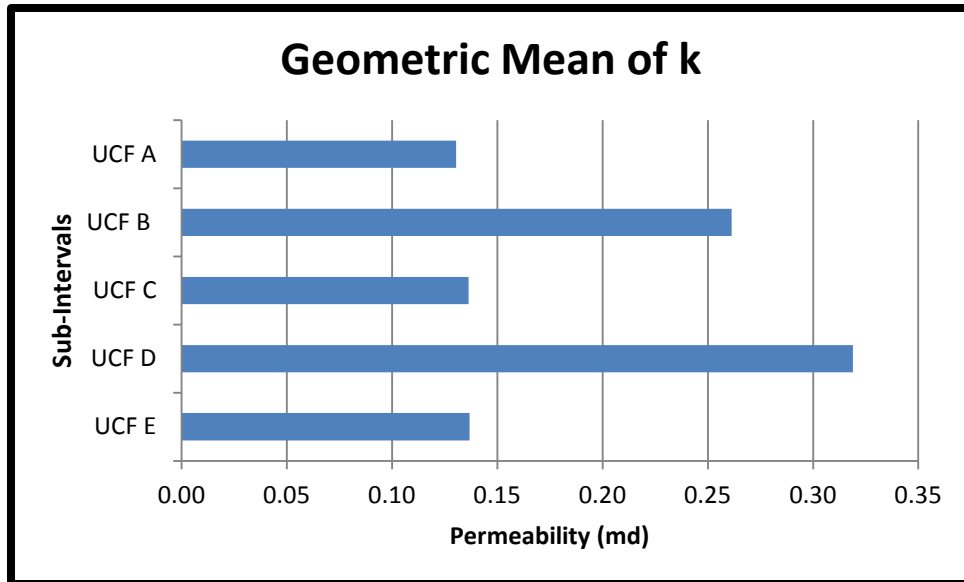


Figure 26: Bar chart of average permeability for each sub-interval.

Permeability Analysis Discussion

Opposite to porosity analysis, permeability analysis only shows a few correlations between depositional environments and measured values. The analysis by segregation of sub-intervals rendered no unique conclusions. For the purpose of this analysis, determined interpretations are listed below, rather than in individual sub-intervals. These interpretations were:

- 1.) Deposits below unconformities or shaley intervals show consistently higher permeability values. Higher permeability values are probably a product of rapid change in depositional environment and diagenetic realm.
- 2.) Supratidal facies show higher permeability values, likely due to freshwater diagenesis and consequent opening of pore throats.
- 3.) Facies with poikilotopic anhydrite identified in core and thin sections, display relatively higher permeability values.

Grain Density Analysis Results

Grain density analysis indicates a dominance of dolomite and anhydrite lithology in the core. A bar chart of average grain density values for each sub-interval is found in Figure 27.

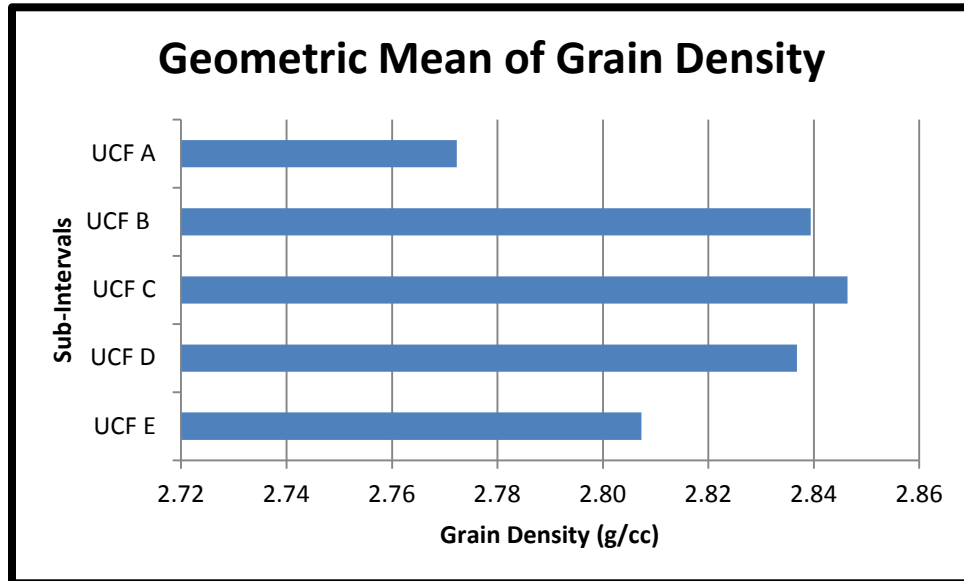


Figure 27: Bar chart of average grain density values for each sub-interval.

Grain Density Analysis Discussion

Unlike the permeability analysis, grain density measurements showed more consistent trends. Except for sub-interval A, all of the others showed an average grain density of between 2.80 and 2.85 g/cm³. Grain density values indicate a dominantly dolomite mineralogy, which has a known value of 2.87 g/cm³ (Asquith and Gibson, 1982). Values above 2.87 g/cm³ were determined to be an indication of greater amounts of precipitated anhydrite, which has a known grain density of 2.98 g/cm³ (Asquith and Gibson, 1982). Lower grain density values were attributed to added amounts of quartz.

Sandstone, for instance, has a known grain density of 2.65 g/cm^3 (Asquith and Gibson, 1982).

Sub-Interval UCF_E

The second lowest average grain density was found in sub-interval E, calculated to be 2.807 g/cm^3 . The lower value is believed to be a reflection of relatively less evaporite precipitation because facies were deposited in dominantly intertidal realms where standing sea water was rare.

Sub-Interval UCF_D

Sub-interval D has the third highest average grain density, at 2.837 g/cm^3 . The subtidal facies, and precipitated anhydrite, at the top of the sub-interval contribute significantly to the overall high grain density value.

Sub-Interval UCF_C

The greatest average grain density of 2.846 g/cm^3 is found in sub-interval C. Almost all facies in this sub-interval are determined to be subtidal. The subtidal facies were also determined to be deposited in restricted lagoons, or ponds. Therefore, they contain the largest amount of anhydrite which adds to the overall higher grain density.

Sub-Interval UCF_B

With a grain density value of 2.839 g/cm^3 , sub-interval B has the second greatest average grain density. The high grain density can be attributed to the subtidal facies that bound the bottom of the sub-interval.

Sub-Interval UCF_A

The lowest average grain density of 2.772 g/cm^3 was found in sub-interval A. The supratidal and silty (quartz) deposits of this sub-interval contribute to its overall lower grain density.

Chapter 4
Microscopic Examination
Thin Section Examination

Results

A total of 21 thin sections were fabricated for this study. Intervals were selected from core on the criteria that they were either (1) an apparent repeating lithofacies, (2) an apparent depositional facies (subtidal, intertidal, supratidal), (3) showed significant porosity (from core laboratory analysis), (4) had features that warranted petrographic examination, or some combination of the four.

Thin sections were initially categorized from whole-core examination using the Dunham's classification scheme (Dunham, 1962). However, some samples, when described petrographically, were later reclassified because their macroscopic and microscopic descriptions showed discrepancies. Extremely small grain sizes and heavy diagenetic overprint explain the differences between the two scales of observations. Descriptions of individual thin sections are found in Appendices A. Figure 28 summarizes all samples, their Dunham (1962) classification, interpreted depositional environment, and mineral percentages.

			<i>Mineral Composition</i>				
Sample	Classification	Interpreted Depositional Realm	Dolomite (%)	Anhydrite (%)	Calcite (%)	Quartz (%)	Organics (%)
A1-6042	Skeletal laminated Ws/Ps	Supratidal	35	15	30	15	5
B1-6046	Quartz rich Ws	Supratidal	25	15	30	25	5
B2-6048	fenestral laminated Ws	Supratidal/Very shallow Intertidal	35	15	35	10	5
C1-6052	Crystalline Anhydritic Dolomite (Ms/Ws)	Intertidal	65	30	0	0	5
C2-6053	Crystalline Anhydritic Dolomite (Ms/Ws)	Intertidal	50	45	0	0	5
C3-6054	Crystalline Anhydritic Dolomite (Ms/Ws)	Intertidal/Subtidal	45	50	0	0	5
E1-6069	Crystalline Anhydritic Dolomite (Ms)	Subtidal	55	35	0	0	10
E2-6073	Crystalline Anhydritic Dolomite (Ws)	Subtidal	45	45	5	0	5
G1-6084	Crystalline Anhydritic Dolomite (Ms)	Subtidal	65	30	0	0	5
G2-6090	Crystalline Anhydritic Dolomite (Ms)	Subtidal	57	40	0	0	3
G3-6099	Crystalline Anhydritic Dolomite (Ms)	Subtidal	55	35	0	0	10
I1-6116	Algal Laminated Ms/Ws	Intertidal	25	30	40	0	5
I2-6120	Intraclastic Ws	Intertidal	45	5	40	0	10
I3-6143	Mottled Skeletal Ws	Intertidal	45	5	35	10	5
K1-6117	Mottled Mudstone	Intertidal/Subtidal	45	5	40	7	3
K2-6126	Skeletal Ms/Ws	Intertidal/Subtidal	50	5	40	0	5
L1-6125	Laminated Mottled Mudstone	Intertidal	50	10	25	5	10
L2-6127	Mottled Ms/Ws	Intertidal	30	15	50	0	5
L3-6134	Laminated Ms/Ws	Intertidal	35	15	45	0	5
M1-6128	Algal Laminated Intraclast Packstone	Intertidal	20	25	50	0	5
M2-6137	Mottled Wackestone	Intertidal	30	15	30	20	5

Figure 28: Thin section analysis results. Ms = Mudstone, Ws = Wackestone, Ps = Packstone.

Discussion

An important observation found during petrographic examination was the presence of mud, or recrystallized mud, in every sample. The dominance of mud suggests low energy depositional settings, protected from normal wave action. Classified lithofacies range from remnant mudstone to remnant packstone, but also include crystalline facies in which diagenesis and recrystallization has completely obliterated depositional texture. Another observation was the presence of anhydrite, to some degree, in every sample. The placement of anhydrite both diagenetically and depositionally, as well as their four identified types, is described in this chapter. Because all samples were deposited in dominantly low energy environments their unique segregation based solely on Dunham's classification (Dunham, 1962), was problematic. For this reason, thin sections were divided on the basis of their depositional realms. The three depositional realms of the samples were divided as: supratidal, intertidal, and shallow subtidal. It is important to note that the term low energy refers to the restricted interior environments of these depositional realms, even though occasional spring tides or storms did bring higher energy deposits.

Supratidal Microfacies

Supratidal microfacies display high abundance of fine-grained skeletal constituents. Skeletal grains were determined to be thin shelled ostracodes, bivalves and foraminifers. In these facies, grains were angular and are probably storm or spring deposits that were transported from marginal reefs and lagoons to the tidal-flat suggested by Lucia (1969). Very fine-grained-quartz in the facies is also an indicator of supratidal realms. Samples A1-6042, B1-6046, and B2-6048 were determined to be supratidal and contain greater than 10 percent fine-grained quartz. The quartz probably originated from

windblown terrestrial deposits as irregular, very fine laminations of silt beds. Lithoclasts of desiccated mudflakes are also found in supratidal microfacies.

Similar to intertidal and opposite to subtidal facies, supratidal facies document moderate preservation of depositional features. Mudcracks are displayed in sample A1-6042 (Figure 29). Although depositional features are preserved, the dominant mineral phase in supratidal facies is still secondary dolomite which somewhat alters depositional textures. This finding further suggests syngenetic replacement of original limestone, by refluxing hypersaline brines. However, minor amounts of calcite are still present to some degree in all supratidal samples.



Figure 29: Photomicrograph of supratidal facies displaying fine skeletal grains and mudcracks. Sample A1-6042 - 12.5x CPL. Arrow indicates stratigraphically up.

Intertidal Microfacies

Intertidal microfacies have many similar features as supratidal facies. Similarities between the two facies include angular skeletal grains and fine-grained quartz. Skeletal grains in the intertidal facies consist of similar organisms as supratidal facies but are

slightly more intact and larger. However, intertidal facies display more mottled structures (Figure 30) and algal laminations (Figure 31). They also feature distinct burrows which are less common in supratidal facies. Another unique feature of intertidal facies is the presence of micritized peloid intraclasts (Figure 32). Samples C1-6052, C2-6053, C3-6054, I1-6116, I2-6120, I3-6143, K1-6117, K2-6126, L1-6125, L2-6127, L3-6134, M1-6128 and M2-6137 were determined to be intertidal microfacies. However, samples C3-6054, K1-6117 and K2-6126 are believed to be marginal subtidal/intertidal environments.

As with supratidal facies, intertidal facies do show some preservation of depositional features. Relative to the supratidal facies, intertidal facies contain significantly more calcite. The greater amount of calcite is probably a product of their protection from hypersaline refluxing during high tides.

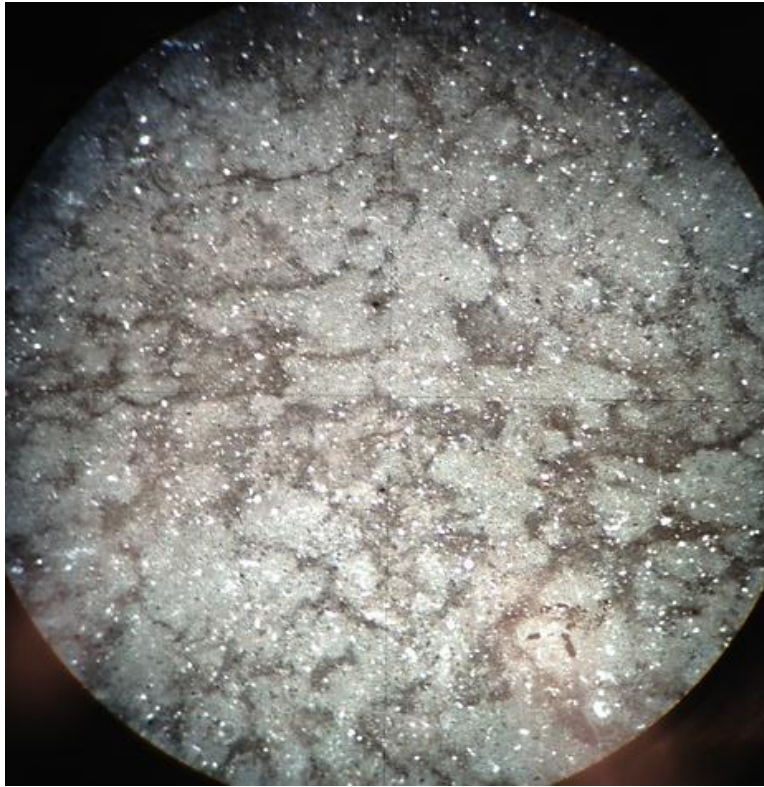


Figure 30: Photomicrograph of sample L1-6125. Mottled fabric of intertidal deposits. 40x
PPL – Diameter of field of view is 4 mm.

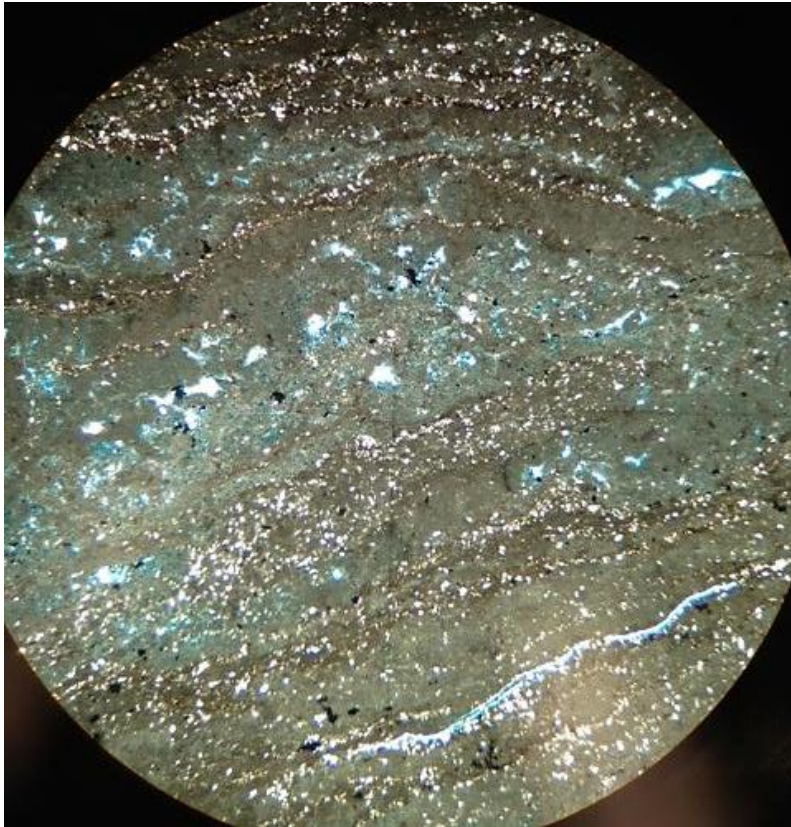


Figure 31: Photomicrograph of finely laminated intertidal deposits bound by an algal mat. Sample L3-6134. 40x PPL – Diameter of field of view is 4 mm. Blue colors indicate pore space.

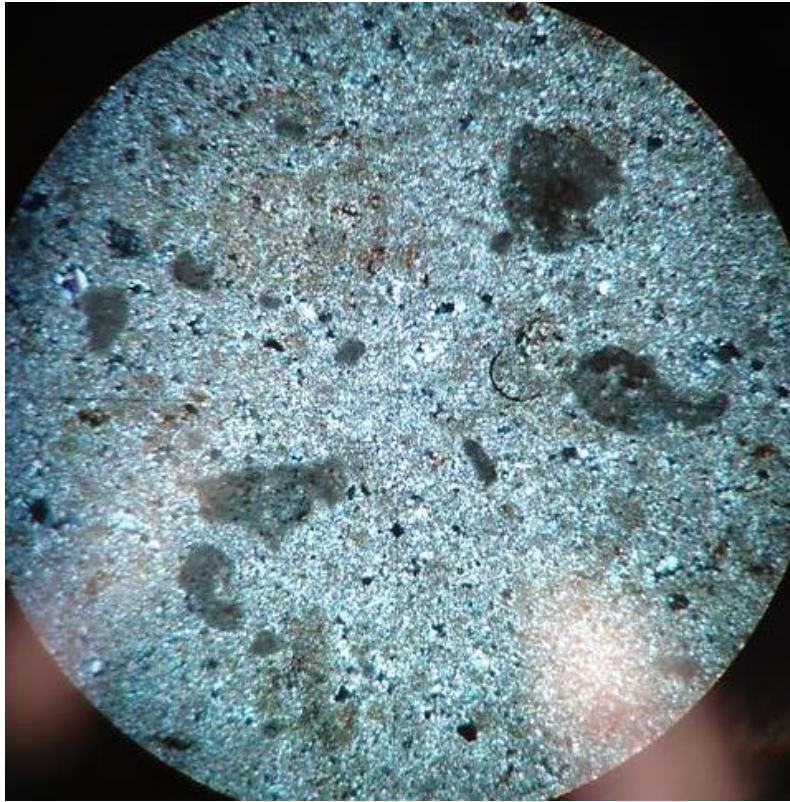


Figure 32: Photomicrograph of intertidal facies with micritized peloids and skeletal grains.

Sample I2-6120. 100x CPL – Diameter of field of view is 2 mm.

Shallow-Subtidal Microfacies

Samples C3-6054, E1-6069, E2-6073, G1-6084, G2-6090, G3-6099, K1-6117 and K2-6126 were all interpreted to be subtidal deposits. However, samples C3-6054, K1-6117 and K2-6126 were determined to be deposited near the intertidal/subtidal margin. The subtidal microfacies all display nearly complete recrystallization as well as subhedral-euhedral dolomite crystals as their matrix (Figures 33, 34 and 35). The subhedral-euhedral dolomite crystals are believed to be a result of protection from eogenetic (early) dolomitization by sea water which lead to burial diagenesis (where crystals could grow larger) later. Lucia (1962) proposes that the shoreline marks the

boundary between the dolomitizing and nondolomitizing environment. Protection from seawater in subtidal environments is opposite from that of tidal-flat environments where brines become hypersaline and most grains are dolomitized early, before burial. Thick sequences of undolomitized carbonate mud accumulated in the subtidal realms, and were later subjected to burial diagenesis. Burial diagenesis and compaction obliterated most of the depositional features in the facies and allowed particles of mud to grow into relatively larger crystals between 1 and 5 μm in diameter.

Rarely, medium to large grains are present in subtidal microfacies but they are recrystallized completely. Most facies are dominated by a crystalline dolomite matrix which is probably recrystallized mud. Subtidal facies also display pore filling and poikilotopic anhydrite (Figure 34). The formation of stylolites in the subtidal facies (Figure 33) further suggests a muddy original lithology and a mechanical component of burial diagenesis, as documented in work by Dickson and Saller (1995). However, conodonts were found still preserved in sample E2-6073 (Figure 34) because they are composed of calcium phosphate (Armstrong and Brasier, 2005) rather than calcite, making them less prone to dissolution. Another important observation in these facies is the large amount of anhydrite precipitated in them.

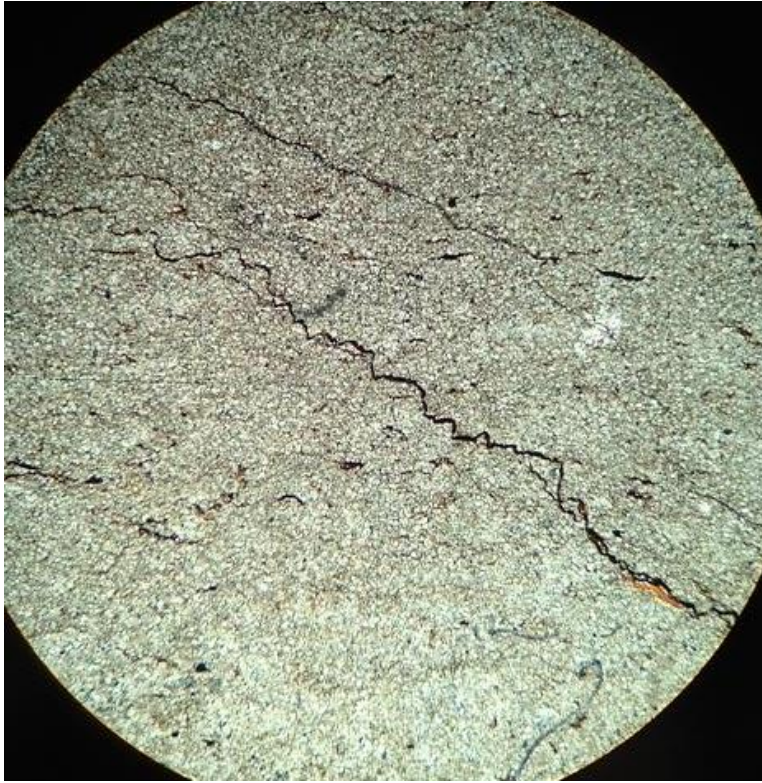


Figure 33: Photomicrograph of stylolites in subtidal facies. Formation of stylolites in crystalline dolomite matrix indicates mechanical compaction and pressure dissolution.

Sample G3-6099. 40x PPL – Diameter of field of view is 4 mm.

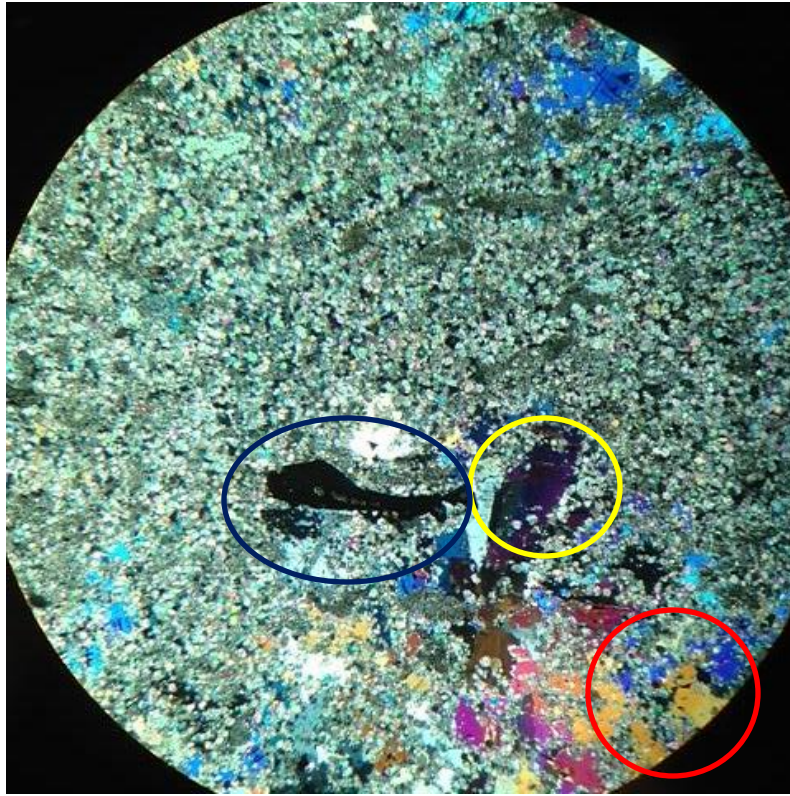


Figure 34: Microphotograph of subtidal facies with black conodont P element (dark blue oval) in a planar subhedral dolomite matrix. High birefringence colors are pore filling (red circle) and poikilotopic anhydrite (yellow circle). Sample E2-6073 40x CPL – Diameter of FOV is 4 mm.

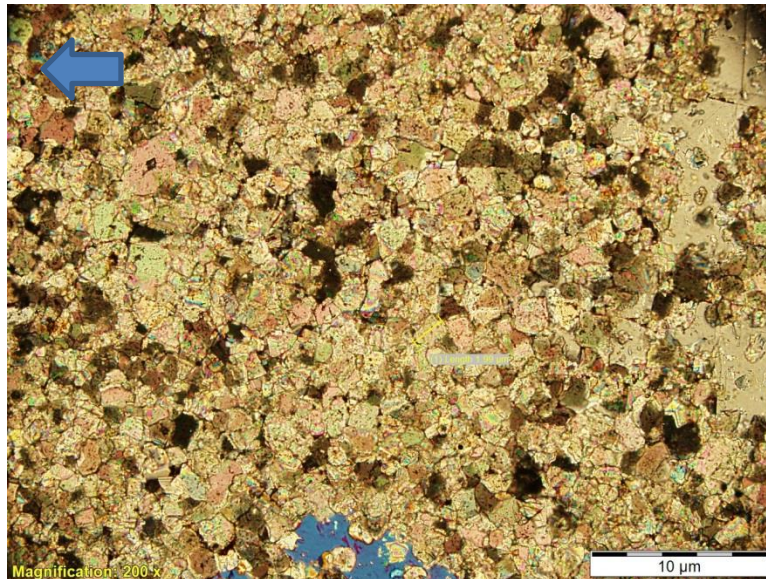


Figure 35: High magnification image of subtidal subhedral/euhedral matrix. Dolomite rhombs are approximately 2 μm in diameter. Sample G2-6090. 200x CPL. Arrow points to depositional orientation.

Diagenetic History of FCU 1947 Core

Results

Diagenesis is defined as all of the changes that happen to sedimentary rocks after deposition and before metamorphism. Within the FCU 1947 core, the three most significant diagenetic events were deemed to be: secondary dolomitization/dolomite cementation (also called overdolomitization), sulfate cementation, and dissolution of grains. These processes significantly altered depositional facies and diagenesis occurred in a cyclic fashion similar to deposition. Less significant events documented from thin section examination were found to be: calcite cementation, fracturing, and the formation of stylolites. These less significant processes had only a minor effect on porosity.

Several mechanisms for diagenesis exist, often in combination with one another. Components of diagenesis include chemical, mechanical and biological processes (Ahr,

2008). The FCU 1947 core appears to be affected by early chemical diagenesis followed by late stage mechanical diagenesis, with biological processes showing smallest amount of diagenetic influence.

The postulated order of identified diagenetic events (Figure 36) from their cross cutting relationships is: 1.) micritization of peloids or grains prior to ultimate deposition, 2.) eogenetic dolomitization from refluxing brines, 3.) sulfate cementation from refluxing brines, 4.) dolomite cementation from refluxing brines, 5.) dissolution or leaching of grains from drops in sea level and rain water percolation, 6.) calcite cementation (minor contribution) from leached calcium rich solutions, 7.) fracturing from structural settling, 8.) second generation sulfate cementation (from deep burial), 9.) stylolite formation from deep burial. The interpreted order was determined from cross cutting relationships from several events identified in multiple thin sections as well as whole-core examination. Controls on diagenesis by their depositional facies are broadly inferred but the relevant relationships between depositional facies and diagenetic events are general and often overlap one another. Therefore, many events are not fabric selective and diagenesis proceeded regardless of facies. Without using techniques such as cathodoluminescence microscopy, epi-fluorescence microscopy, fluid inclusion microscopy, stable isotope, or strontium isotope analysis, it is impossible to prove the timing of each event (Scholle and Ulmer-Scholle, 2003). The three most important diagenetic events within the core are described in the discussion portion of this chapter.

Diagenetic Event	Diagenetic Sequence									
	Syndepositional				Shallow Burial				Intermediate to Deep Burial	
	<i>Eogenetic Stage</i>				<i>Eogenetic Stage</i>		<i>Mesogenetic Stage</i>		<i>Mesogenetic Stage</i>	
Micritization of pellets/peloids										
Dolomitization	Early-stage reflux dolomitization from super saturated evaporite brines									
Dolomite Cementation										
Leaching of Shells						Infiltration of meteoric waters during sea level lowstands				
Calcite Cementation							Minor contribution			
Fracturing							Minor contribution			
Sulfate Cementation/ Evaporite Mineralization	Most abundant in eogenetic stage									
Stylolite Formation										

Figure 36: Diagenetic history of the upper Clear Fork determined from cross cutting relationships.. The different stages are explained in chapter 5. Similar to work from Montgomery (1998).

Discussion

Dolomitization and Overdolomitization (Dolomite Cementation)

Diagenesis often causes what is called dolomitization, in which limestone is altered into dolomite. Dolomitization represents a mineralogical and chemical change from calcium carbonate (calcite, Mg-calcite, or aragonite) to calcium magnesium carbonate (Saller and Henderson, 1998). The generation of dolomite can cause various changes to the initial depositional rock properties. Through dolomitization, porosity and permeability are often significantly altered (Sun, 1995). It is generally believed that dolomitization increases porosity because the process reduces the volume of the rock, resulting in an increase in the volume of the pore space. More recently, Lucia and Major (1994) argue that porosity decreases amid near-surface dolomitization. Within the core and interpreted study area, the most prevalent diagenetic event was concluded to be eogenetic (near-surface) dolomitization. Thin section and grain density analysis document significant alteration of depositional textures and petrophysical attributes. Diagenetic overprint can be attributed to a process known as hypersaline refluxing. Modern analogs of this process can be seen in the Trucial Coast and Qatar, in the Middle East.

The proposed tidal-flat, shallow intertidal, and restricted lagoonal depositional realms all produced an environment ideal for sea water evaporation. As marine water was evaporated, the near surface water became hypersaline which in turn became significantly denser. As proposed by Lucia (1999), the higher density of evaporative brines, coupled with the higher elevation of tidal-flat environments, helps form a hydrodynamic potential, driving the fluids to reflux from the surface into underlying strata where they interact with ground water and replace sea water. High Mg/Ca ratios, induced by both the evaporation of sea water and the precipitation of gypsum and anhydrite,

create a microchemical process which enables the dissolution of calcium carbonate and the precipitation of dolomite. The process of dolomite formation can be expressed in two different equations, which both form end members of a continuous series of possible reactions (Lucia, 1999). The equations proceed as followed:



In a closed system dolomitization should have reduced mineral volume by replacement of aragonite or calcite, further enhancing porosity. However, these closed systems were rare to nonexistent in the refluxing environment proposed. Hence, large volumes of dolomitizing fluids passed through the rocks, creating an open system. Open system conditions introduced not only magnesium, but also dissolved carbonate which precipitated as dolomite cement in what would have otherwise been enhanced porosity. This process is known as overdolomitization but in simple terms is dolomite cementation. The process of dolomite cementation is evident, to some extent, in all thin sections analyzed in this study. Furthermore, grain density analysis show values of 2.80 g/cm³ or greater throughout the core interval. Out of the examined samples, supratidal facies were most extensively subjected to eogenetic dolomitization and related dolomite cementation.

Evaporite Mineralization

A product directly related to the dolomitization mechanism of the upper Clear Fork, anhydrite is the second most common mineral phase identified in this study. Volumetrically, it occludes much of the primary and secondary porosity and is observed in all thin sections. First precipitated as gypsum, increasing temperature and activity of water promote the dehydration of the calcium sulfate into its anhydrous form (Hardie, 1967). Four general types of anhydrite were distinguished in core and thin sections, although some are believed to have formed in combination with one another or may be

considered to be gradational or hybrid forms. Subtidal facies display the largest amount of anhydrite.

Nodular anhydrite (Figures 13 and 23) is found in several intervals of the core. Diagenetic in origin, nodular anhydrite replaces only the volume of rock the nodule encompasses, rather than grains themselves. Nodules often replace only a small percentage of the rock and consequently do not greatly reduce porosity or permeability of the bulk volume.

The most significant form of anhydrite is pore filling anhydrite (Figures 34 and 37). This type spatially occludes intercrystal, vuggy, and moldic pore space, reducing overall porosity substantially (Lucia, 1999). Additionally, the precipitation within intercrystal pore space greatly reduces permeability of the subjected rock.

Formed from a combination of replacement and pore filling mechanisms (Lucia, 1999), poikilotopic anhydrite was identified in several core intervals and thin sections (Figure 34). Ranging in size from less than a millimeter to several centimeters, crystals of poikilotopic anhydrite often possess inclusions of dolomite. Similar to nodular anhydrite, the crystals have an uneven and patchy distribution. Although the formation of this anhydrite does reduce matrix porosity it has been suggested that it enhances reservoir quality. Recently, work by Lucia et al. (2004), documented that the formation of poikilotopic anhydrite actually increases pore throat size, increasing overall reservoir quality, despite lowering total porosity. These findings appear to be consistent with measured permeability values in samples C1-6052, C2-6053, and C3-6054, containing poikilotopic anhydrite, which show relatively higher permeability values than the adjacent rocks (Plate1). However, high values of permeability may actually be attributed to the largely moldic pore system in the C-facies.

In contrast to pore filling and nodular anhydrite types, massive or bedded anhydrite (Figure 23) is depositional in nature and does not significantly alter pore systems. However, due to its extremely low porosity and permeability as well as lateral continuity, bedded anhydrite may be a baffle or impermeable barrier (seal) to migrating hydrocarbons or other fluids. The spatial extent of these beds has a profound effect on reservoir performance and should be carefully mapped and understood to increase efficiency of reservoir sweeps. Fortunately, massive anhydrite beds are identified by distinct well log signatures. Additionally, they may be predicted to occur as capping beds in parasequences of shallowing upwards successions such as those documented in the upper Clear Fork of Fullerton Field (Ahr, 2008). Within the 1947 core, two beds of massive anhydrite greater than 1 foot thick were found at depths 6026' and 6018'.



Figure 37: Photomicrograph of pore filling anhydrite (high birefringence colors) in a dolomite matrix. The anhydrite occludes much of the secondary pore space. Sample G2-6090. 12.5x CPL. Arrow indicates stratigraphically up.

Dissolution

The presence of grain and crystal molds in nearly every thin section demonstrates that dissolution was a significant diagenetic event (Figure 46). Determined to be a product of small sea level changes, dissolution occurred when vast expanses of sediment was aurally exposed and subjected to infiltration of meteoric water. The meteoric water was undersaturated with respect to CaCO_3 and acidic and dissolution continued until equilibrium was reached or the leaching fluids passed through the strata. Though the dissolution fluids likely originated from rain water, the postulated arid

environments did not bring frequent rain and is probably why dissolution is not the most common event. Furthermore, it is probable that aragonite grains were preferentially dissolved because aragonite is more soluble than calcite (Ahr, 2008). Dissolution probably occurred at several times and may or may not have preceded sulfate cementation. For the purpose of this study, supratidal facies show the largest amount of grain dissolution, followed by intertidal facies.

Diagenetic Alteration in Relation to Depositional Facies

Supratidal facies were most prone to dolomitization/dolomite cementation from refluxing hypersaline brines. The refluxing brines also contributed to emplacement of evaporite within the deposits. The dolomitization and cementation of these facies reduced overall porosity. However, supratidal facies also show varying degrees of dissolution from meteoric water which helped enhance reservoir quality.

Intertidal facies were somewhat protected from refluxing brines by normal tides. Partial protection is evident by the relatively larger amounts of calcite compared to supratidal facies. The daily fluctuation of tides helped protect from dolomite and anhydrite precipitation. During sea level low-stands, these facies were exposed to meteoric water infiltration and resultant calcite or aragonite dissolution, similar to supratidal facies, which contributed to better reservoir quality.

Subtidal facies were the poorest reservoirs. The realm in which they were deposited protected them from surface dolomitization and early sulfate cementation. Because these deposits were not dolomitized early, they were more prone to compaction. The large volumes of hypersaline water in their muddy deposits, and prolonged contact with the fluids during burial diagenesis, generated more anhydrite precipitation, obliterating pore space.

Chapter 5

Porosity

Pore Types

Results

Table 2 outlines major micro and macropore types determined from thin section examination. Using the classification scheme from Choquette and Pray (1970), three common pore types were identified, and five minor types.

Discussion- Major Pore Types

The Choquette and Pray (1970) classification of pore types is a long established scheme that is frequently used in petroleum geology as well as by most carbonate petrographers. The classification scheme links, as closely as possible, pore types to depositional and diagenetic facies, otherwise known informally as carbonate “fabrics”. Only this classification scheme was used in this study. An initial macroscopic examination of core was conducted to determine macropore types. No macropores were found within the entire cored interval with the exception of very small (<1 mm) molds in the grainstone intervals identified with a 10x hand lens. It is an important observation to note that significant diagenetic alteration, as mentioned in Chapter 4, destroyed nearly all depositional porosity, leaving an almost entirely secondary pore system.

Dominant and volumetrically abundant pore types in thin sections were determined to be moldic (grain and skeletal), intercrystalline (matrix), and vugs. Less abundant types identified in thin sections were fenestral, fracture, boring, intracrystalline and shrinkage pores. Whereas several different types of pores were identified, it is important to note that many of the pores are hybrids of several pore types produced by the sequences of diagenetic events mentioned in chapter 4 and illustrated in Figure 36.

Most of the proposed events caused the occlusion of secondary pores and destroyed most primary and secondary reservoir porosity.

Moldic Pores

Moldic pores were determined to be the most abundant type. Categorized as secondary pores, moldic pores formed from the complete, partial, or selective dissolution of grains or crystals (Lonoy, 2006). Abundant moldic pores were identified in 14 of the 21 samples in this study (Figure 46). Molds in the samples were formed by dissolution of skeletal grains, peloids, foraminiferal tests, evaporite crystals, and possibly early stage dolomite crystals. Most molds in the samples went to complete dissolution but several samples such as A1-6042, B1-6046 (Figures 40 and 41) and B2-6048 have grains that are only partially leached (dissolved). Dissolution was likely preferential to aragonite grains and could explain why grains juxtaposed to one another show inverse degrees of dissolution. More often, molds show complete dissolution and were later filled by either dolomite or sulfate cement (Figure 39). The formation of moldic pores is believed to be a fabric selective process (Saller et al., 1994). An important characteristic of the moldic pores is their lack of connectedness with nearby pores. The isolation of the pores explains the low permeability of samples.

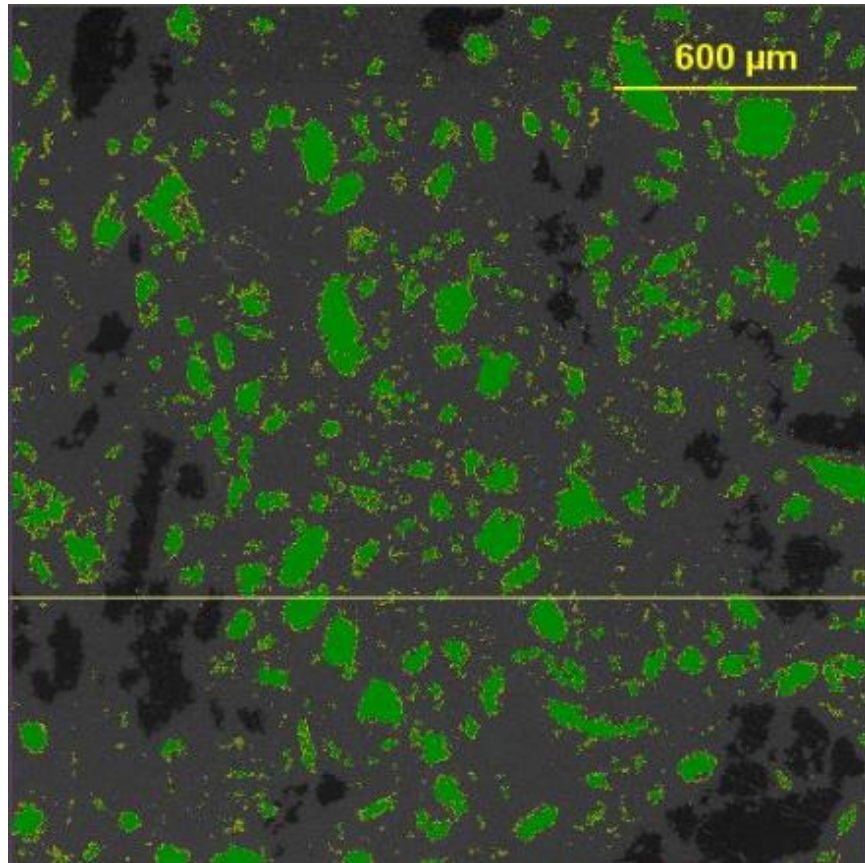


Figure 38: SEM photo of grain and peloid dissolution molds. Green is pore space. Sample C2-6053 at 75x magnification. Dark black areas were determined to be pore filling anhydrite.

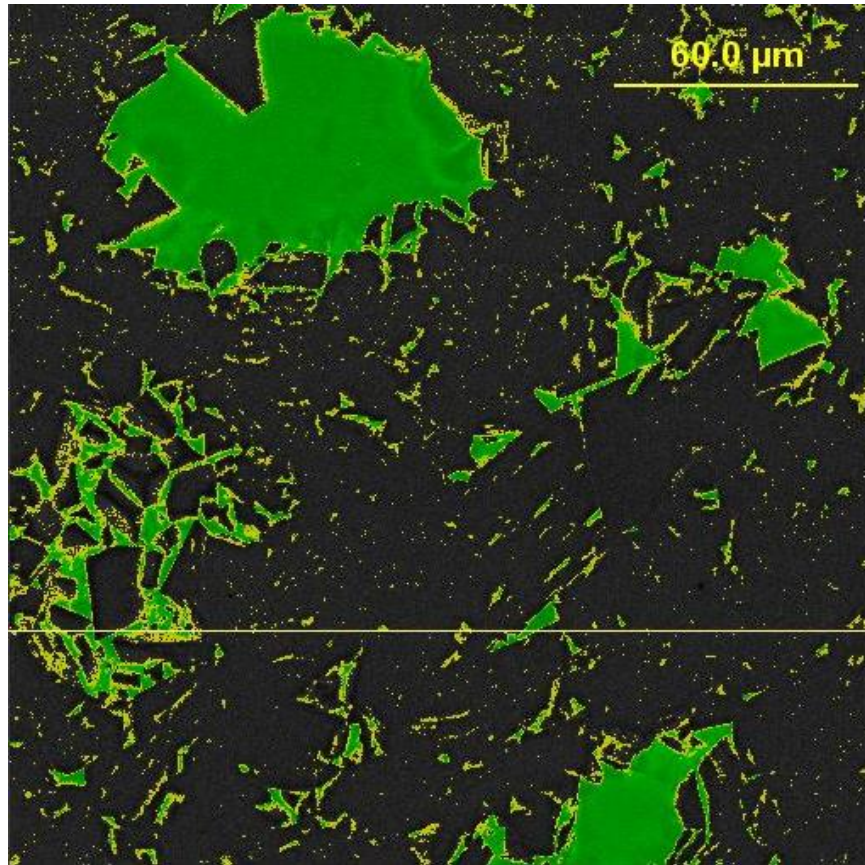


Figure 39: SEM photo sample of moldic pore with dolomite cement rhombs lining pore walls. Sample C1-6052 at 750x. In some cases the pore is nearly completely occluded by dolomite or sulfate cement. Pore space is green.

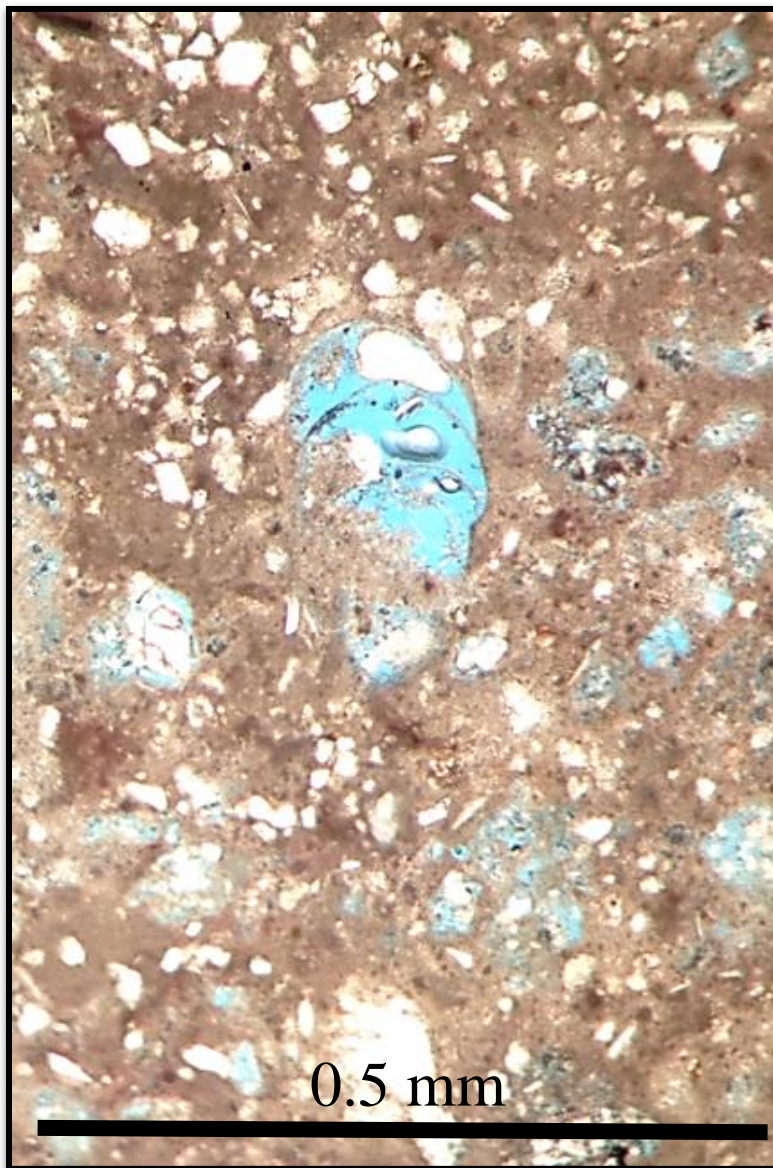


Figure 40: Photomicrograph of partial dissolution of grains and later stage obliteration of shelter porosity within a foraminifer test by dolomite cryptocrystalline cement sample.

Pore space is blue. Sample B1-4046 PPL 100X.

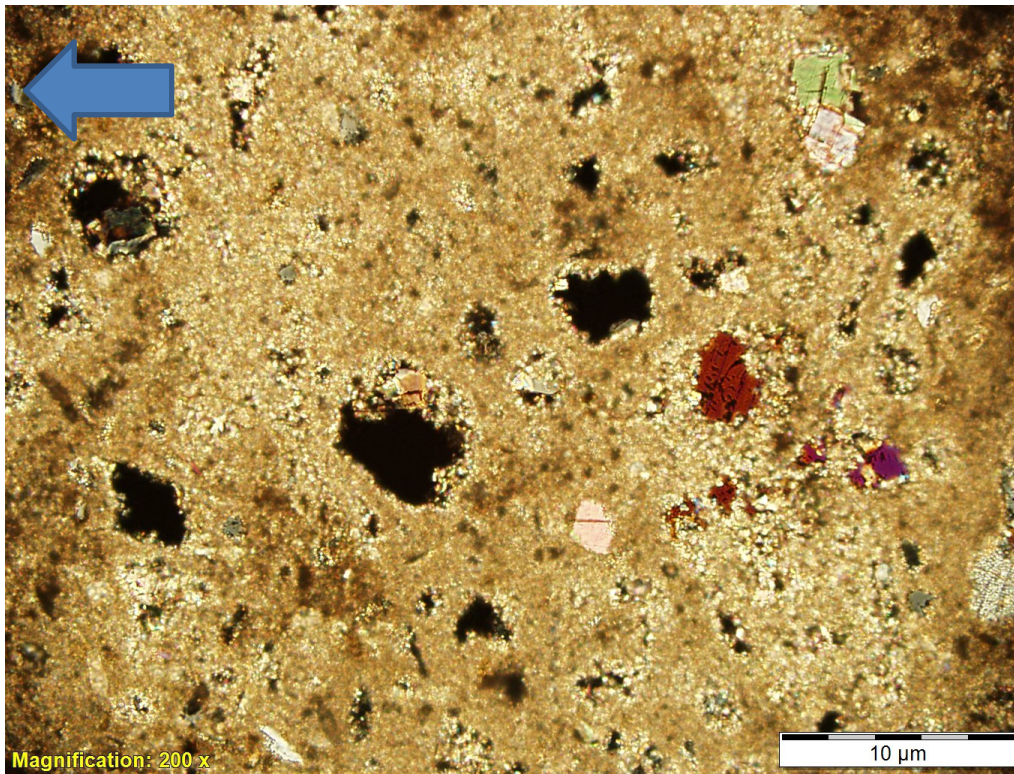


Figure 41: Photomicrograph of moldic porosity partially reduced by dolomite cement in multiple stages. Red grain in right center of photo is calcite (Alizarin stain), suggesting preferential dissolution of grains. Sample B2-6048 CPL 200x. Pore space is black.

Intercrystalline Matrix Pores

Choquette and Pray (1970) documented that intercrystalline porosity may be of either primary or secondary origin. However, of the samples examined in this study, all crystals in which pore space is adjacent to, were diagenetic and therefore are secondary in nature. The pore space found between these crystals is the most volumetrically abundant, yet smallest pore type, as determined from high magnification SEM analysis. Porosity was found between cryptocrystalline and microcrystalline dolomite cement rhombs. The crystallization of the dolomite rhombs decreased the size of the original mud

particles and created pore space between them, in what appear to be fracture filaments (Figure 42). Lonoy (2006) categorized these types of pores as mudstone microporosity. Saller et al. (1994) note that intercrystalline porosity can also be created by dissolution of the micritic matrix. A crucial observation of these pores in thin sections is that they appear to be linked together and probably add connectivity to matrix porosity.

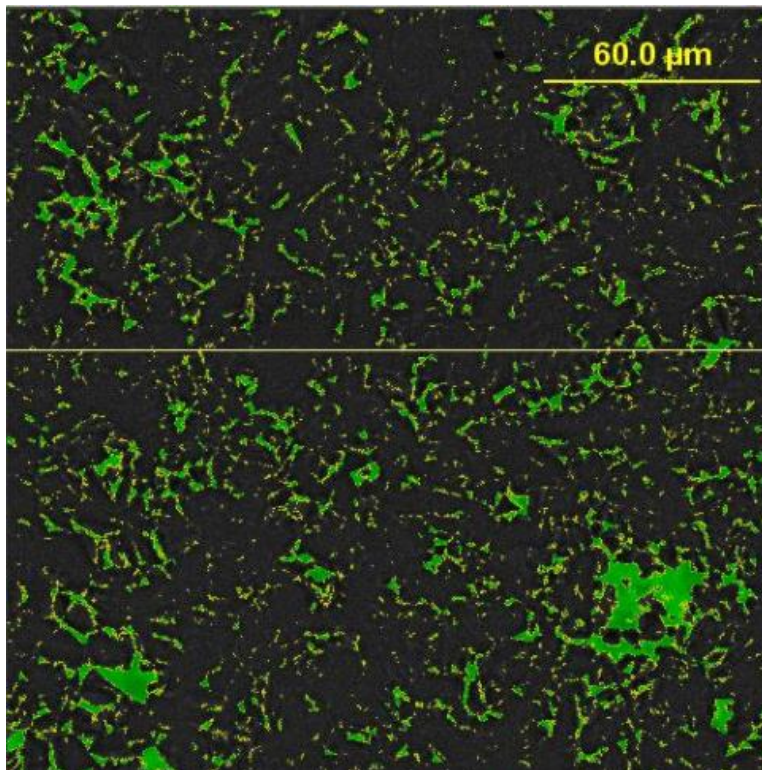


Figure 42: SEM photo of intercrystalline matrix porosity and fracture filaments. Green is pore space. Sample E1-6069 at 750x. Matrix porosity nearly invisible using optical microscopy.

Solution Enlarged/Reduced Vuggy Pores

Vugs examined in thin sections likely originated from gas bubbles or from shrinkage and formed at or contemporaneously with deposition as postulated by Shinn

(1968, 1986). The vugs in thin sections are likely hybrid in nature. Vugs can form from solution-enlarged fractures, molds, intercrystal, and fenestral pores as noted in Choquette and Pray (1970). The hybrid or gradational attributes of these pores makes them difficult to categorize and distinguish as they often overlap other pore types. The alteration of vugs is believed to be a non-fabric selective diagenetic process (Saller et al., 1994). Most vugs in thin sections have been enlarged by diagenetic fluids (solution) but some have been occluded. In most samples, vugs originated from moldic or fenestral pores (Figures 43 and 44).

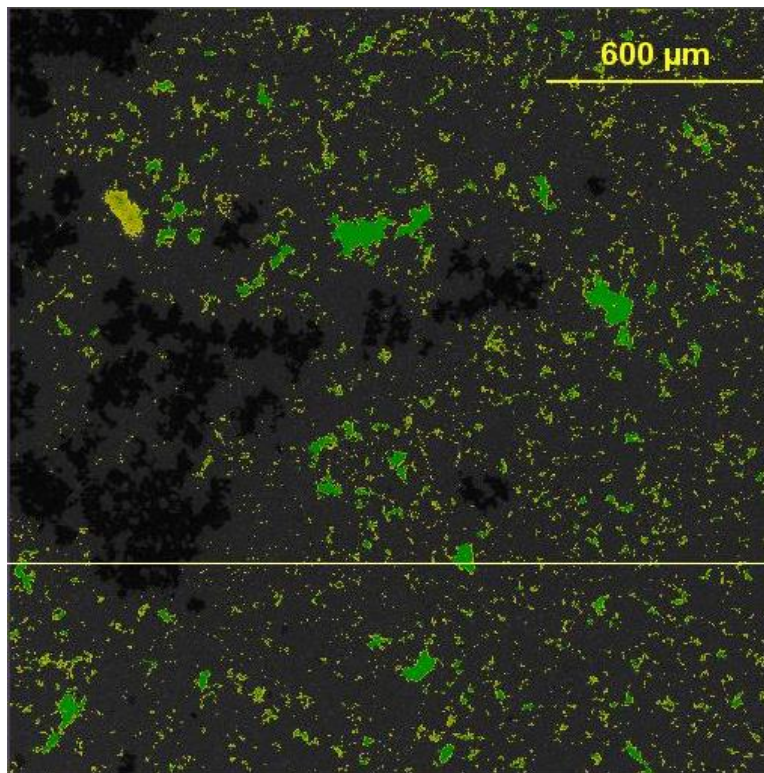


Figure 43: SEM photo of solution enlarged vugs (larger) and intercrystalline porosity (smaller pores). Sample G1-6084 at 75x magnification. Darker black areas determined to be pore filling anhydrite.

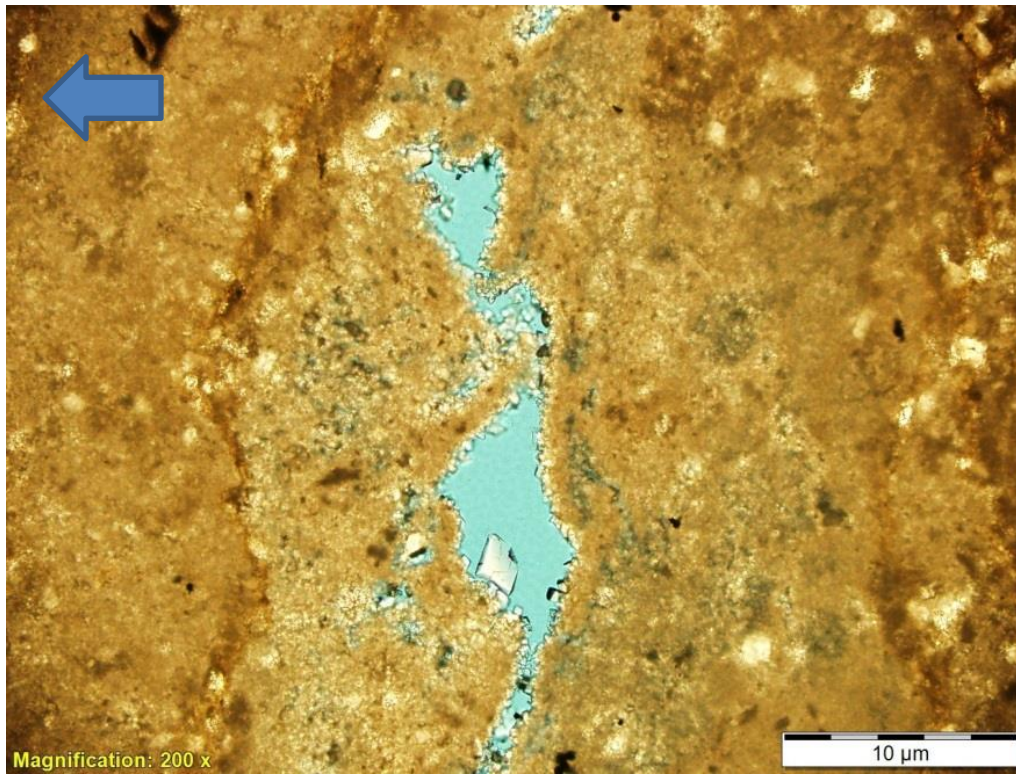


Figure 44: Photomicrograph displaying complex pore evolution. Pore space (blue) originated as a fenestral pore enlarged by meteoric solutions during early burial then reduced by dolomite cement during at least two different time intervals (small and large dolomite rhombs). Sample L3-6134 200x PPL.

Primary Porosity Development

Primary porosity encompasses both syndepositional and depositional porosity. Syndepositional porosity can be thought of as any pore space formed when the material is precipitated (either biogenically or chemically). Examples of porosity include biological formation of chambers, precipitation of an accreting growth framework, and intraparticle voids of tests (shells). Pore space formed during the time the layer was deposited is considered depositional porosity (Choquette and Pray, 1970). In carbonate mud,

depositional porosity may be more than two thirds of the total volume. In coarser sediment, depositional porosity typically contributes around one third of the overall volume (Choquette and Pray, 1970). In the examined thin sections, depositional porosity within muddy intervals may have contributed significantly to primary porosity, but mechanical compaction and burial diagenesis more or less transformed the pore system into one that is characterized as secondary in nature. Ahr (2008) concludes that tidal-flat environments have only limited potential for porosity because of the mud-rich nature of their systems (and destruction of depositional porosity).

Secondary Porosity Development

Secondary porosity is defined by Choquette and Pray (1970) as any porosity formed after deposition. They proposed three different burial stages, which each yield a unique alteration of the pore system. The three stages are eogenetic, mesogenetic, and telogenetic. The eogenetic stage refers to early burial, and applies to the time interval between deposition and the burial of the deposits at or below the depth of influence of surface processes. The mesogenetic stage is the time interval from the eogenetic stage to the final time of when surface processes once affect the deposits (from uplift). The telogenetic stage is the time interval in which long buried deposits are influenced substantially by processes associated with a forming unconformity after uplift. Because both the eogenetic and telogenetic stage are influenced by surface processes, it can be difficult to distinguish between the two. However, karsting, and dedolomitization of sediments are a common feature of the telogenetic stage.

From examination of thin sections and core, it was determined that most alteration of the pore system occurred in the eogenetic realm. The formation of moldic pores likely occurred at or near the surface from percolating rain water during drops in sea level. The dolomitization, and evaporite precipitation of supratidal and intertidal facies

also occurred in this stage. Dolomitization in the eogenetic stage probably created the intercrystalline pores in the matrix. Intercrystalline pores were probably modified to some extent in the mesogenetic realm as well. Vuggy pore types are also thought to have occurred in both the eogenetic and mesogenetic stage. Early stage gas bubbles likely altered eogenetic depositional pores but solutions formed in or transported through the sediment in the mesogenetic stage probably modified vugs again.

In contrast, the dolomitization of subtidal facies is believed to have occurred in the mesogenetic stage. Intercrystalline pores between subhedral/euhedral dolomite rhombs are thought to have formed from burial diagenesis. As mentioned in chapter 4, the presence of stylolites indicates these deposits were subjected to chemical compaction during burial. In the FCU 1947 core, no dedolomitization or karsting was observed so deposits are believed to not have gone through the telogenetic stage.

SEM Image Analysis

Results

Figure 46 summarizes the porosity data from the SEM image analysis of all 21 samples as well as their measured gas expansion porosity for the entire foot of core in which the thin sections were taken. A crossplot of SEM porosity versus gas expansion porosity is shown in Figure 45. An r^2 coefficient of 0.07 was determined from the cross plot. The low coefficient value indicates very little correlation between the two measurements. Probable causes for the remarkably low coefficient are discussed in the limitations and considerations portion of this chapter.

Pore size distributions for each individual sample are shown in Figures 47-50. Crossplots of micro, macro, and total pore shape versus permeability are shown in Figures 51-53. Cross plots of total, micro and macro porosity versus permeability are

found in Figures 54-56. Individual sample pore size distributions, SEM photo examples of pore types, and a photo of the core sample can be found in Appendices B.

Anselmetti et al. (1998) defined the boundary between microporosity and macroporosity to be a pore area of 500 microns squared. It is important to note that this is a different definition of microporosity from that of the British Standards Institute. The British Standards Institute classifies a micropore as a pore size (in diameter rather than area) less than 2 nm. The stage file created for this study omitted anything with a pore area of less than $0.5 \mu\text{m}^2$. The omission of pores less than $0.5 \mu\text{m}^2$ was done because the polish compound used on thin sections was a 1 μm grit. Therefore, "pores" analyzed smaller than that would likely be imperfections of the slide. "Pore size" in the distribution charts of this study and in the discussion were found by taking the square root of the pore area divided by pi. The mention of pore size refers to a linear value for an average pore length. The pore size distributions are plotted in histograms with discrete steps of the six pore size classes. For example, all pores with an area of between 0.5 and $5 \mu\text{m}^2$ fall in the pore size class of 1 μm . All pores between 5 and $50 \mu\text{m}^2$ fall into a pore size class of 3.2 μm and so on.

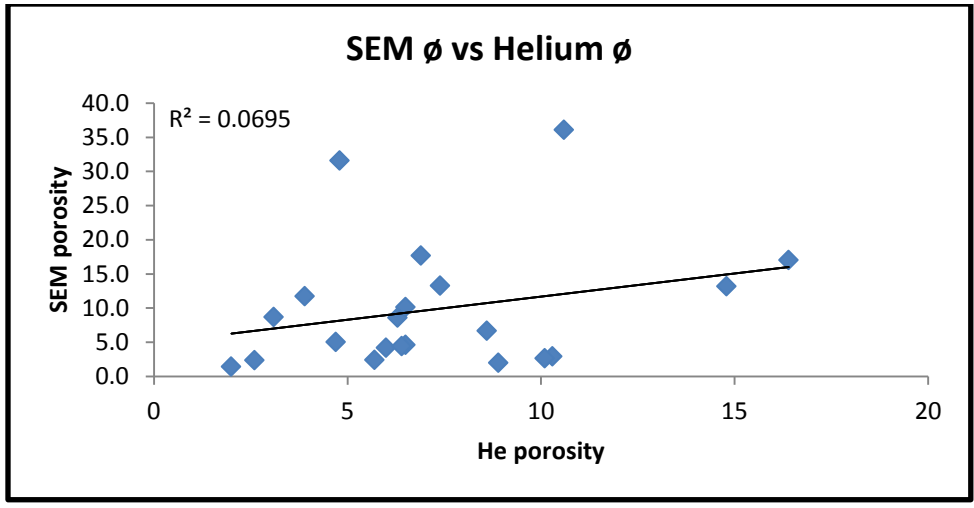


Figure 45: Crossplot of SEM porosity versus gas expansion Helium porosity.

Digital Image Analysis

Sample Label	SEM 8 point		Micropore	Macropore	Main Micropore Type	Main Macropore Type	Micropore Shape Parameter	Macropore Shape Parameter	Overall Shape Parameter	Max Perm (md)
	He ϕ	total ϕ	%	%						
A1-6042	10.6	36.1	35.8	0.3	Intercrystal Matrix	Vuggy	3.9	2.0	3.9	0.02
B1-6046	14.8	13.2	9.4	3.9	Intercrystal/Vug Matrix	BioMolds/Grain Dissolution Molds	2.0	2.0	2.0	0.03
B2-6048	16.4	17.0	15.6	1.5	Intercrystal/Vug Matrix	Grain Dissolution Molds	3.8	1.6	3.8	0.17
C1-6052	4.7	5.0	2.6	2.4	Intercrystal/Molds	Grain Dissolution Molds	1.8	1.8	1.8	0.89
C2-6053	3.9	11.7	2.3	10.5	Intercrystal/Molds	Peloid Grain Molds	1.9	1.9	1.9	2.2
C3-6054	7.4	13.3	12.5	0.8	Intercrystal/Molds	Molds/Vuggy	3.2	2.0	2.9	0.06
E1-6069	3.1	8.7	2.0	7.3	Intercrystal Matrix	Intercrystal	1.8	3.7	3.5	0.02
E2-6073	2.6	2.3	1.8	0.5	Intercrystal Matrix	Intercrystal	2.0	2.0	2.0	0.03
G1-6084	6.5	4.6	3.0	1.6	Intercrystal Matrix	Grain Dissolution Molds/Vuggy	1.8	2.1	2.0	0.15
G2-6090	2	1.4	1.3	0.1	Intercrystal Matrix	Vuggy/Intercrystal	2.6	2.7	2.6	0.21
G3-6099	6.5	10.1	6.6	3.7	Intercrystal Matrix	Solution Enlarged Vugs	2.1	2.4	2.3	0.74
I1-6116	10.3	2.9	2.0	1.0	Intercrystal/Molds	Intercrystal/Molds/Fracture	1.8	2.3	2.2	0.02
I2-6120	8.6	6.6	5.3	1.4	Intercrystal Matrix	Intercrystal/Molds	3.0	2.1	2.5	0.02
I3-6143	10.1	2.7	1.9	0.8	Intercrystal Matrix	Intercrystal	2.1	2.2	2.1	0.01
K1-6117	4.8	31.6	31.5	0.04	Intercrystal Matrix	Vuggy	2.7	2.0	2.7	0.01
K2-6126	6.9	17.7	16.9	0.7	Intercrystal Matrix	Molds/Intercrystal	2.8	1.8	2.7	0.01
L1-6125	5.7	2.4	2.2	0.2	Intercrystal/Molds	Intercrystal/Grain Molds	2.1	1.9	2.1	0.05
L2-6127	6	4.2	2.1	2.1	Intercrystal/Molds	Grain Dissolution Molds/Vuggy	1.9	1.9	1.9	0.03
L3-6134	6.3	8.6	8.3	0.3	Intercrystal Matrix	Grain Dissolution Molds/Vuggy/Fracture	2.3	2.0	2.3	0.01
M1-6128	6.4	4.4	3.5	0.9	Intercrystal Matrix	Molds/Vuggy Intercrystal	1.8	1.7	1.8	0.14
M2-6137	8.9	2.0	1.5	0.5	Intercrystal Matrix	Intercrystal/Molds	2.1	2.0	2.1	0.01

Figure 46: Image analysis porosity results. Highlighted cells indicate samples with equal to or greater than 0.03 md permeability.

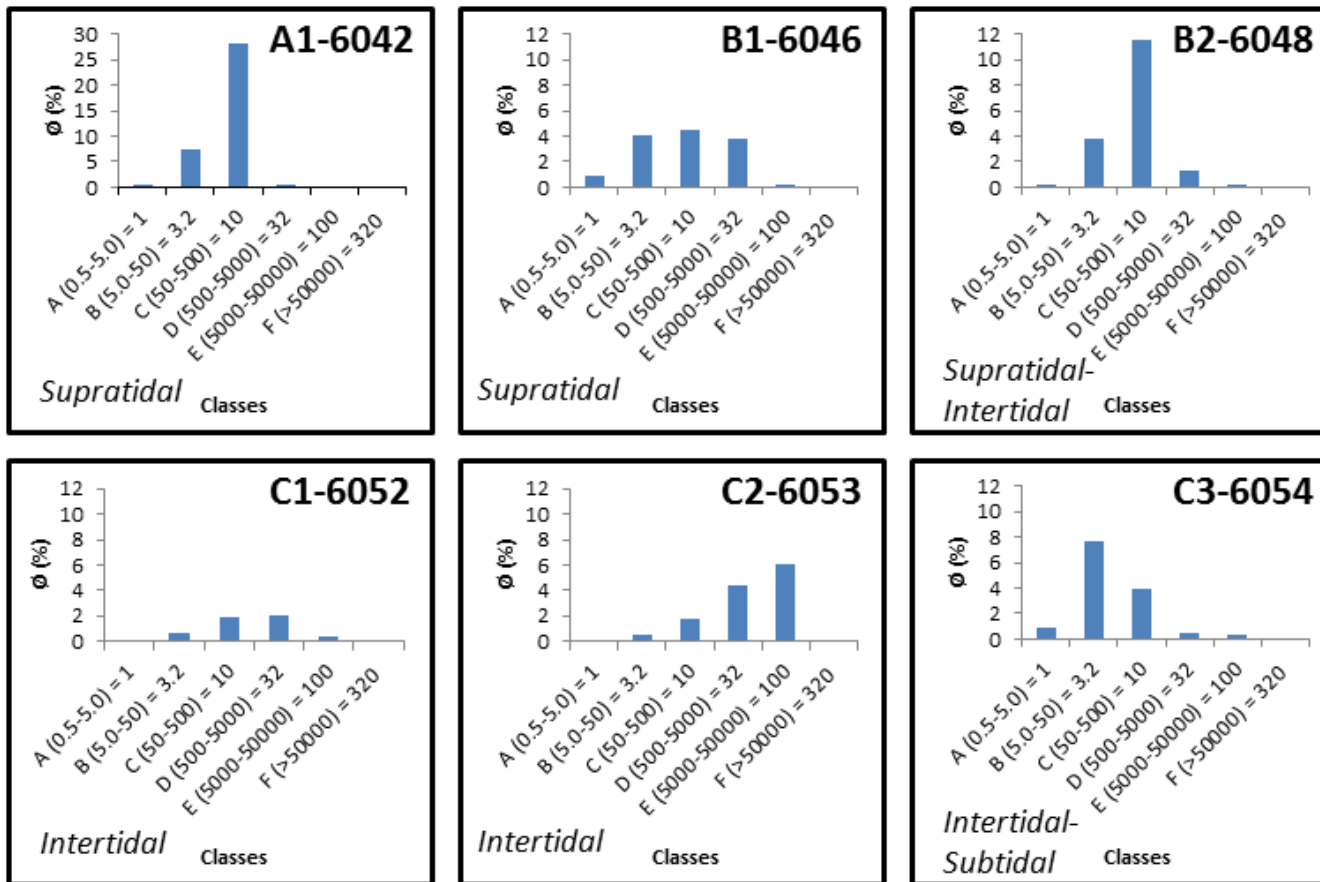


Figure 47: Pore size distributions from A1-6042, B1-6046, B2-6048, C1-6052, C2-6053, C3-6054. A1-6042 has a different vertical scale to fit bar chart.

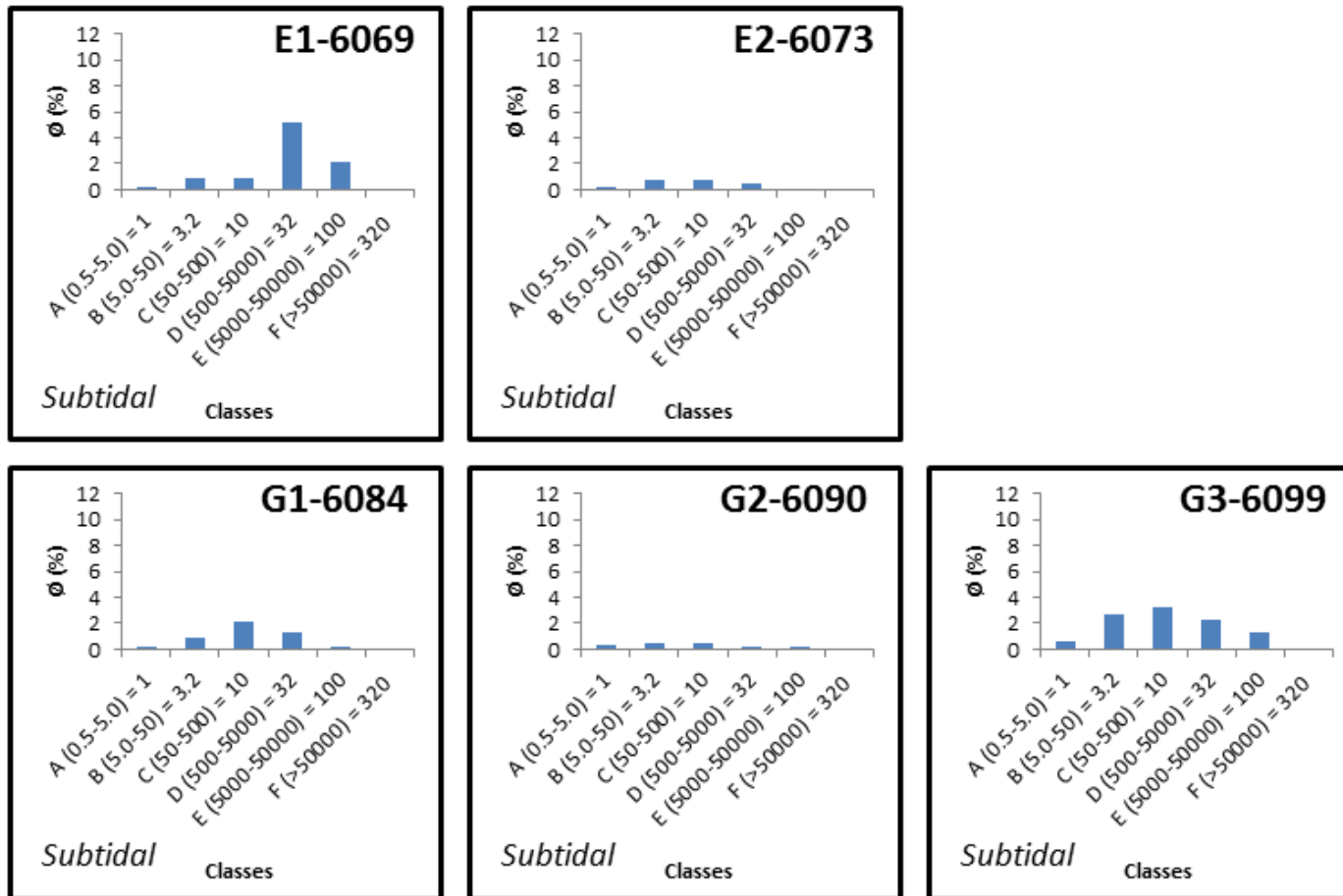


Figure 48: Pore size distributions from subtidal samples E1-6069, E2-6073, G1-6084, G2-6090, G3-6099.

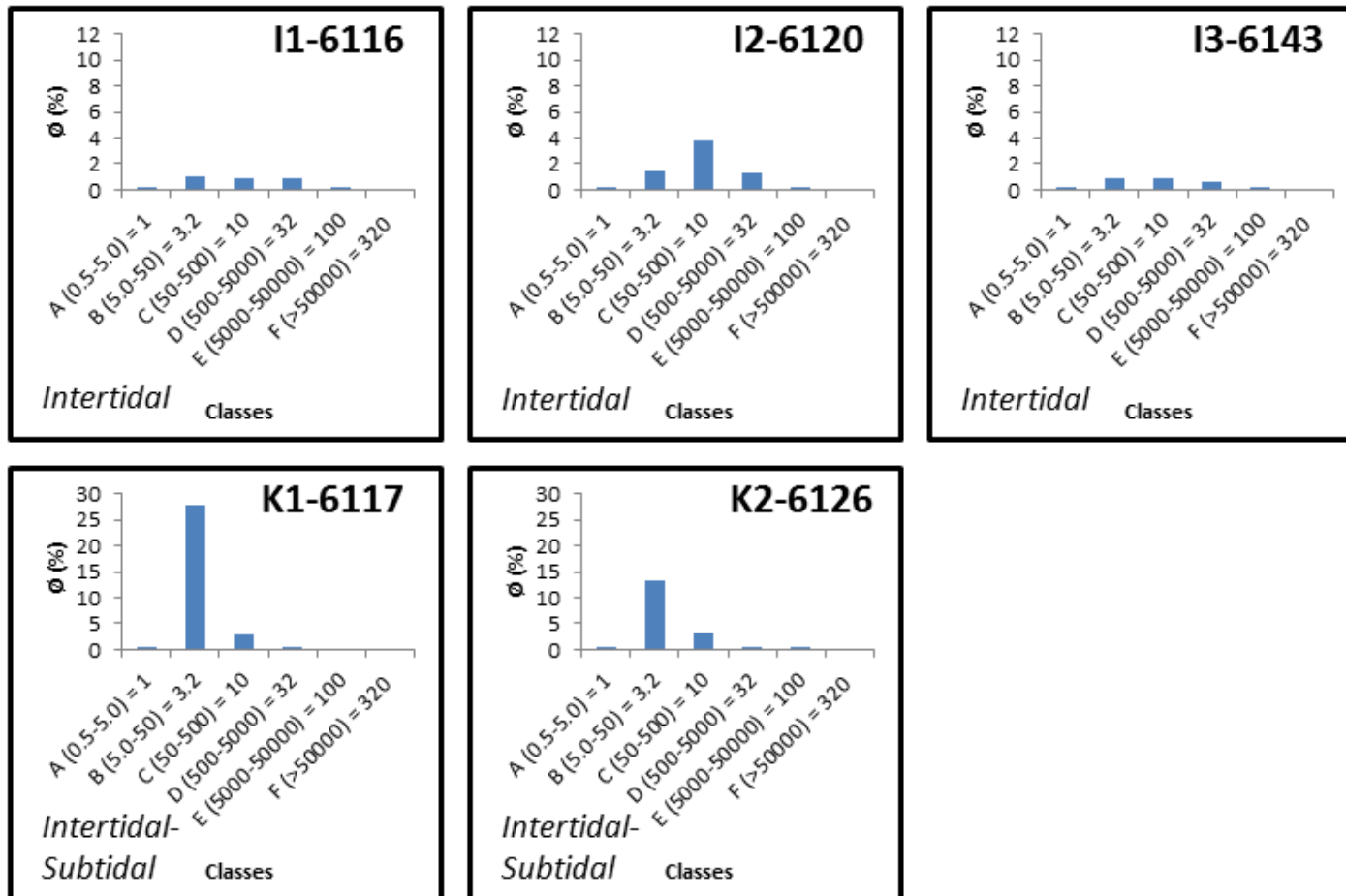


Figure 49: Pore size distributions from I1-6116, I2-6120, I3-6143, K1-6117, K2-6126. K1-6117 has different vertical scale.

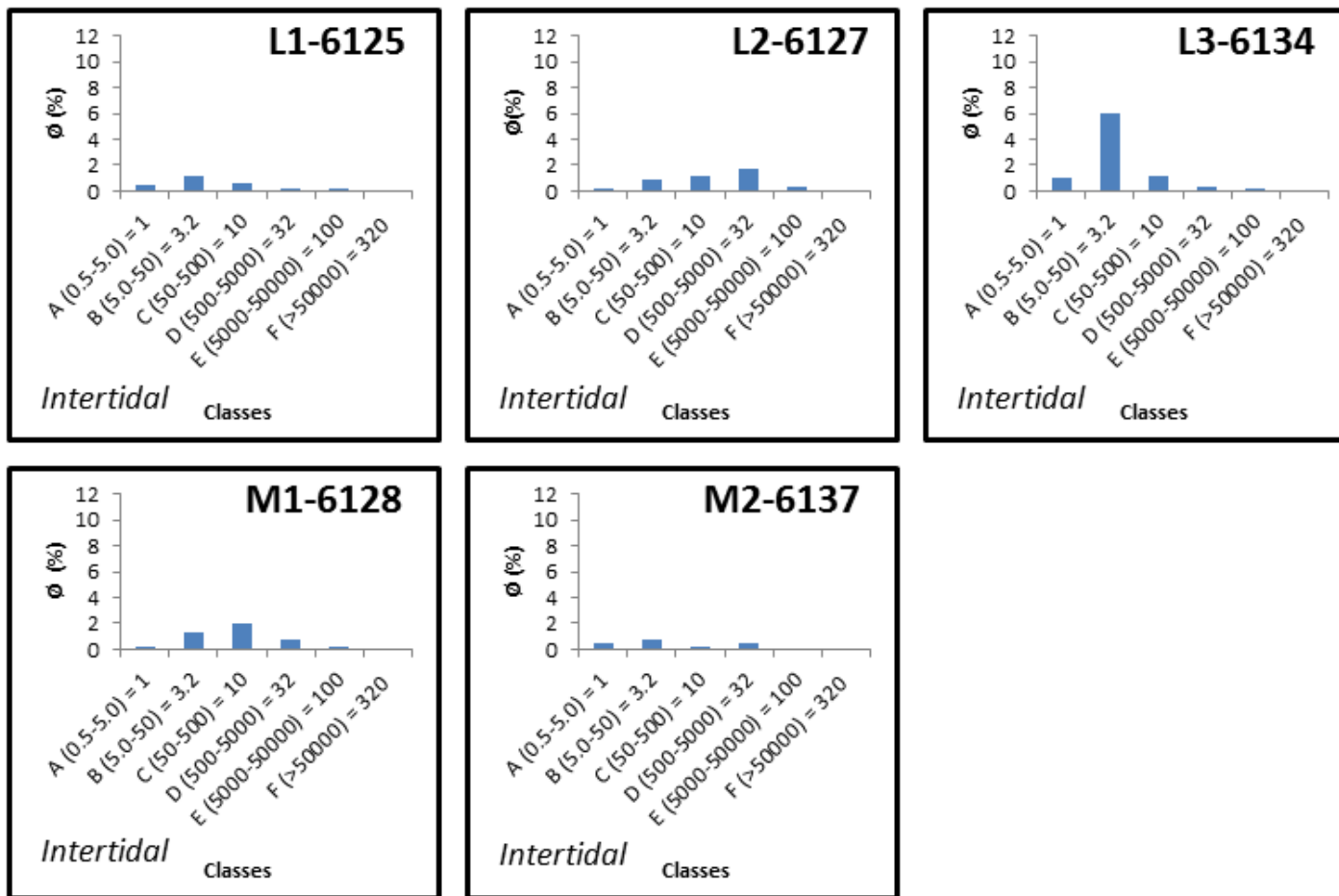


Figure 50: Pore size distributions from intertidal samples L1-6125, L2-6127, L3-6134, M1-6128, M2-6137.

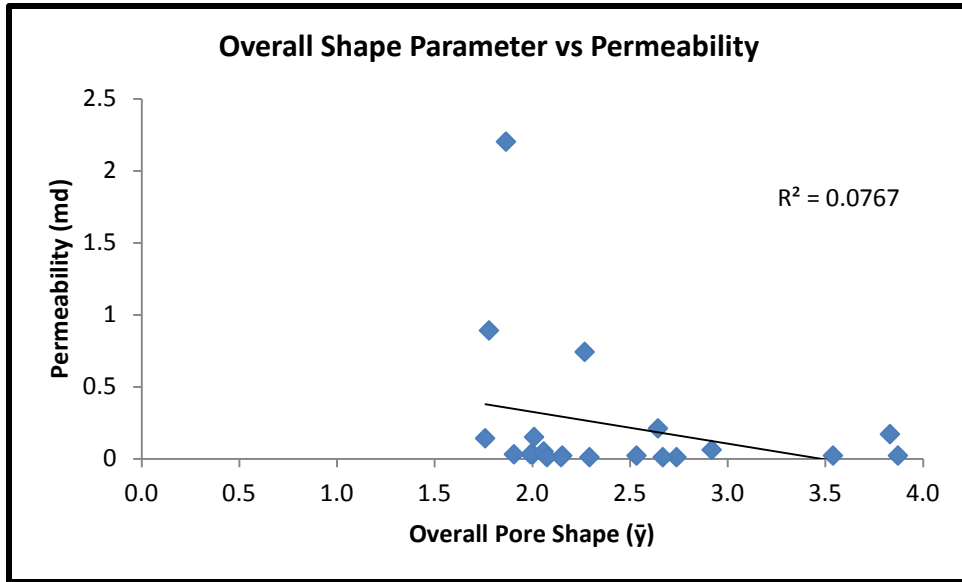


Figure 51: Crossplot of permeability versus overall pore shape parameter ($\bar{\gamma}$).

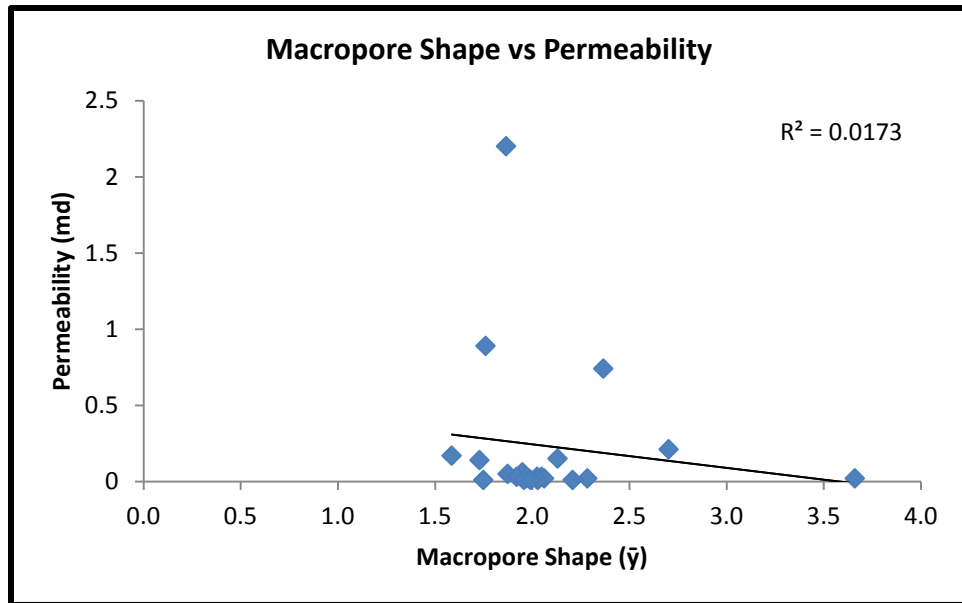


Figure 52: Crossplot of permeability versus macropore shape parameter ($\bar{\gamma}$).

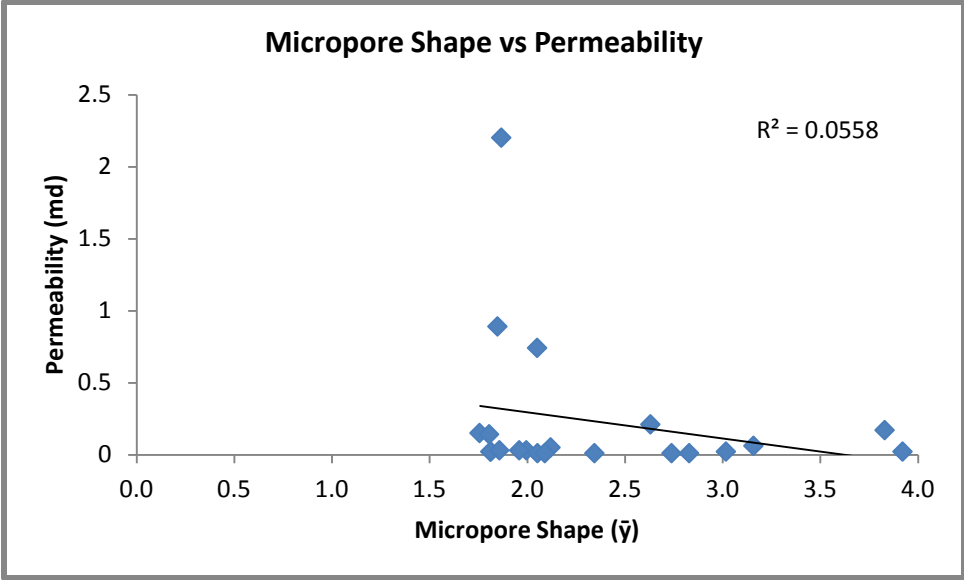


Figure 53: Crossplot of permeability versus micropore shape parameter ($\bar{\gamma}$).

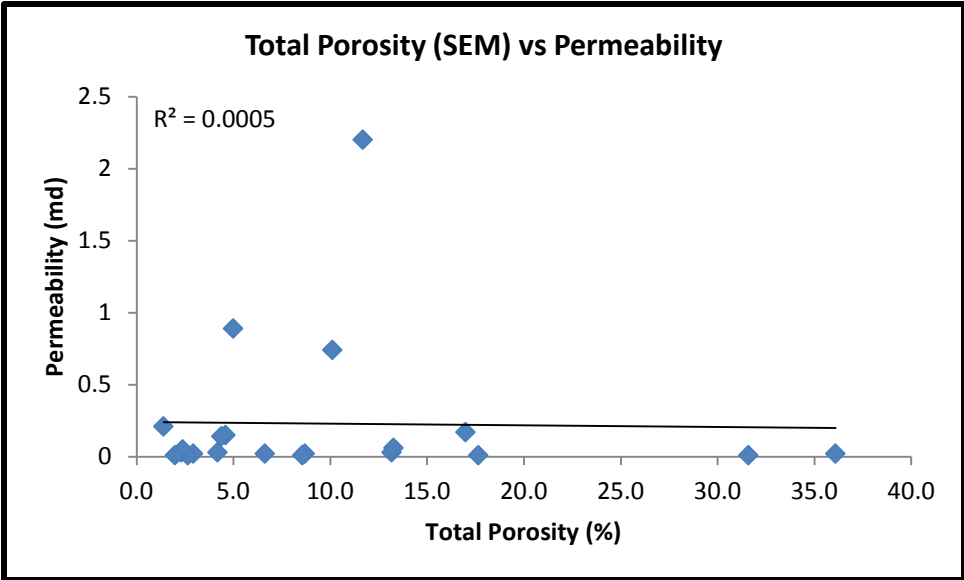


Figure 54: Crossplot of permeability versus (SEM) total porosity.

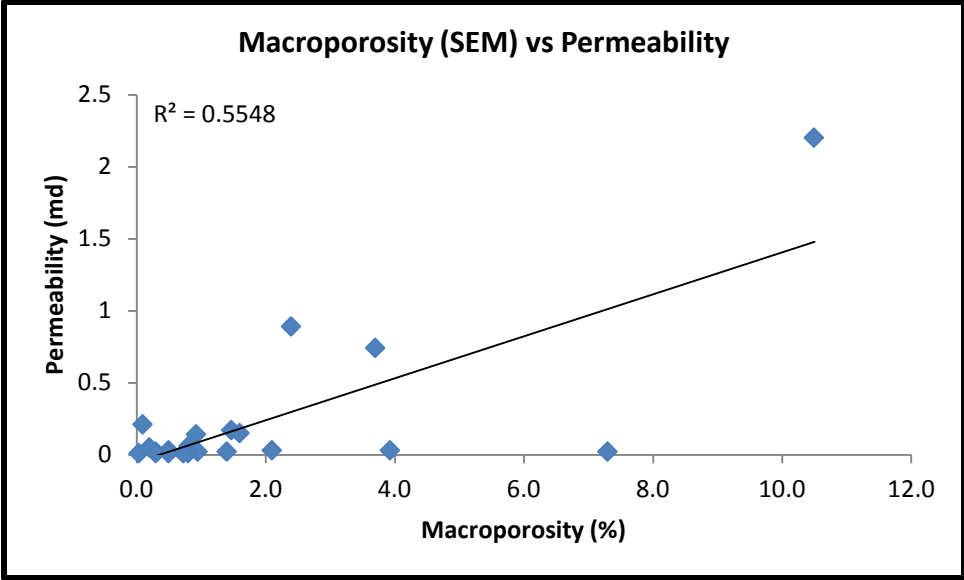


Figure 55: Crossplot of permeability versus (SEM) macroporosity.

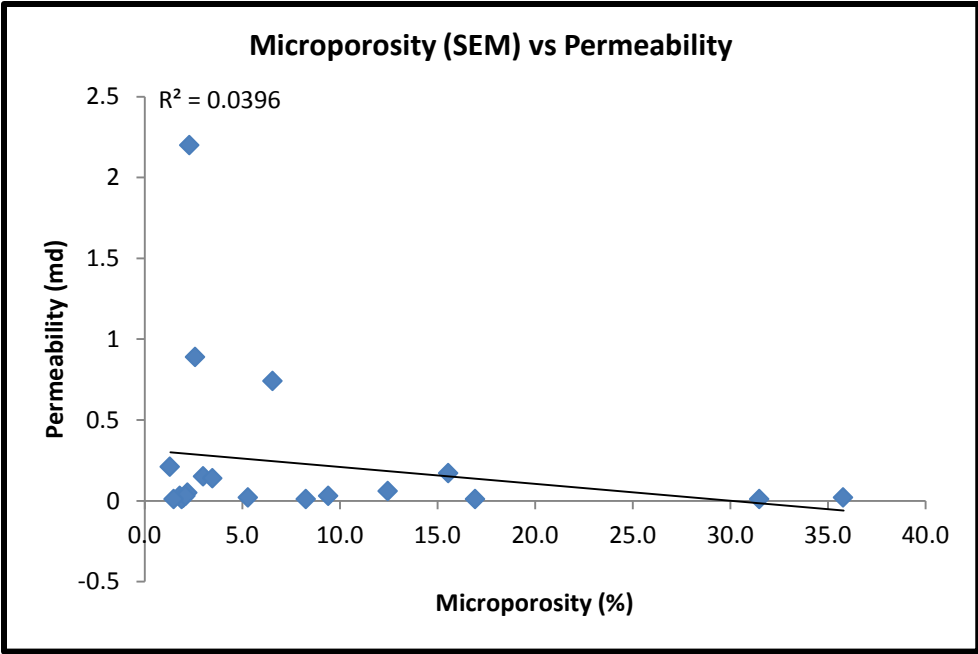


Figure 56: Crossplot of permeability versus (SEM) microporosity.

Discussion

Pore Size Distributions with Relation to Lithofacies

An overall evaluation of pore size distributions from all samples showed two similar trends with every sample. Pores between 0.5 and 5.0 μm^2 regardless of their abundance, had very little contribution to overall porosity, usually much less than 1 percent of total porosity. The small pores were determined to be intracrystalline or intraparticle, probably imperfections formed during the mineralization of the dolomite in the eogenetic or mesogenetic realm, or before the layer were deposited. Because the smallest class of micropores is so insignificant in relation to pore volume, it is safe to assume they do not contribute to reservoir performance and therefore can be omitted from further evaluation. Moreover, no pores greater than 50,000 μm^2 were located during the SEM analysis. This observation was expected in the samples as they were dominantly mudstone/wackestone/packstone; thus large interparticle, intercrystal and skeletal growth/framework pores were not expected. The absence of larger pores is consistent with both qualitative micro and macro examination of samples.

The original hypothesis in this study was that similar lithofacies would show similar pore size distributions independent of stratigraphic position. Preliminary macroscopic descriptions of core were used in the identification and segregation of different lithofacies. Samples (thin sections) were then taken from similar macroscopic facies. As mentioned previously, the letter in each sample label corresponds to a unique lithofacies (determined macroscopically) and the number is the depth from which they were taken in feet of measured depth. For example, all samples of B were determined macroscopically to be similar lithofacies. However, when lithofacies were examined in microscopically, they varied from their macroscopic descriptions in some cases. Many facies originally characterized as mudstone were microscopically determined to be

wackestone due to the presence of fine skeletal grains ($\approx 20 \mu\text{m}$) beyond the resolution of a hand lens. Dunham's classification (Dunham, 1962) considers particles less than 20 microns to be carbonate mud. Many grains in microfacies were determined to be very close that the threshold and if visual identification of their origin was possible they were considered as grains. Therefore, some lithofacies that were originally determined to be similar were in slightly different and hence, had different pore systems. However, some lithofacies were determined to be similar both microscopically and macroscopically.

Similar lithofacies did show some correlation of pore size distributions but many factors contributed to their differences such as degree of dolomitization and anhydrite emplacement within the sampled interval. Pore size distribution of all samples of facies G, all determined to be a crystalline anhydritic dolostone, show a consistent unimodal or bell shaped distribution of pores (Figure 48).

Pore Size Distribution with Relation to Depositional Facies

No direct correlation between depositional facies and pore size distributions were found in this study. However, some broad observations were made by examining the pore distributions. Two supratidal facies, A1-6042 and B2-6048 (Figure 47), show a common distribution shape. Common distribution shape is thought to be a reflection of fine laminations in both samples which have vuggy pores near them. Sample B1-6046 is more quartz-rich, lacks laminations, has more moldic pores and fewer solution enlarged vugs.

Four out of five subtidal facies show a consistent bell shaped distribution of pore sizes (Figure 48). Bell-shaped distribution is probably the product of recrystallization and cementation of muddy, homogenous deposits, producing similar pores types and geometries. All three intertidal-subtidal facies show a dominance of pore sizes $3.2 \mu\text{m}$ and $10 \mu\text{m}$. These pores are interpreted to be intercrystal pores found in the matrix.

Intertidal facies did not show any noticeable correlation and pore size distributions varied from sample to sample.

Pore Shape Parameter

Pore shape parameter ($\bar{\gamma}$) was calculated using equation 7 and from SEM measurements for all 21 samples in this study. Micropore ($<500 \mu\text{m}^2$) and macropore ($>500 \mu\text{m}^2$) shape parameters were calculated separately as well as cumulatively to give an overall shape parameter for all pores. Values ranged from as low as 1.6, to as high as 3.8. Lower shape parameter samples generally related to the presence of moldic pores (Figure 57). Samples displaying larger $\bar{\gamma}$ parameters were attributed to pores that were of vuggy and intercrystal nature (Figure 58).

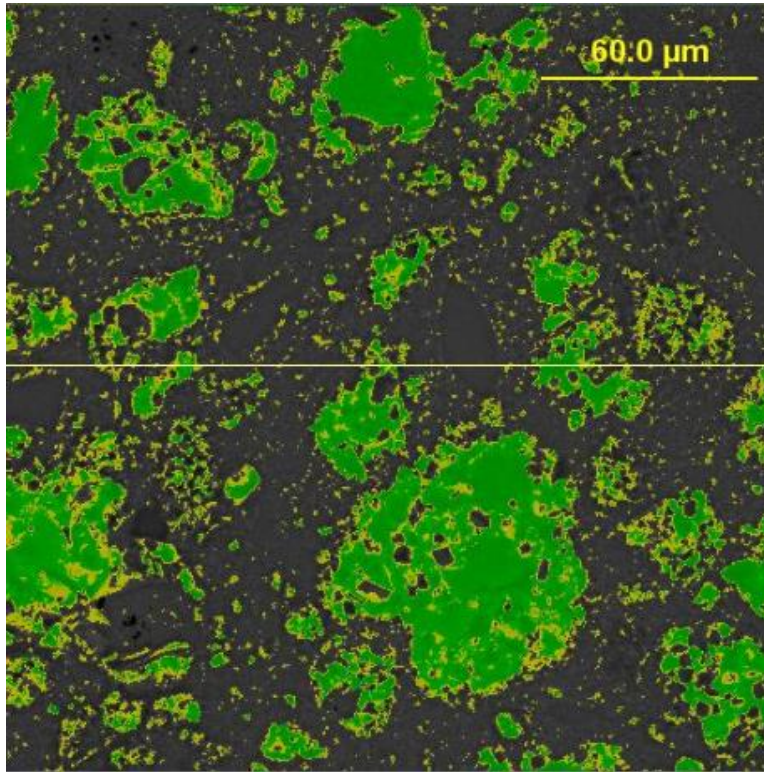


Figure 57: SEM photo of round pores with low $\bar{\gamma}$ values. Sample B1-6046 at high magnification (750x) displaying moldic pores (green). This sample has a $\bar{\gamma}$ value of 2.0 for both micropores and macropores.

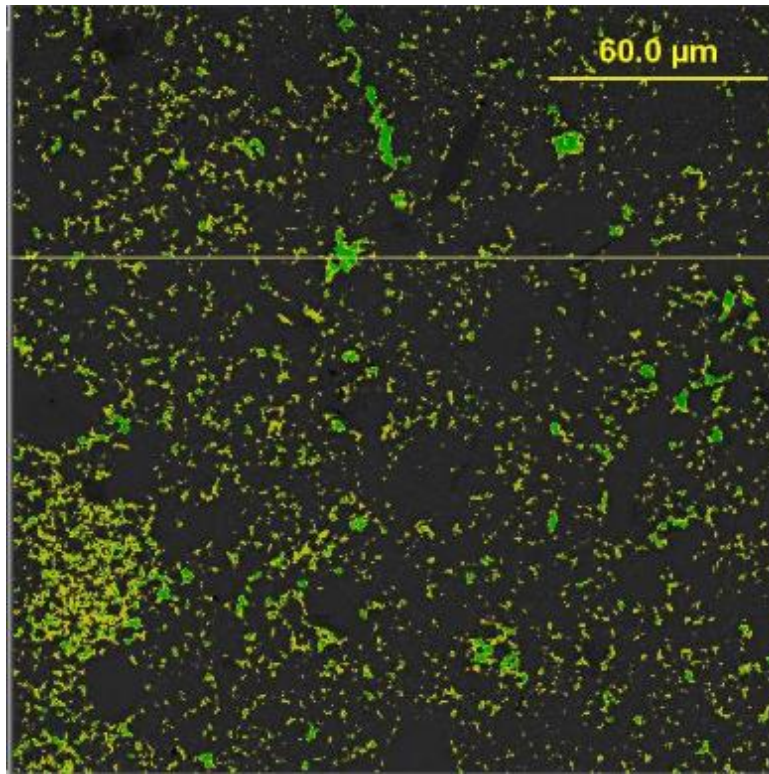


Figure 58: SEM photo of intercrystalline pores which have higher $\bar{\gamma}$ values. Sample A1-6042 at high magnification (750x). This sample has a $\bar{\gamma}$ value of 3.9 for micropores and 2.0 for macropores (not in field of view).

Pore Shape Relation to Permeability

Initially, it was hypothesized that samples with higher permeability should have higher shape parameter ($\bar{\gamma}$) values because in theory higher shape parameter values should indicate more elongate pores (equations 6 and 7). Therefore, elongate pores should be an indication of pore connectivity when examined in two dimensions. However, crossplots in Figures 51, 52, and 53 show little to no correlation between permeability and shape parameter. Figure 46 includes individual shape parameters and permeability measurements and further suggests that there is no correlation between the two

measurements. It is particularly evident in samples C1-6052 and C2-6053, which have the highest permeability values, yet show a relatively lower \bar{y} value for both micropores and macropores.

The lack of correlation between permeability and shape parameter can be attributed to several factors. Like porosity, permeability values were determined from foot intervals of core around each sample and therefore a scale bias is introduced when attempting to link the two values. Also similar to porosity quantification, the small size of thin sections does not give full representation of pore shapes due to significant heterogeneity. Laminations, degree of cementation, and varying pore structures throughout the sample can influence shape parameter values of the whole sample.

A significant limitation to equation 7 is that it does not account for rugosity within each pore. Many samples contain pores that have been altered by cementation. Dolomite cementation in particular, adds a higher perimeter surface to the pores. The additional perimeter from the dolomite cement rhombs is not balanced by larger areas in the pore structure. Therefore equation 7 calculates highly elongate pores from more or less circular pores because of their high perimeter to low area ratio. Dolomite cementation and its addition to perimeter value are illustrated in Figure 39.

Pore Parameters Controlling Permeability

It is generally accepted that unlike clastic reservoirs, carbonate reservoirs do not have a common permeability-porosity relationship (Ahr, 2008). The absence of a relationship in carbonate reservoirs is because intercrystal (or interparticle) pores are often not the dominant type as they are in clastic reservoirs. As documented from SEM images in this study, intercrystal porosity is common in the matrix. Though and abundance of intercrystalline pores, the presence of moldic and vuggy pores complicates the relationship between permeability and porosity. To illustrate that there is no

relationship, the SEM measured total porosity of each sample was crossplotted with the whole-core air permeability of each sample (Figure 54). From the crossplot, an r^2 coefficient was measured to be 0.0005, which proves there is no correlation between the two parameters as hypothesized.

An initial hypothesis in this study was that permeability was influenced by the amount of microporosity. Work by Anselmetti et al. (1998) states that samples with higher microporosity were correlated with higher permeability's. It was believed that intercrystalline matrix porosity provided a fluid flow path. Therefore, more microporosity should equal higher permeability. To test this hypothesis, a crossplot of microporosity versus whole-core permeability was generated (Figure 56). A low r^2 coefficient of 0.0396 was calculated. It is apparent from the low coefficient that little to no relationship exists between microporosity and permeability. The lack of a relationship is probably due to varying degrees of cementation, dissolution and recrystallization for each sample.

A crossplot of macroporosity versus permeability was generated to see if any relationship between the two exists (Figure 55). Surprisingly, the two showed a relatively strong correlation, with an r^2 coefficient of 0.5548. This correlation coefficient is remarkably higher than the two crossplots of total porosity and microporosity versus permeability. The strong correlation suggests that samples with higher amounts of macroporosity have higher permeability's. It is possible that samples with larger pores held more diagenetic fluids and were therefore prone to more dissolution. The larger moldic pores can be attributed to a grain-rich depositional texture. In a sense that makes higher permeability facies a product of fabric selective diagenesis. Intercrystalline pores appear to connect the larger moldic pores. This concept makes sense in intertidal depositional facies but not in subtidal facies which also display relatively higher permeability values. The formation of vugs from diagenetic fluids in subtidal facies,

coupled with intercrystalline porosity that may be enlarged by the fluids, is probably what gives facies their higher permeability.

Limitations and Considerations

Porosity quantification from SEM image analysis yielded varying results. Whole-core gas expansion porosity (helium) conducted by Core Laboratories was utilized as a “true” total porosity for comparison. The utilization of the two methods proved to be erroneous in many cases. Any correlations or conclusions from SEM image analysis in this study are to be considered carefully.

Several issues arose while comparing whole-core gas expansion porosity to SEM thin section image analysis porosity. A major drawback to the SEM method was the unrepresentative fields of view from thin sections, (<2 inches of core coverage) when attempting to compare to an entire foot of whole-core total porosity. The comparison of the two measurements is considered to introduce a scale bias. Whole-core porosity accounts for pore space in fractures and vugs within the entire 1 foot core interval. Much of this larger pore space is outside the resolution of a standard thin section, which may help explain why SEM analysis porosity are much lower than whole-core porosity.

On the other hand, whole-core porosity can only account for pore space that is reachable by helium gas, hence effective porosity. Most of the samples in this study have very low permeability's, many less than 0.1 millidarcies, and although helium has small molecules, gas may have not reached all pore spaces if long equilibration times were not used. In a commercial setting, with a large scale coring job consisting of almost 4000 feet of core retrieved and analyzed from 35 wells, some negligence of laboratory measurements and practices may have occurred. Short equilibration times leaves ineffective pore space unaccounted for. Using thin sections it is likely that ineffective pore space was exposed in the image analysis which may help contribute to the larger SEM

porosity values relative to the whole-core porosity. The presence of grain and skeletal moldic pores, as well as isolated vugs, further suggests a large amount of ineffective porosity seen in the image analysis but missed in the whole-core porosity.

Assuming that effective pore space is captured by data from the image analysis (Figure 46), a crossplot of SEM and Helium porosity values was generated using only samples that show permeability values greater than or equal to an arbitrary value of 0.03 millidarcies (Figure 59). By omitting the very low permeability samples, the r^2 coefficient was raised from 0.07 to 0.58. The significant increase in the r^2 value suggests that samples displaying low permeability values were not subject to long equilibration times for whole-core gas expansion analysis and therefore may be unrepresentative of true total porosity.

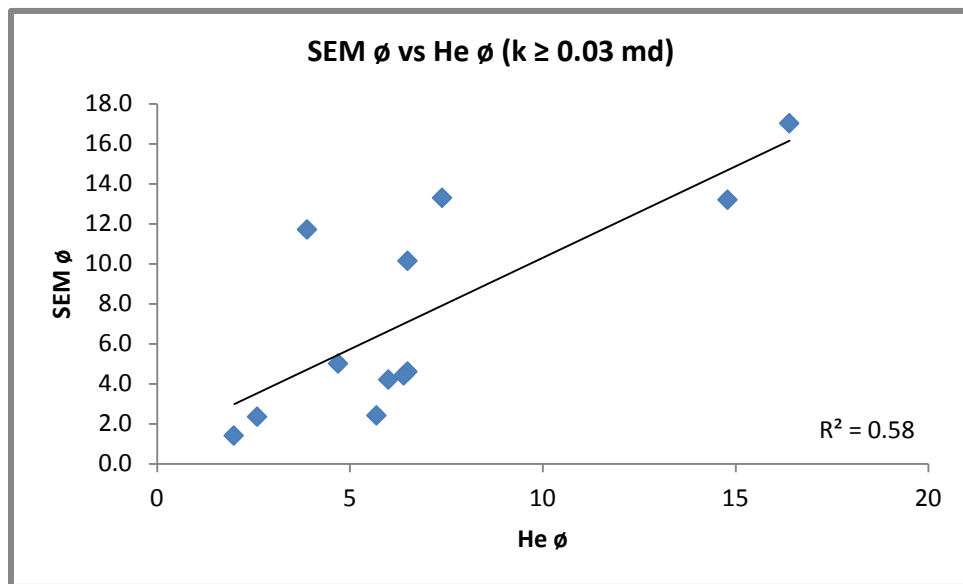


Figure 59: Crossplot of Helium porosity and SEM porosity. Samples with less than 0.03 millidarcies were omitted which dramatically increased the r^2 coefficient.

Laminations and extreme heterogeneity, both vertically and horizontally, at scales of less than 1 cm, introduces another sampling error and can be seen throughout the core and in thin sections. Heterogeneity can be attributed to significant diagenetic alteration but can also be a product of rapidly changing depositional environments. Whole-core porosity analysis in essence, gives a total porosity for all of the many lithologies combined in the measured foot. A large combination of lithologies is not the case for the thin section image analysis which represents a much smaller area. The difference between whole-core values and thin section values can be considered to be a scale bias.

Selecting the fields of view (FOV) on each thin section also introduced a possible observer error. If the user omitted certain fields of view with pores too large or none at all, it would introduce yet another sampling bias. To generate the most unbiased results, FOV's were picked randomly while also attempting to equally space them apart across the thin section. If allotted the time and resources, scans of the entire thin section, rather than 8 points, may have yielded values closer to whole-core gas expansion porosity, though a scale bias still exists.

Another possible error was the calibration of a gray threshold. Images were meticulously studied to delineate pores from the solid phase so that the thresholds could accurately represent pore space. However, user error is always a possibility when a personal judgment is used to select the threshold.

Although great variations between whole-core and SEM image analysis porosity are seen in several samples, it is assumed that the SEM image analysis is representative of the specific area where the thin section was obtained from. Additionally, image analysis has been a proven and reliable method of pore quantification in several previous studies (Ehlich et al., 1984, 1991a, 1991b; McCreesh et al., 1991; Gerard et al., 1992;

Anselmetti et al., 1998). Where lithology is more homogenous for the entire foot of the core (Figure 60), such as in samples E2-6073, L2-6127, L3-6134 SEM, whole-core analysis and SEM image analysis show very similar values of total porosity. Therefore pore size distributions are still assumed to be representative of the thin section samples.



Figure 60: Core photograph of homogenous lithology. Sample E2-6073 which contains very similar SEM and whole-core helium porosity values.

For the purpose of reservoir exploitation, SEM porosity quantification for the Clear Fork reservoir was an ineffective method in this study. The highly heterogeneous nature of carbonate reservoirs makes the quantification of their porosity a challenge. Because SEM image analysis measures such a small area of the reservoir, it does not represent the large volume. In clastic or homogenous carbonate reservoirs however, where pore types are more uniform and evenly distributed, SEM image analysis could prove to be a very effective method for quantifying porosity. In future work the scale bias

could be significantly reduced if thin sections were made from the ends of core plugs which are then subject to Mercury Injection Porosimetry (MIP) or some other plug measurement of porosity, which would be more suitable for comparison and calibration between the two measurements.

Although SEM porosity analysis is an ineffective tool for the quantification of porosity in heterogeneous reservoirs, it proved to be critically important for qualitatively studying the pore system. The resolution provided by the backscattered electrons highlighted features of the pore system otherwise not seen in optical microscopy. By studying the images from the SEM analysis, a greater understanding of the pore system was attained.

Chapter 6

Reservoir Exploitation

The main purpose and ultimate goal of this study, is to gain a better understanding of the reservoirs in the upper Clear Fork of *FCU 1947*. By using the observations from whole-core, thin section microscopy, and SEM image analysis, delineation of poor and good reservoirs can be made. By implementing wireline logs, poor and good reservoirs can be correlated to nearby wells at similar structural position by their broadly unique signatures which may bring added value to this study. However, the complexity of carbonate facies, and significant stratigraphic changes, makes it nearly impossible to correlate reservoirs across the entire field.

Wireline Log Responses

Results

Plate 1 and Figure 61 show the wireline log responses of the cored interval. The slabbed core was originally marked with depths before it was depth shifted to the correct MD. To depth shift the interval, the most radioactive shale determined from the gamma ray log to be at 6121', was tied to the same physical deposit in the slabbed core, found at 6123'. By doing this, the cored interval was determined to be 2 feet shallower than originally marked, and was shifted accordingly. The original interval of 6015'-6145' was shifted to 6013'-6143'. Both shifted and original depths are labeled in Plate 1. Wireline log depths of the cored interval are the shifted depths of between 6013'-6143'. It is important to note that all mentions of depth in core analysis and in sample labels found in previous chapters are the original unshifted depths, as marked on the slabbed core.

From examining core and wireline log responses, it was determined that no direct correlation between lithofacies and wireline signatures could be made. However, by studying the core, dominant depositional environments, and resultant depositional facies

were determined for each sub-interval. These sub-intervals displayed somewhat unique wireline responses which were correlated to nearby wells. By correlating these sub-intervals from FCU 1947 to nearby wells, it is possible to target reservoirs beyond those of the studied well. The wireline log responses of the sub-intervals and depositional facies are examined in the discussion portion of this chapter.

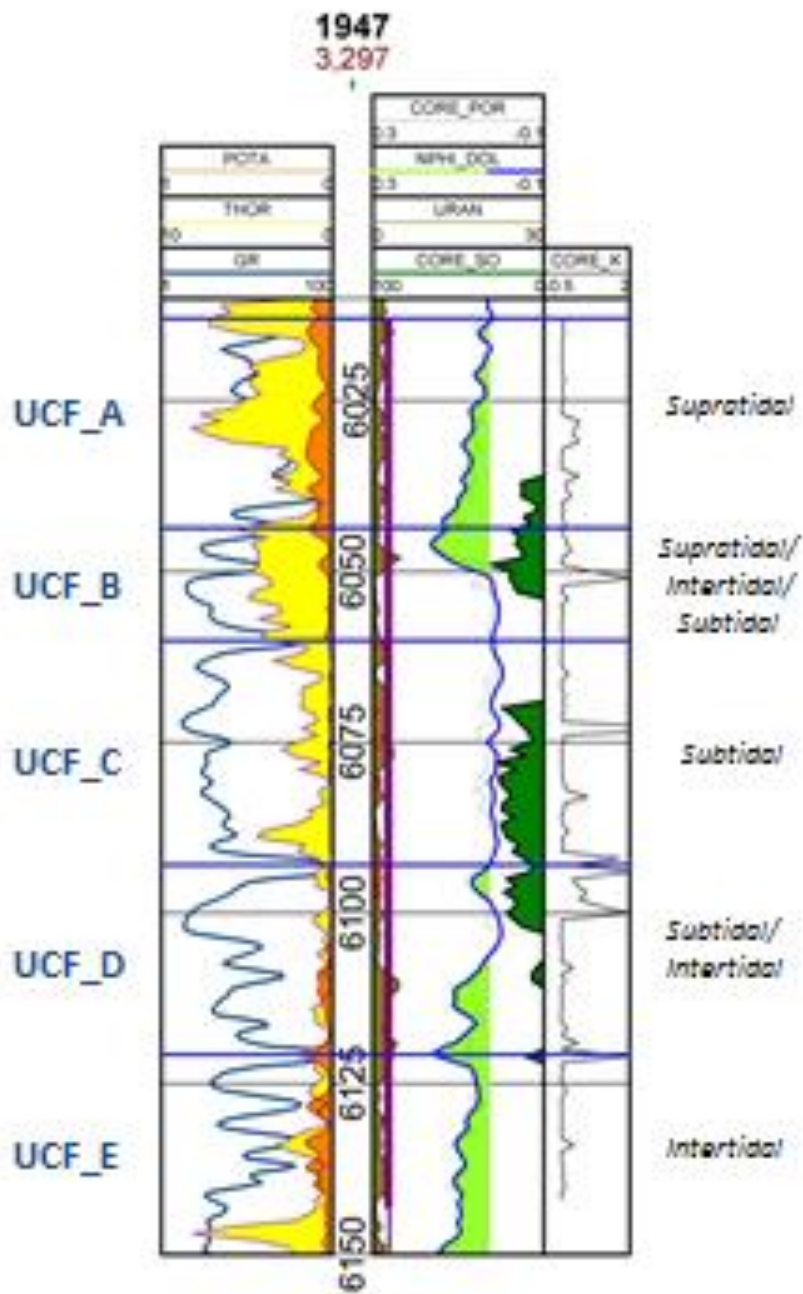


Figure 61: Wireline log responses and core analysis measurements of the FCU 1947 cored interval (XTO Energy, 2013).

Discussion

The most distinguishable depositional facies within the cored interval via wireline logs are the subtidal facies. Subtidal facies display a very 'clean' gamma ray response with a value of between 10 and 30 API units. They also display little variation in gamma ray response from foot to foot. The 'clean' gamma ray response is consistent with macroscopic and microscopic examination of facies which show a dominance of recrystallized carbonate mud which is not very radioactive. However, the presence of stylolites in the subtidal facies does indicate concentration of radioactive minerals, particularly thorium. The clean gamma ray response coupled with the spike in thorium, gives these subtidal facies a unique log response that can be correlated to nearby wells.

Neutron and density porosity measurements in these subtidal facies display very low values. The low values are consistent with whole-core and SEM porosity measurements. The neutron and density signatures are consistently low and show little variation from foot to foot. Anhydrite plugging, compaction, and burial diagenesis were all determined to contribute to the low porosity values of subtidal facies. Resistivity values (shallow, medium, and deep) of these facies are high (shown in plate 1), typically greater than 100 ohms. Though high resistivity values may appear to indicate hydrocarbons in place, it was determined to be a reflection of the low porosity and permeability of these facies, making the rock more resistive to electrical current. Subtidal facies are deposited at: the top of the UCF_D sub-interval, the entire UCF_C sub-interval, and at the base of the UCF_B sub-interval.

Intertidal facies display a 'hotter' gamma ray response than subtidal facies but 'cleaner' response than supratidal facies. Furthermore, the gamma ray signature is not as consistent as subtidal facies and cycles between 'hot' and 'clean'. The cycling is a product of small scale sea level fluctuations, in which intertidal and supratidal

environments are most affected. Gamma ray measurements of intertidal facies cycle from 30 to 80 API units. These facies also show higher concentrations of potassium, thorium and uranium than subtidal facies.

Neutron and density responses show fairly consistent values that don't change abruptly in intertidal facies. The facies display porosity values between 5 and 10 percent. Resistivity measurements (shallow, medium, and deep) range between 5 and 30 ohms in intertidal facies and are also fairly consistent. Almost all of sub-interval UCF_E, the bottom half of UCF_D, and the middle to top half of UCF_B have intertidal deposits.

Supratidal facies in the core display the 'hottest' gamma ray responses, with the exception of shale. Thorium in particular, increases greatly in supratidal facies. It is apparent in Plate 1 and Figure 62 that thorium increases towards the top of the interval. API values in supratidal facies range from 40 to 100 units and overlap somewhat with intertidal facies but the greater thorium content in supratidal facies makes it possible to delineate the two.

Neutron and density responses show more abrupt changes from foot to foot in comparison to intertidal and subtidal facies. Anhydrite and silty beds explain variations of porosity values. Wireline porosity values in supratidal facies vary from 3 to 15 percent. Porosity is highest at the base of supratidal cycles and decreases up section. Resistivity measurements (shallow, medium, and deep) show variation of values from 3-70 ohms in supratidal facies. Much of the variation in resistivity measurements is assumed to be directly related to variations in porosity.

Perforation Targets and Completions Practices

Results

It was concluded in this study that individual lithofacies within the upper Clear Fork cored interval are volumetrically insignificant due to the thinly bedded nature of their

deposits. The dominance of mud throughout most of the core made skeletal and grain content of facies negligible in relation to the pore system. SEM porosity analysis and microscopic examination of similar lithofacies showed little correlation in respect to their pore systems. Diagenetic overprint, both fabric selective and not, is believed to have altered the pore systems in many similar lithofacies.

Although individual lithofacies were determined to be insignificant in reservoir exploitation; depositional facies were found to be useful for the process. By examining core, thin sections, SEM analysis, and wireline responses, three depositional facies were identified and examined. Subtidal, intertidal, and supratidal facies can be delineated from one another and their specific characteristics can be applied to reservoir exploitation. As mentioned throughout this study, the characterization and correlation of sub-intervals makes it possible to target similar reservoirs in nearby wells.

Discussion

The poorest reservoir facies were determined to be subtidal facies. The restricted lagoonal depositional realms where they were deposited favored the deposition of mud. Protection from near surface dolomitization allowed thick sequences of pelleted mud to accumulate in the lagoons. Later, compaction and heavy anhydrite precipitation destroyed most porosity and permeability. Their lithofacies consist of planar subhedral/euhedral dolomite which is recrystallized mud (from burial diagenesis). Because there is a dominance of subhedral crystals, the facies do not have much intercrystalline porosity, and little connectivity. Secondary pore space in the subtidal facies has been mostly plugged by anhydrite. Remnant grains have been heavily dolomitized and show large dolomite crystals, and sometimes poikilotopic anhydrite (replacement and pore filling). Fluid saturations from core analysis (Plate 1 and Figure 61) indicate that UCF_C has the highest volume of oil, but because of the small pore

sizes and low permeability, it is believed to be residual oil bound by capillary forces. It is therefore concluded that subtidal facies in FCU 1947 and nearby wells, do not make good reservoirs. Sub-interval UCF_C should be avoided when recompleting the FCU 1947 and surrounding wells. If it is decided that the sub-interval will be recompleted, there is little use in acidizing the target, as it is almost entirely dolomite and anhydrite.

Intertidal facies were determined to be the best reservoirs in restricted interior platform type environments, such as the ones proposed in this study. Because intertidal facies were not exposed to sitting bodies of water like supratidal (tidal-flat) facies, they were not as heavily cemented by hypersaline refluxing and eogenetic alteration (dolomitization, dolomite cementation, and sulfate cementation). The intertidal facies show the most calcite which further suggests they are not as diagenetically altered. The facies have the largest grain size, the least mud, and the least anhydrite. The intertidal sub-intervals and facies of the 1947 core and nearby wells contain the best reservoir deposits and would be the best perforating targets (Figures 62 and 63). Although sub-interval UCF_E is almost entirely intertidal facies, it was determined from fluid saturation analysis to be over 90 percent water. However, correlating the sub-interval to up-dip wells and examining water saturations could result in an oil wet zone above a water contact, with favored reservoir properties. The intertidal facies of UCF_B were determined to have some oil bearing deposits, and would make the best producing interval of the cored interval.

Supratidal facies are the second best reservoirs. These facies are slightly more grain-rich than sub-tidal facies but less than intertidal. Grains are smaller in these facies compared to intertidal facies because larger grains fell out of suspension before reaching the tidal-flat environment. Grains are likely storm or spring deposits. The supratidal facies were dolomitized early from refluxing brines which also overdolomitized them, reducing

secondary porosity. However, the early dolomitization helped protect these facies from excess compaction during burial. The facies show more anhydrite than intertidal facies but slightly less anhydrite than subtidal facies but supratidal facies are the only depositional facies with bedded anhydrite. Supratidal facies also show a significant amount of leaching and resultant moldic porosity. Dissolution probably occurred in these facies because tidal-flat environments were exposed to occasional rain water, which partially dissolved grains (mainly aragonite). The somewhat grainy, moderately anhydritic, and partially dissolved nature of these facies is what makes them the second best reservoirs.

The supratidal and intertidal facies from 6040' to 6052' (shifted, wireline depth) make the best perforation targets of the cored interval. These facies display high porosity, good permeability, and relatively good oil saturation. The pore systems in these facies are characterized as vuggy and moldic from dissolution during sea level low-stands. These facies also have large macropores which are likely connected by intercrystalline matrix pores. Furthermore, the presence of calcite in these facies suggests they should be acidized before stimulation (hydraulic fracturing). In conclusion, it is determined that the intertidal and supratidal deposits at the top of shallowing upwards cycles are the best perforation targets in *FCU 1947* and nearby wells (Figures 62 and 63).

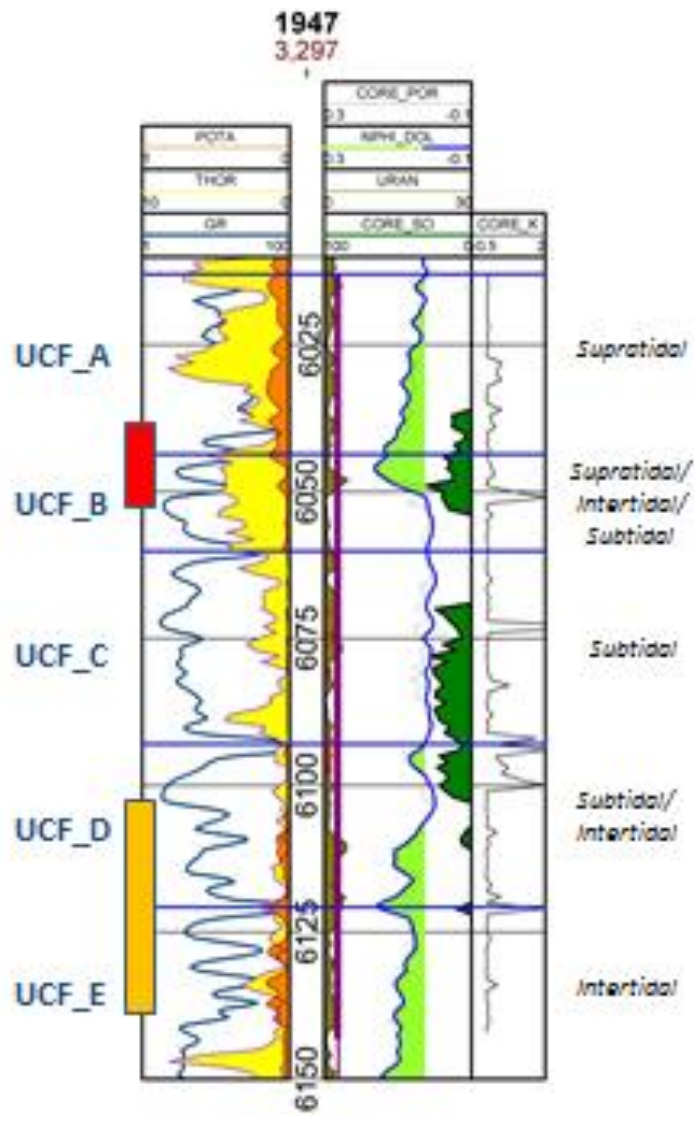


Figure 62: Proposed perforation intervals for FCU 1947. Red rectangle outlines suggested perforation interval directly below a shallowing upwards cycle top. Secondary perforation interval is the orange rectangle (XTO Energy, 2013).

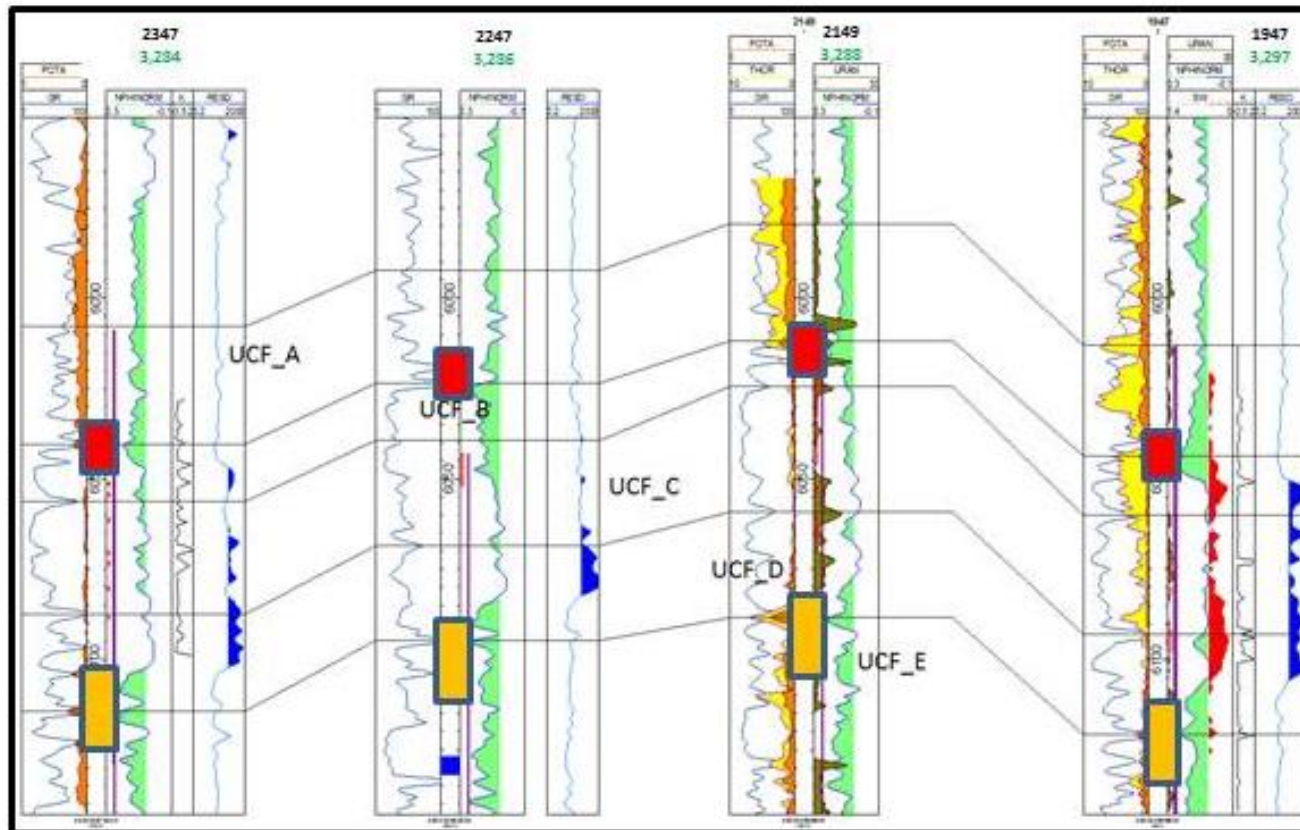


Figure 63: Suggested perforation intervals in structural cross section of FCU 1947 and nearby wells (XTO Energy, 2013).

Chapter 7

Conclusions

1. Fullerton Field upper Clear Fork deposition took place in a very shallow water carbonate environment on the interior of the Central Basin Platform. Low depositional topography created an environment where small scale changes in sea level caused highly cyclic deposition.
2. Interpreted depositional environments within the study were determined from core and thin section analysis to be low-energy subtidal, intertidal and supratidal realms. Minor, high-energy open marine facies were only identified in two intervals which had grainstone deposits.
3. Lithofacies categorized macroscopically and microscopically using Dunham's (1962) classification scheme showed some discrepancies between the two due to the extremely fine-grained and muddy nature of the deposits. Furthermore, lithofacies were determined to be extremely heterogeneous, vertically and laterally, sometimes at scales of less than 1 cm.
4. Dolomitization, overdolomitization, evaporite precipitation, and dissolution in the eogenetic stage are responsible for diagenetic overprint in intertidal and supratidal facies. Subtidal facies however, were protected from hypersaline refluxing but were subjected to compaction and burial diagenesis in the mesogenetic realm.
5. Heavy diagenetic overprint in deposits altered pore systems at multiple events, creating an almost exclusively secondary pore system.
6. Characterization of pore system in specific lithofacies was determined to be of only minor importance. The varying degrees of diagenetic alteration often produced dissimilar pore systems in similar lithofacies. Rather, characterizing

overall pore systems for overall depositional environments in correlatable sub-intervals brings more volumetric significance.

7. Moldic, vuggy, and intercrystalline (matrix) pore types were determined to be the most abundant pore type. Less abundant types identified were fenestral, fracture, boring, intracrystalline and shrinkage pores.
8. SEM analysis was determined to be an ineffective method of quantifying porosity in highly heterogeneous carbonate reservoirs. The small coverage of reservoir rock in a thin section made the quantification of porosity via SEM image analysis a volumetrically insignificant method which is only representative of the small area a thin section encompasses.
9. Comparing SEM image analysis porosity values to whole-core gas expansion (Helium) values introduced a scale bias. The bias made the comparison of the two measurements highly variable. The same scale bias can be said for comparing attributes (pore shape, microporosity, macroporosity, total porosity) to air permeability values also determined from whole-core. Any correlations between SEM derived values and whole-core derived values should be considered cautiously.
10. Crossplots of SEM porosity and gas expansion porosity using only samples with permeability's greater than or equal to 0.03 md suggest that low permeability rocks, such as those found in the upper Clear Fork require long equilibration times when using the gas expansion method. If long equilibration times are not provided, only effective pore space will be accounted for. Higher permeability samples showed significantly closer values between SEM and whole-core analysis.

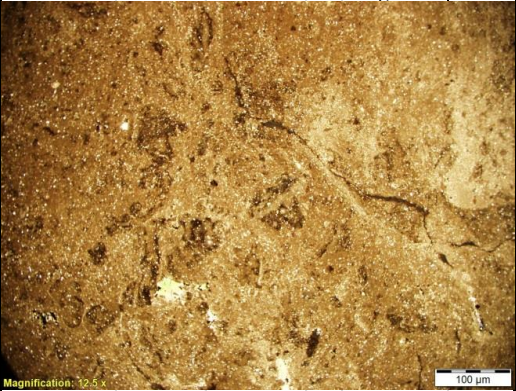
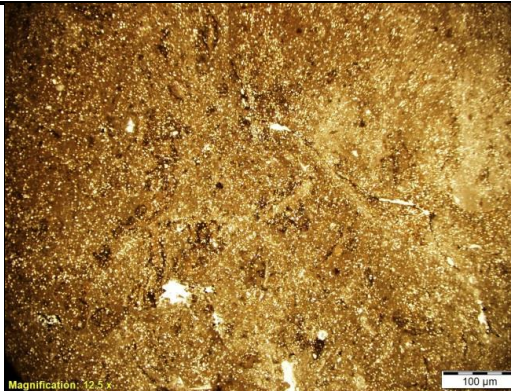
11. No correlation between micro, macro or overall pore shape (\bar{y}) with permeability was identified. This finding postulates that pore geometry within measured samples does not have an effect on connectivity of pore networks.
12. No correlation between microporosity and permeability was identified by crossplotting the two measurements. The lack of correlation suggests that fluid pathways may not follow micropore networks as originally hypothesized.
13. A relatively strong correlation between macroporosity and permeability was found. Higher macroporosity yielded higher permeability in most samples. Higher macroporosity and permeability is interpreted to be a product of fabric selective diagenesis, in which intertidal and supratidal facies were leached of their grains during sea level low-stands and resultant dissolution processes. Therefore, diagenetic fluids preferentially passed through intertidal facies, increasing their overall pore systems.
14. Subtidal facies are the most distinguishable of the depositional facies via wireline logs. They are characterized by a 'clean' gamma ray response (between 10 and 30 API units). Furthermore, the presence of stylolites within these facies can be correlated to high amounts of Thorium which can be identified on spectral gamma ray logs. Neutron and density signatures through these facies are subtle and have consistently lower porosity values in comparison to the other depositional facies.
15. Supratidal and intertidal facies show some overlap in their gamma ray signatures but supratidal facies display slightly 'hotter' gamma ray readings. Supratidal facies also display highest concentrations of Thorium in comparison to the other depositional facies. Neutron and density porosity logs in supratidal


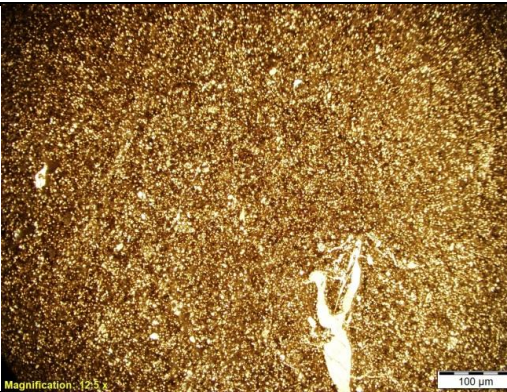
facies show sporadic trends which are believed to be a product of anhydrite beds and silt or clay-rich beds.

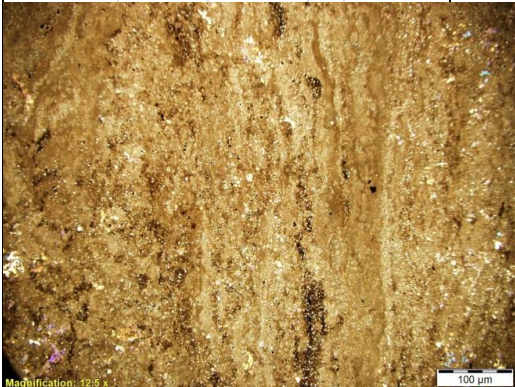
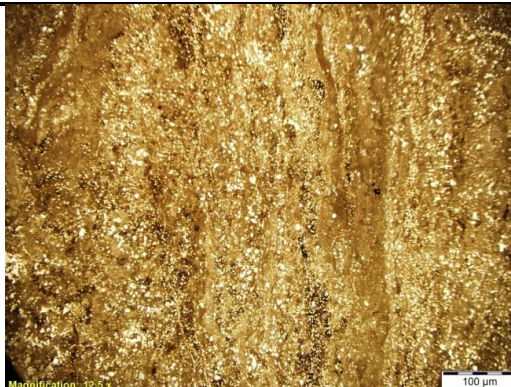
16. Intertidal facies have cyclic gamma ray signatures, a product of small scale sea level changes. Gamma ray values range between 30 and 80 API units. Neutron and density porosity wireline signatures show a consistent and subtle porosity trend with values ranging between 5 and 10 percent.
17. Subtidal facies were determined to be the poorest reservoirs. Pore systems in these facies were more or less obliterated from compaction, anhydrite plugging, burial diagenesis, and chemical dissolution in the mesogenetic stage. If these facies are to be selected for a perforation interval, it would be economical to not acidize the zone. Acid jobs would have little effect on these facies as they are an almost entirely dolomite and anhydrite mineralogy.
18. Intertidal facies were determined to be the best reservoirs. Protection from excess anhydrite precipitation by tides, helped preserve pore space. Protection from tides also meant these facies were not as subjected to hypersaline refluxing (compared to supratidal facies) and therefore were not as overdolomitized. These facies are also the most grain-rich and contain the most calcite. Acidizing these facies could be economical and improve well performance. Furthermore, intertidal facies directly below supratidal cycle tops were found to be better reservoirs than intertidal facies below subtidal facies (transgressive sequence).
19. Supratidal facies were found to be the second best reservoirs. Hypersaline refluxing in the eogenetic realm plugged pore space in these facies but the dolomitization of these facies helped create deposits which were more resistant



to compaction and burial diagenesis. Supratidal facies still have some preserved calcite but not as much as intertidal facies.

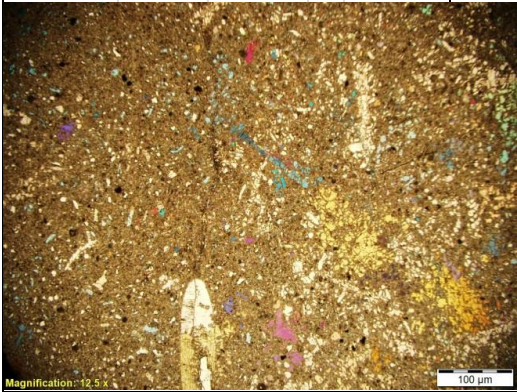
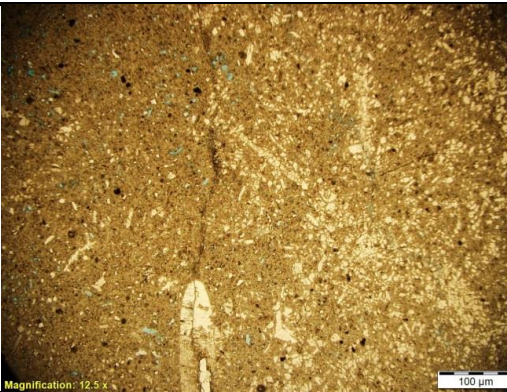
Appendix A
Thin Section Data


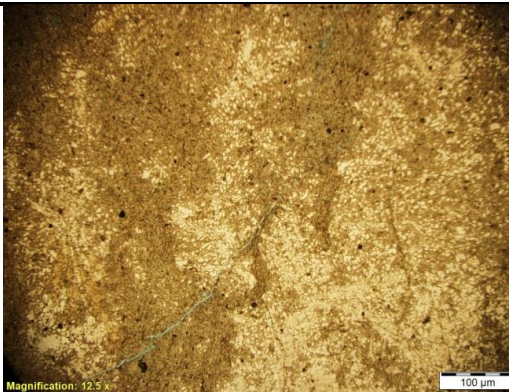
THIN SECTION #: A1-6042		LOCATION: Well # FCU 1947		Formation: upper Clear Fork	
DUNHAM CLASSIFICATION:		Skeletal laminated Ws/Ps			
GRAIN COMPOSITION			%	DESCRIPTION	
ALLO CHEMS:	Bioclasts:	Forams -	2	Moderately preserved very small (<0.5mm) uniserial forams.	
		Bivalves -	5	All other bioclasts skeletal (fragments)	
		Ostracods -	2		
		Gastropods -			
		Other -		Skeletal bryozoans	
	Undiff -				
	Intraclasts:	Mud -	5	Mudflakes (rip-up clasts) and mudcracks	
		Peloids -	10	Micritized peloids	
		Ooids -			
		Other -		Most mud recrystallized to cryptocrystalline dolomite	
MINERAL COMPOSITION (=100%)		Calcite -	30		
		Dolomite -	35		
		Sulfate -	15		
		Quartz -	15	Very fine grained quartz	
		Organics -	5		
					
12.5x CPL			12.5x PPL		

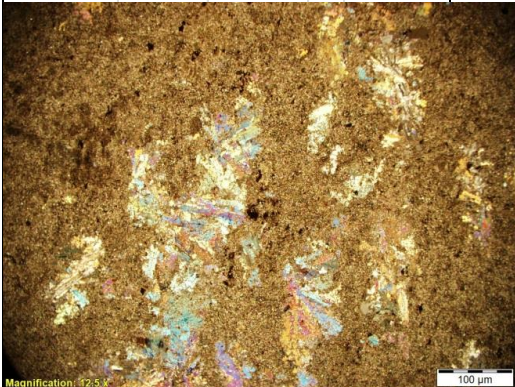
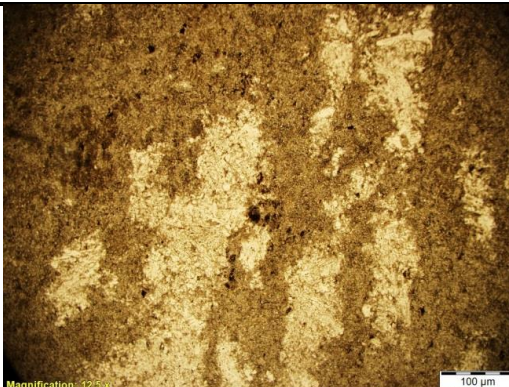
THIN SECTION #: B1-6046		LOCATION: Well # FCU 1947		Formation: upper Clear Fork	
DUNHAM CLASSIFICATION: Quartz rich Ws/Ps					
GRAIN COMPOSITION			%	DESCRIPTION	
ALLO CHEMS:	Bioclasts:	Forams -	5	Small uniserial forams	
		Bivalves -	10	Skeletal and angular	
		Ostracods -	2	Thin shelled ostracods	
		Gastropods -			
		Other -			
	Undiff -				
	Intraclasts:	Mud -			
		Peloids -	10	Peloids destroyed from transport and diagenesis	
		Ooids -			
		Other -			
MINERAL COMPOSITION (=100%)		Calcite -	30	Trace amounts of spar along some pore walls	
		Dolomite -	25		
		Sulfate -	15		
		Quartz -	25	Very fine grained quartz	
		Organics -	5		
					
12.5x CPL				12.5x PPL	


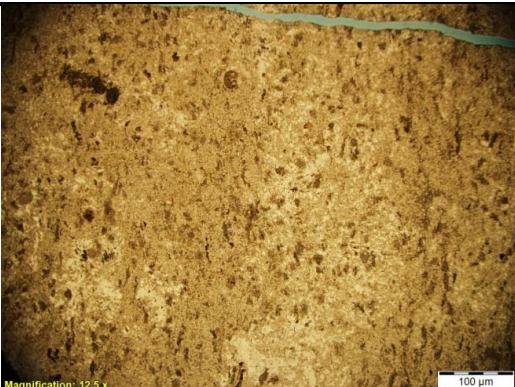
THIN SECTION #: B2-6048		LOCATION: Well # FCU 1947		Formation: upper Clear Fork	
DUNHAM CLASSIFICATION: Fenestral laminated Ws					
GRAIN COMPOSITION			%	DESCRIPTION	
ALLO CHEMS:	Bioclasts:	Forams -			
		Bivalves -	10	Bivalve fragments	
		Ostracods -	3	Few thin shelled ostracod fragments	
		Gastropods -			
		Other -	2	Small echinoid spines	
	Undiff -				
	Intraclasts:	Mud -			
		Peloids -	10	Heavily altered remnant peloids	
		Ooids -	5	Remnant ooids	
		Other -		Fenestral laminations	
MINERAL COMPOSITION (=100%)		Calcite -	35		
		Dolomite -	35		
		Sulfate -	15		
		Quartz -	10	Very fine grained quartz	
		Organics -	5		
					
12.5x CPL			12.5x PPL		

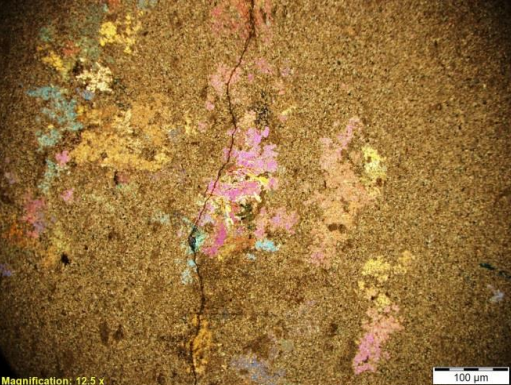
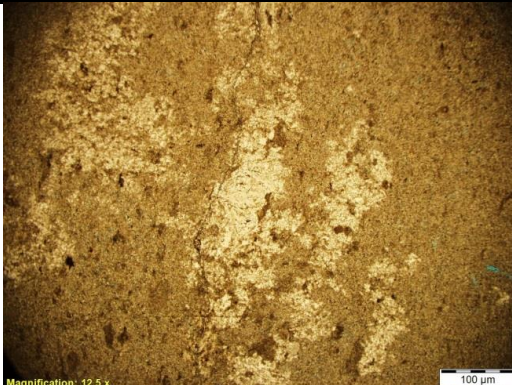
THIN SECTION #: C1-6052		LOCATION: Well # FCU 1947		Formation: upper Clear Fork	
DUNHAM CLASSIFICATION:		Crystalline anhydritic dolomite (Ms/Ws)			
GRAIN COMPOSITION			%	DESCRIPTION	
ALLO CHEMS:	Bioclasts:	Forams -			
		Bivalves -			
		Ostracods -			
		Gastropods -			
		Other -			
	Undiff -				
	Intraclasts:	Mud -			
		Peloids -			Ghost grains of micritized peloids that were recrystallized and precipitated with anhydrite/dolomite
		Ooids -			
		Other -			
MINERAL COMPOSITION (=100%)		Calcite -			
		Dolomite -	65		Dominantly dolomite matrix
		Sulfate -	30		Pore filling and poikilotopic
		Quartz -			
		Organics -	5		
					
12.5x CPL				12.5x PPL	

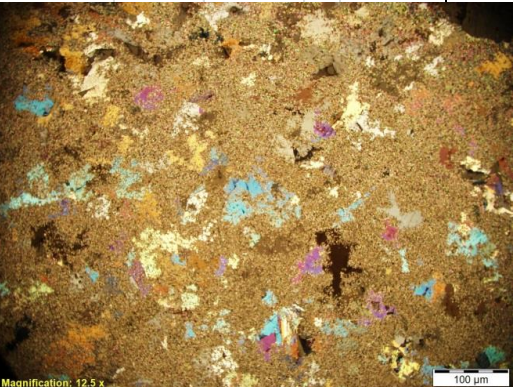
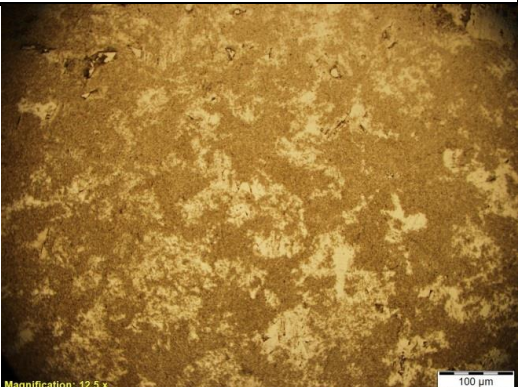
THIN SECTION #: C2-6053		LOCATION: Well # FCU 1947		Formation: upper Clear Fork	
DUNHAM CLASSIFICATION:		Crystalline anhydritic dolomite (Ms/Ws)			
GRAIN COMPOSITION			%	DESCRIPTION	
ALLO CHEMS:	Bioclasts:	Forams -		Rare bivalve fragments	
		Bivalves -	5		
		Ostracods -			
		Gastropods -			
		Other -			
	Intraclasts:	Mud -		Very fine micritized peloids	
		Peloids -	5		
		Ooids -			
		Other -			
MINERAL COMPOSITION (=100%)		Calcite -		Finely crystalline dolomite matrix Bladed, poikilotopic and pore filling anhydrite	
	Dolomite -	50			
	Sulfate -	45			
	Quartz -				
	Organics -	5			
					
12.5x CPL			12.5x PPL		

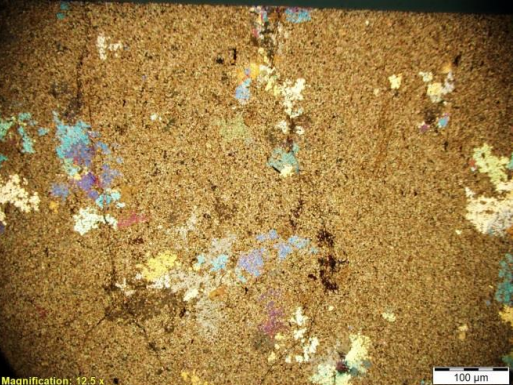

THIN SECTION #: C3-6053		LOCATION: Well # FCU 1947		Formation: upper Clear Fork	
DUNHAM CLASSIFICATION: Crystalline anhydritic dolomite (Ms/Ws)					
GRAIN COMPOSITION			%	DESCRIPTION	
ALLO CHEMS:	Bioclasts:	Forams -			
		Bivalves -			
		Ostracods -			
		Gastropods -			
		Other -			
		Undiff -			
	Intraclasts:	Mud -			
	Peloids -	10	Micritized and recrystallized peloids		
	Ooids -				
	Other -				
MINERAL COMPOSITION (=100%)		Calcite -			
		Dolomite -	45	Finely crystalline dolomite matrix	
		Sulfate -	50	Bladed, poikilotopic and pore filling anhydrite	
		Quartz -			
		Organics -	5		
					
12.5x CPL			12.5x PPL		

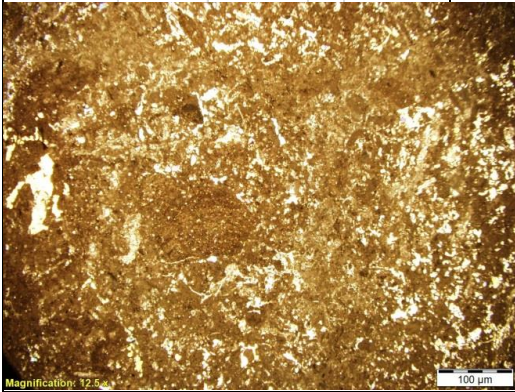
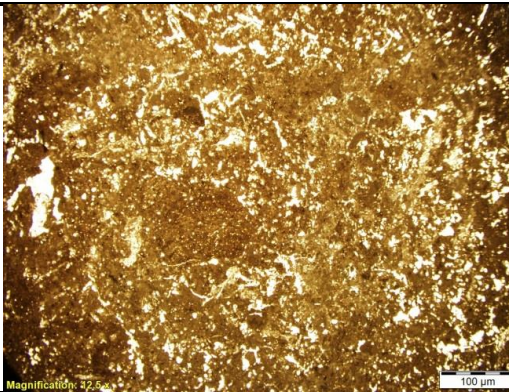
THIN SECTION #: E1-6069		LOCATION: Well # FCU 1947		Formation: upper Clear Fork	
DUNHAM CLASSIFICATION: Crystalline Anhydritic Dolomite (Ms)					
GRAIN COMPOSITION			%	DESCRIPTION	
ALLO CHEMS:	Bioclasts:	Forams -			
		Bivalves -			
		Ostracods -			
		Gastropods -			
		Other -			
	Undiff -				
	Intraclasts:	Mud -			
		Peloids -	8		Micritized prior to deposition
		Ooids -			
		Other -			
MINERAL COMPOSITION (=100%)		Calcite -			
		Dolomite -	55		
		Sulfate -	35		Poikilotopic, nodular and pore filling anhydrite
		Quartz -			
		Organics -	10		
					
12.5x CPL			12.5x PPL		

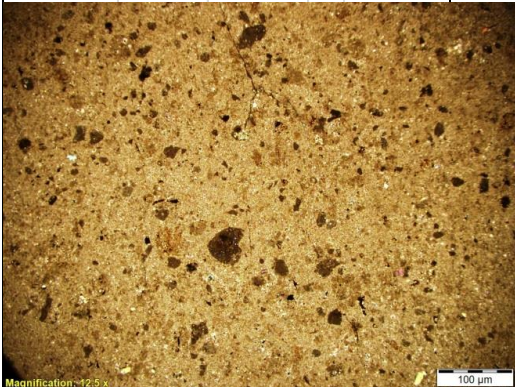
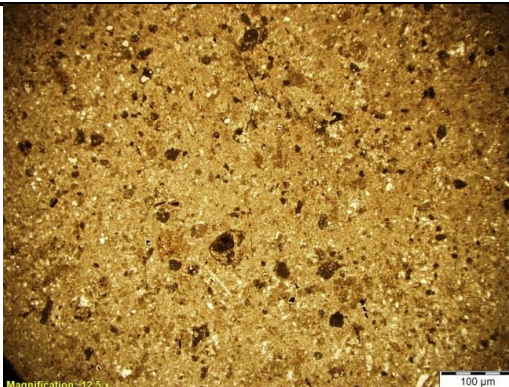
THIN SECTION #: E2-6073		LOCATION: Well # FCU 1947		Formation: upper Clear Fork	
DUNHAM CLASSIFICATION: Crystalline Anhydritic Dolomite (Ws)					
GRAIN COMPOSITION			%	DESCRIPTION	
ALLO CHEMS:	Bioclasts:	Forams -			
		Bivalves -	2		
		Ostracods -			
		Gastropods -			
		Other -	8	A few well preserved conodont elements	
	Undiff -				
	Intraclasts:	Mud -			
		Peloids -	20	Micritized prior to deposition and heavily altered after burial	
		Ooids -	5	Micritized prior to deposition	
		Other -			
MINERAL COMPOSITION (=100%)		Calcite -	5		
		Dolomite -	45		
		Sulfate -	45	Pore filling and poikilotopic	
		Quartz -			
		Organics -	5		
					
12.5x CPL			12.5x PPL		

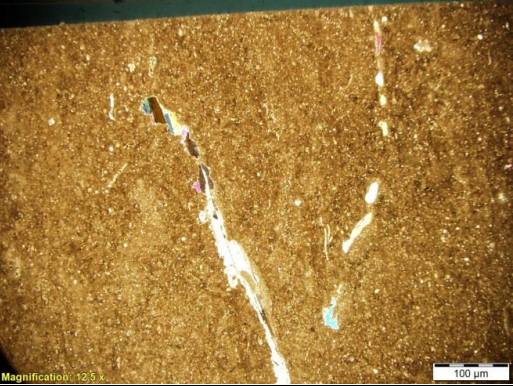
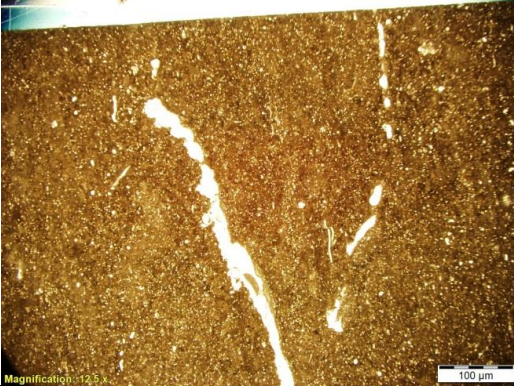
THIN SECTION #: G1-6084		LOCATION: Well # FCU 1947		Formation: upper Clear Fork	
DUNHAM CLASSIFICATION: Crystalline Anhydritic Dolomite (Ms)					
GRAIN COMPOSITION			%	DESCRIPTION	
ALLO CHEMS:	Bioclasts:	Forams -			
		Bivalves -			
		Ostracods -			
		Gastropods -			
		Other -			
	Undiff -				
	Intraclasts:	Mud -			
		Peloids -	5		Not well preserved
		Ooids -			
		Other -			
MINERAL COMPOSITION (=100%)		Calcite -			
		Dolomite -	65		
		Sulfate -	30		Pore filling anhydrite
		Quartz -			
		Organics -	5		
					
12.5x CPL			12.5x PPL		

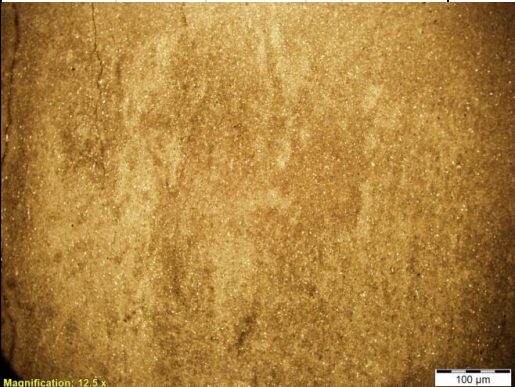

THIN SECTION #: G2-6090		LOCATION: Well # FCU 1947		Formation: upper Clear Fork		
DUNHAM CLASSIFICATION: Crystalline Anhydritic Dolomite (Ms)						
GRAIN COMPOSITION			%	DESCRIPTION		
ALLO CHEMS:	Bioclasts:	Forams -				
		Bivalves -				
		Ostracods -				
		Gastropods -				
		Other -				
	Intraclasts:	Undiff -				
		Mud -				
		Peloids -				
		Ooids -				
		Other -				
MINERAL COMPOSITION (=100%)		Calcite -				
		Dolomite -	57	Pore filling and poikilotopic anhydrite		
		Sulfate -	40			
		Quartz -				
		Organics -	3			
						
12.5x CPL			12.5x PPL			

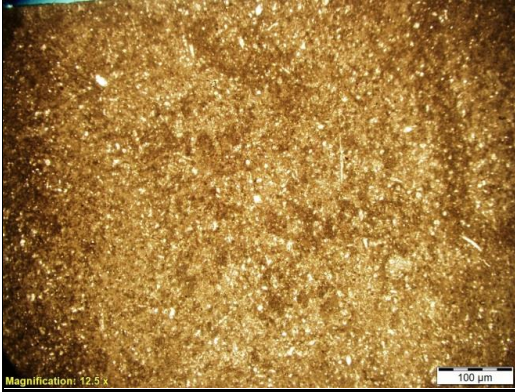
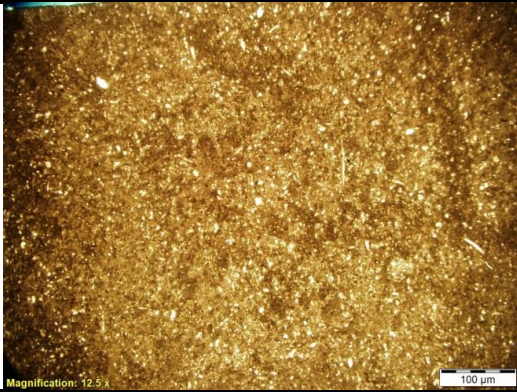
THIN SECTION #: G3-6099		LOCATION: Well # FCU 1947		Formation: upper Clear Fork	
DUNHAM CLASSIFICATION: Crystalline Anhydritic Dolomite (Ms)					
GRAIN COMPOSITION			%	DESCRIPTION	
ALLO CHEMS:	Bioclasts:	Forams -			
		Bivalves -			
		Ostracods -			
		Gastropods -			
		Other -			
		Undiff -			
	Intraclasts:	Mud -			
	Peloids -				
	Ooids -				
	Other -				
MINERAL COMPOSITION (=100%)		Calcite -			
		Dolomite -	55		Pore filling and poikilotopic
		Sulfate -	35		
		Quartz -			
		Organics -	10		
					
12.5x CPL			12.5x PPL		

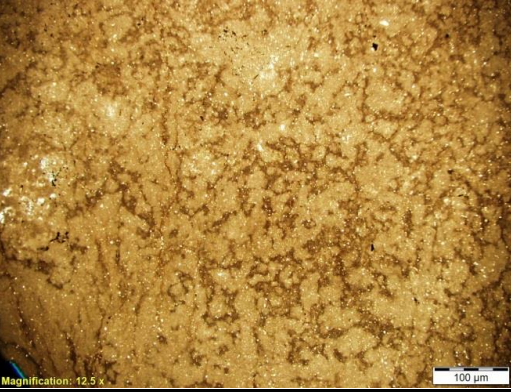
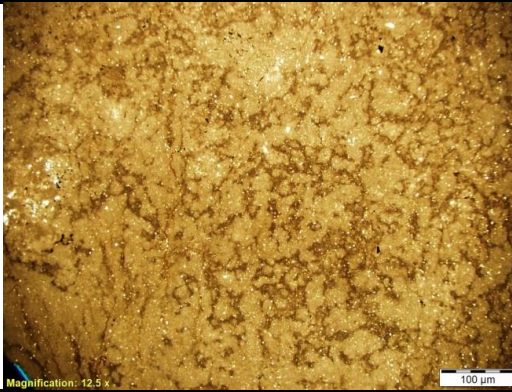
THIN SECTION #: I1-6116		LOCATION: Well # FCU 1947		Formation: upper Clear Fork	
DUNHAM CLASSIFICATION: Algal Laminated Ws					
GRAIN COMPOSITION			%	DESCRIPTION	
ALLO CHEMS:	Bioclasts:	Forams -		Very small angular grains	
		Bivalves -	5		
		Ostracods -			
		Gastropods -			
		Other -			
	Undiff -				
	Intraclasts:	Mud -			
		Peloids -			
		Ooids -			
		Other -			
MINERAL COMPOSITION (=100%)		Calcite -	40	Pore filling anhydrite	
		Dolomite -	25		
		Sulfate -	30		
		Quartz -			
		Organics -	5		
					
12.5x CPL				12.5x PPL	

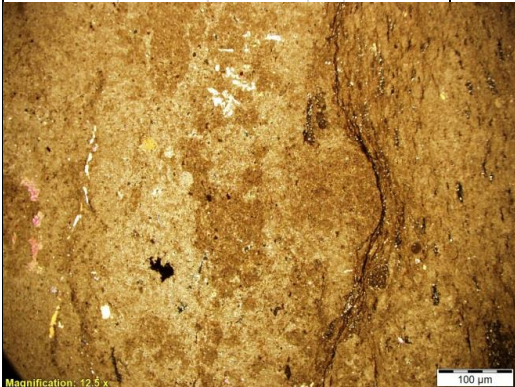
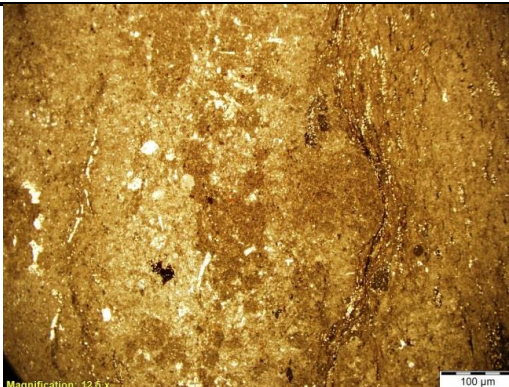
THIN SECTION #: I2-6120		LOCATION: Well # FCU 1947		Formation: upper Clear Fork	
DUNHAM CLASSIFICATION:		Intraclastic Ws			
GRAIN COMPOSITION			%	DESCRIPTION	
ALLO CHEMS:	Bioclasts:	Forams -		Angular	
		Bivalves -	5		
		Ostracods -			
		Gastropods -			
		Other -			
	Undiff -				
	Intraclasts:	Mud -			
	Peloids -	30	Peloids micritized prior to deposition		
	Ooids -	15	Ooids micritized prior to deposition		
	Other -				
MINERAL COMPOSITION (=100%)		Calcite -	40		
		Dolomite -	45		
		Sulfate -	5		
		Quartz -			
		Organics -	10		
					
12.5x CPL		12.5x PPL			

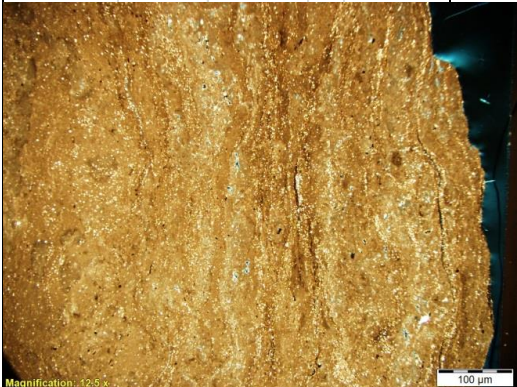
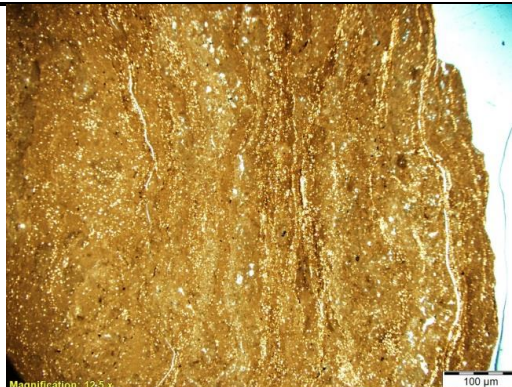
THIN SECTION #: I3-6143		LOCATION: Well # FCU 1947		Formation: upper Clear Fork	
DUNHAM CLASSIFICATION: Mottled Skeletal Ws					
GRAIN COMPOSITION			%	DESCRIPTION	
ALLO CHEMS:	Bioclasts:	Forams -		Highly angular and broken, some completely recrystallized	
		Bivalves -	15		
		Ostracods -	3		
		Gastropods -			
		Other -			
		Undiff -			
Intraclasts:	Mud -		Remnant peloids micritized and recrystallized		
	Peloids -	5			
	Ooids -				
	Other -				
MINERAL COMPOSITION (=100%)		Calcite -	35		
		Dolomite -	45		
		Sulfate -	5		
		Quartz -			
		Organics -	5		
					
12.5x CPL			12.5x PPL		

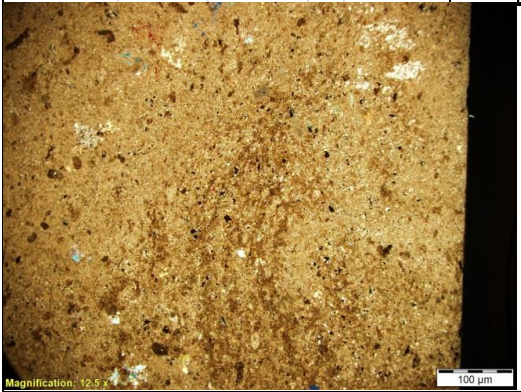
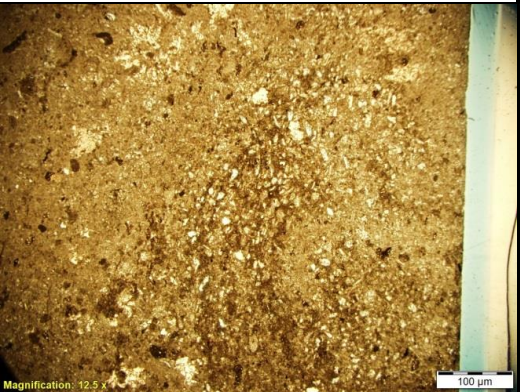
THIN SECTION #: K1-6117		LOCATION: Well # FCU 1947		Formation: upper Clear Fork	
DUNHAM CLASSIFICATION: Mottled Mudstone					
GRAIN COMPOSITION			%	DESCRIPTION	
ALLO CHEMS:	Bioclasts:	Forams -		Little to no grains	
		Bivalves -			
		Ostracods -			
		Gastropods -			
		Other -			
	Undiff -				
	Intraclasts:	Mud -			
		Peloids -			
		Ooids -			
		Other -			
MINERAL COMPOSITION (=100%)		Calcite -	40		
		Dolomite -	45		
		Sulfate -	5		
		Quartz -	7		
		Organics -	3		
					
Magnification: 12.5 x			Magnification: 12.5 x		
100 µm			100 µm		
12.5x CPL			12.5x PPL		

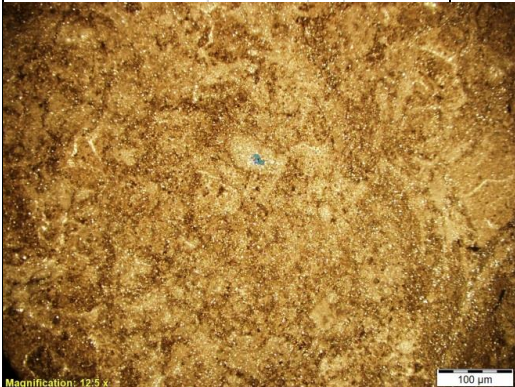
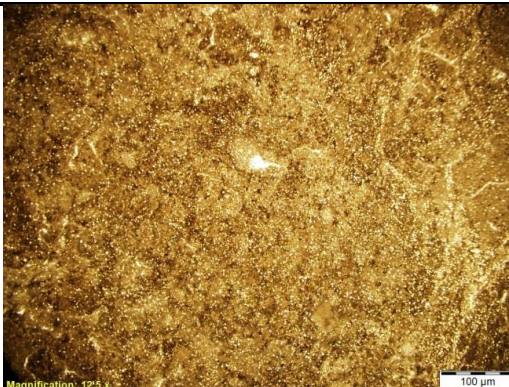
THIN SECTION #: K2-6126		LOCATION: Well # FCU 1947		Formation: upper Clear Fork	
DUNHAM CLASSIFICATION: Skeletal Ms/Ws					
GRAIN COMPOSITION			%	DESCRIPTION	
ALLO CHEMS:	Bioclasts:	Forams -	3	One uniserial foram found	
		Bivalves -	15	Highly angular and broken	
		Ostracods -	5	Thin shelled ostracods	
		Gastropods -			
		Other -			
		Undiff -			
Intraclasts:	Mud -				
	Peloids -				
	Ooids -				
	Other -				
MINERAL COMPOSITION (=100%)		Calcite -	40		
		Dolomite -	50		
		Sulfate -	5		
		Quartz -			
		Organics -	5		
					
12.5x CPL				12.5x PPL	

THIN SECTION #: L1-6125		LOCATION: Well # FCU 1947		Formation: upper Clear Fork		
DUNHAM CLASSIFICATION: Laminated Mottled Mudstone						
GRAIN COMPOSITION			%	DESCRIPTION		
ALLO CHEMS:	Bioclasts:	Forams -				
		Bivalves -				
		Ostracods -				
		Gastropods -				
		Other -				
	Intraclasts:	Undiff -				
		Mud -				
		Peloids -				
		Ooids -				
		Other -				
MINERAL COMPOSITION (=100%)		Calcite -	25			
		Dolomite -	50			
		Sulfate -	10			
		Quartz -	5			
		Organics -	10			
						
12.5x CPL			12.5x PPL			

THIN SECTION #: L2-6127		LOCATION: Well # FCU 1947		Formation: upper Clear Fork	
DUNHAM CLASSIFICATION: Laminated Mottled Ms/Ws					
GRAIN COMPOSITION			%	DESCRIPTION	
ALLO CHEMS:	Bioclasts:	Forams -			
		Bivalves -			
		Ostracods -			
		Gastropods -			
		Other -			
		Undiff -			
Intraclasts:	Mud -				
	Peloids -				
	Ooids -				
	Other -				
MINERAL COMPOSITION (=100%)		Calcite -	50		
		Dolomite -	30		
		Sulfate -	15		
		Quartz -			
		Organics -	5		
					
12.5x CPL				12.5x PPL	

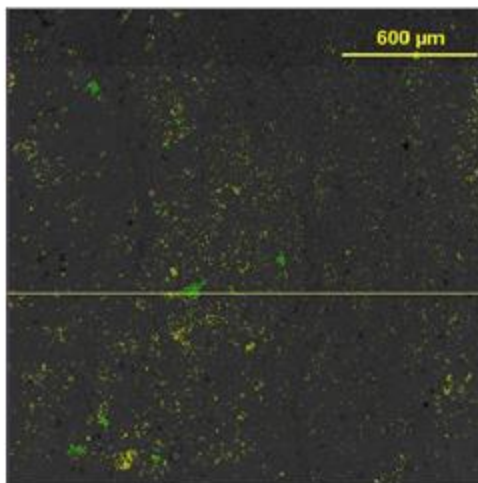
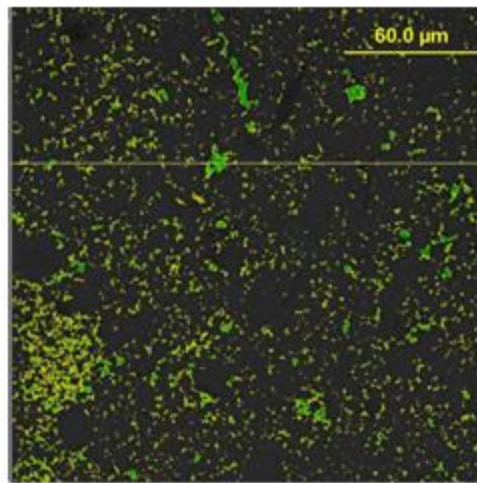
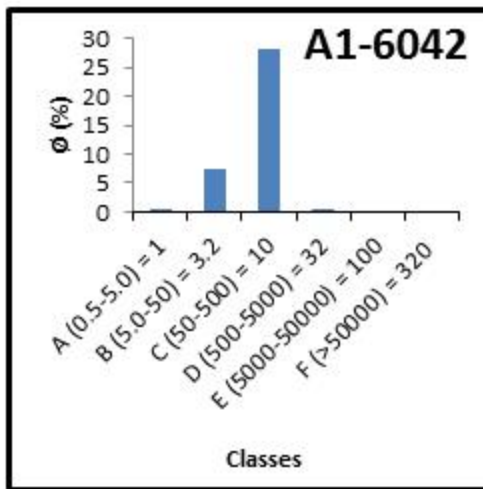
THIN SECTION #: L3-6134		LOCATION: Well # FCU 1947		Formation: upper Clear Fork		
DUNHAM CLASSIFICATION: Laminated Ms/Ws						
GRAIN COMPOSITION			%	DESCRIPTION		
ALLO CHEMS:	Bioclasts:	Forams -				
		Bivalves -				
		Ostracods -				
		Gastropods -				
		Other -				
	Intraclasts:	Undiff -				
		Mud -				
		Peloids -				
		Ooids -				
		Other -				
MINERAL COMPOSITION (=100%)		Calcite -	45			
		Dolomite -	35			
		Sulfate -	15			
		Quartz -				
		Organics -	5			
						
12.5x CPL			12.5x PPL			

THIN SECTION #: M1-6128		LOCATION: Well # FCU 1947		Formation: upper Clear Fork	
DUNHAM CLASSIFICATION: Algal Laminated Intraclastic Packstone					
GRAIN COMPOSITION			%	DESCRIPTION	
ALLO CHEMS:	Bioclasts:	Forams -			
		Bivalves -			
		Ostracods -			
		Gastropods -			
		Other -			
		Undiff -			
	Intraclasts:	Mud -			
	Peloids -	10	Small peloids micritized prior to deposition		
	Ooids -				
	Other -				
MINERAL COMPOSITION (=100%)		Calcite -	50		
		Dolomite -	20		
		Sulfate -	25		
		Quartz -			
		Organics -	5		
					
12.5x CPL				12.5x PPL	

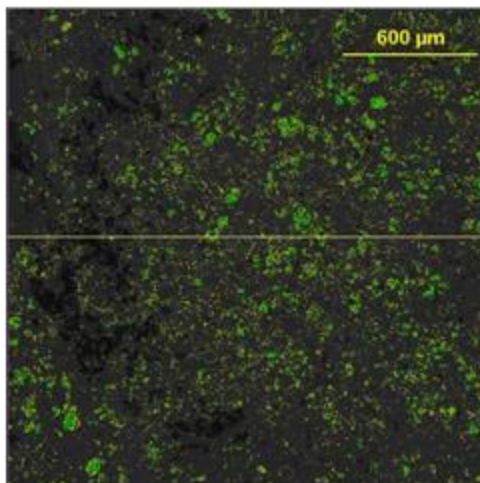
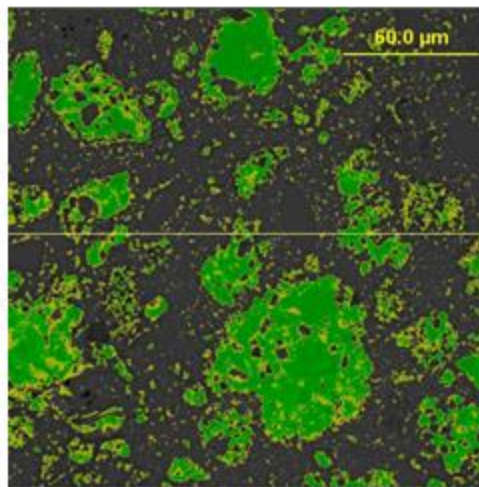
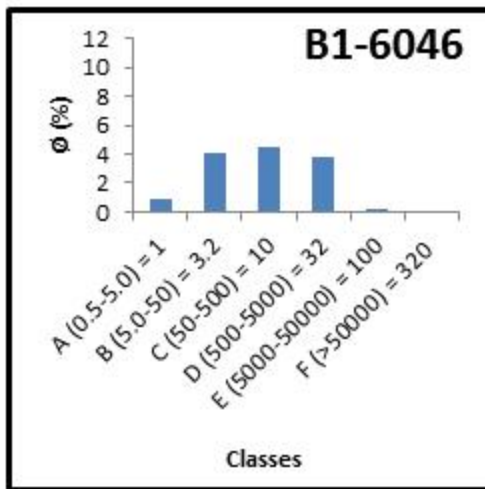
THIN SECTION #: M2-6134		LOCATION: Well # FCU 1947		Formation: upper Clear Fork		
DUNHAM CLASSIFICATION: Mottled Wackestone						
GRAIN COMPOSITION			%	DESCRIPTION		
ALLO CHEMS:	Bioclasts:	Forams -				
		Bivalves -				
		Ostracods -				
		Gastropods -				
		Other -				
		Undiff -				
	Intraclasts:	Mud -				
		Peloids -	10		Peloids destroyed from transport and diagenesis	
		Ooids -	5		Ooids destroyed from transport and diagenesis	
		Other -				
MINERAL COMPOSITION (=100%)		Calcite -	30			
		Dolomite -	30			
		Sulfate -	15			
		Quartz -	20			
		Organics -	5			
						
12.5x CPL			12.5x PPL			

Appendix B

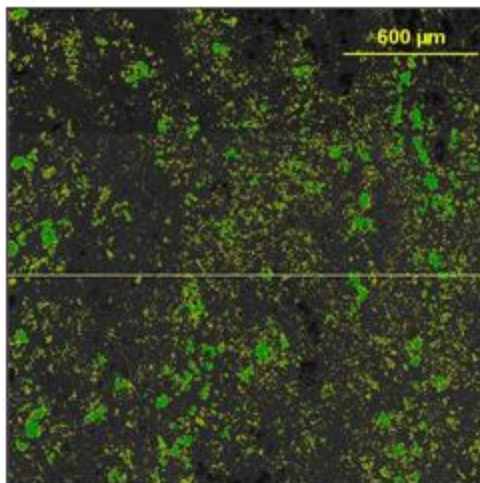
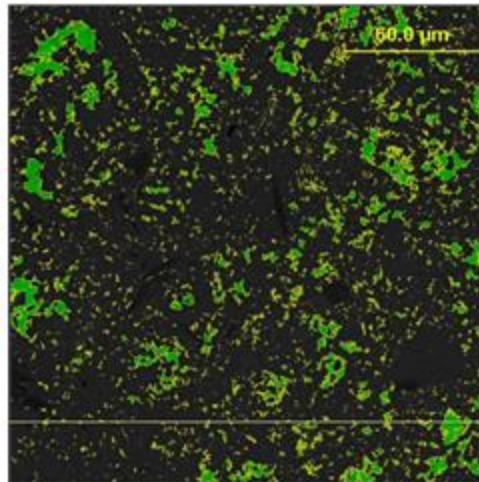
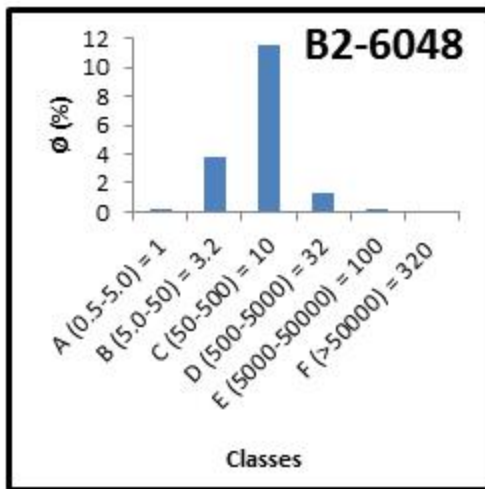
SEM Image Analysis Data



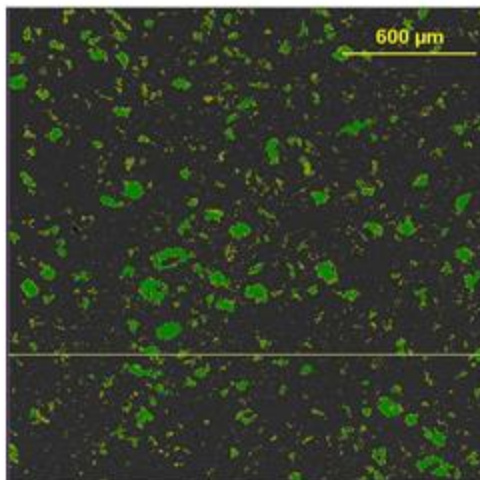
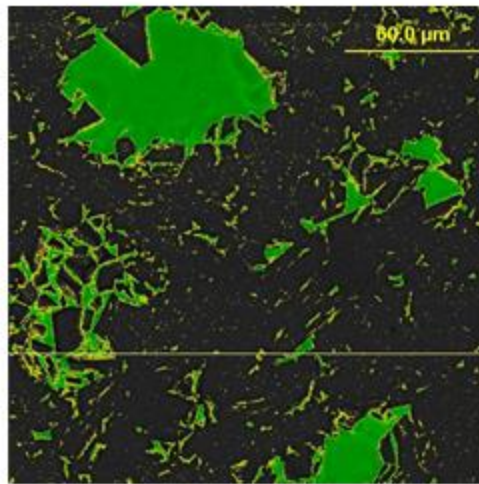
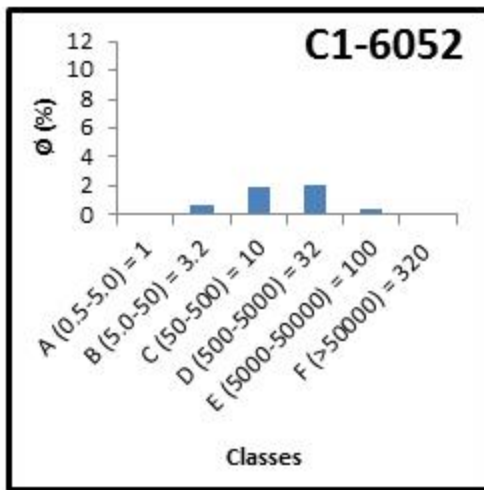
	Contribution	Shape Parameter
Microporosity	35.84%	3.923
Macroporosity	0.24%	1.983
Total Porosity	36.08%	3.874



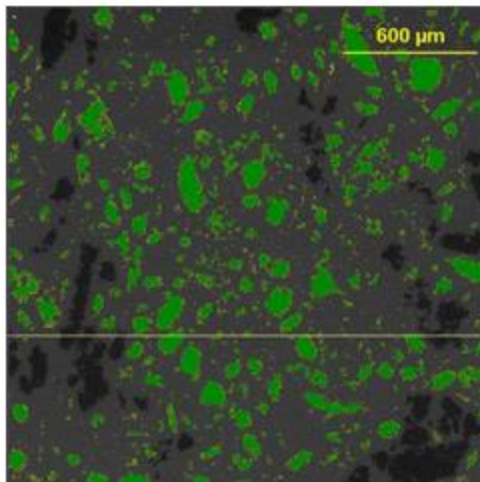
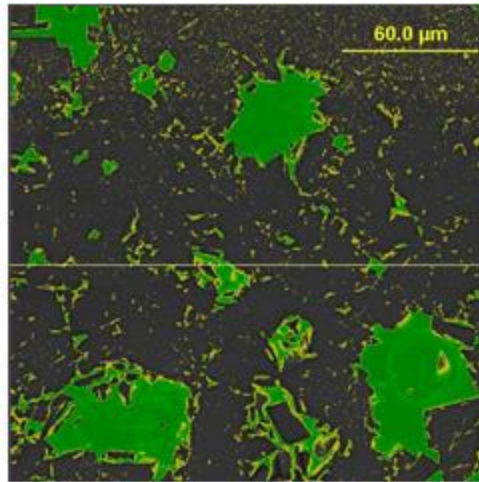
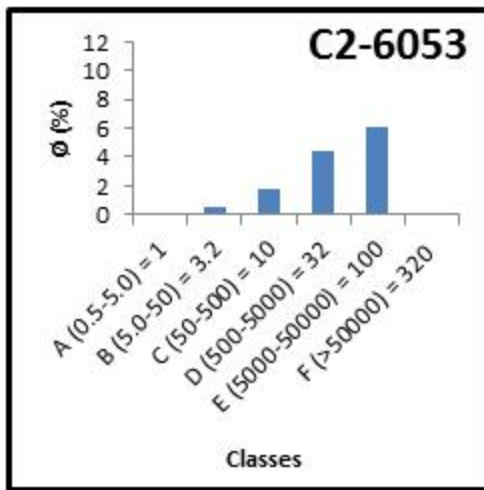
	Contribution	Shape Parameter
Microporosity	9.42%	1.996
Macroporosity	3.93%	2.049
Total Porosity	13.19%	2.005



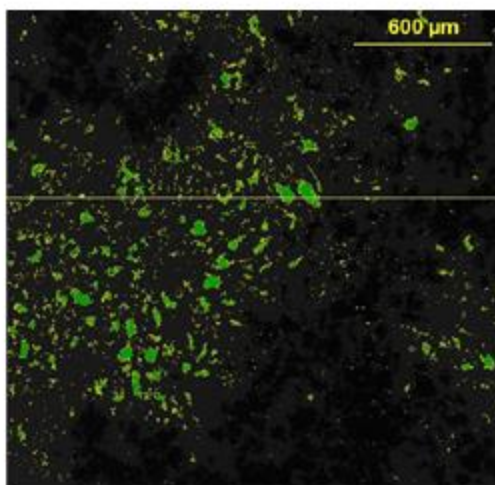
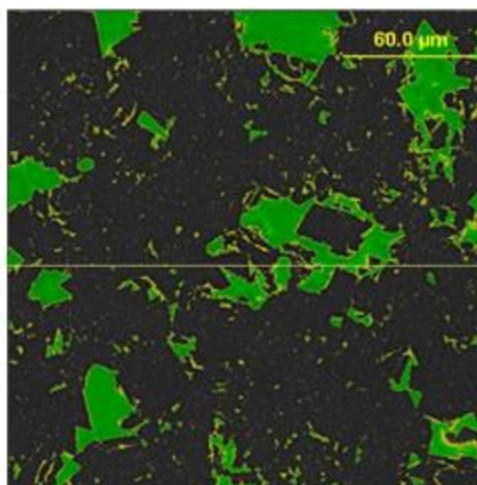
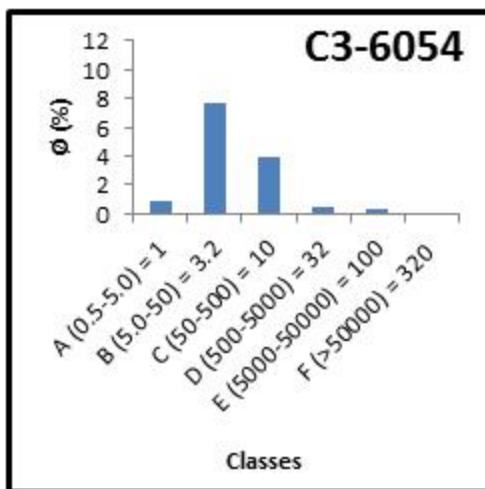
	Contribution	Shape Parameter
Microporosity	15.56%	3.831
Macroporosity	1.47%	1.587
Total Porosity	17.01%	3.833



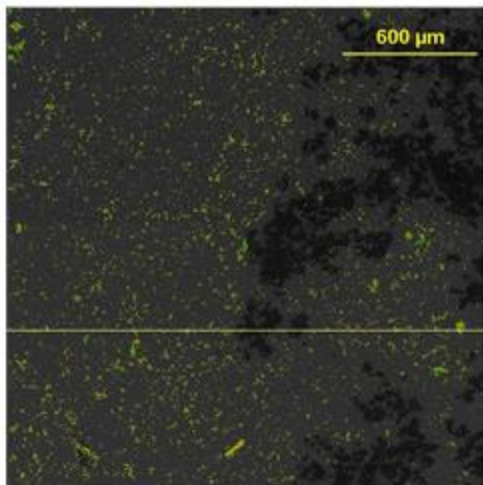
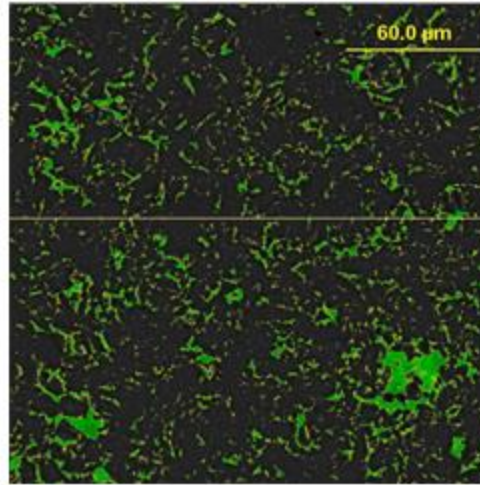
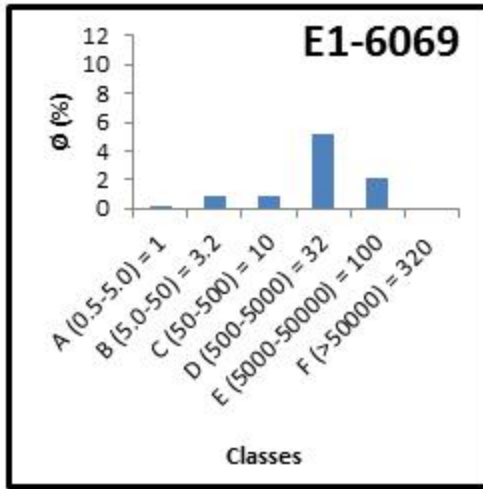
	Contribution	Shape Parameter
Microporosity	2.60%	1.849
Macroporosity	2.43%	1.761
Total Porosity	4.98%	1.780



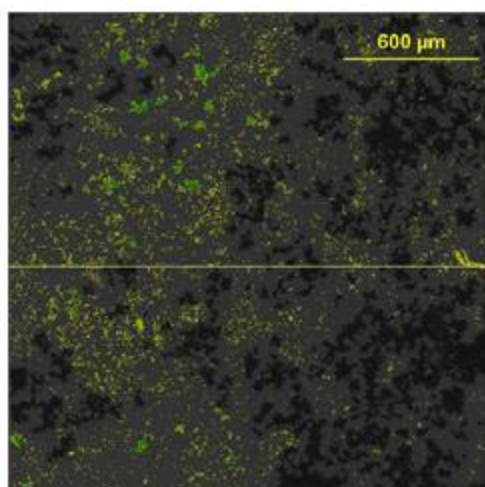
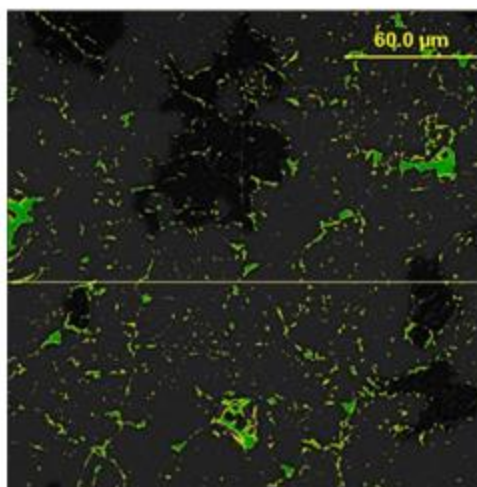
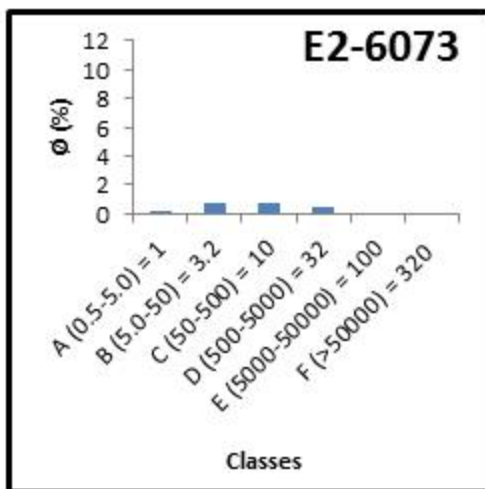
	Contribution	Shape Parameter
Microporosity	2.28%	1.869
Macroporosity	10.52%	1.866
Total Porosity	11.70%	1.866



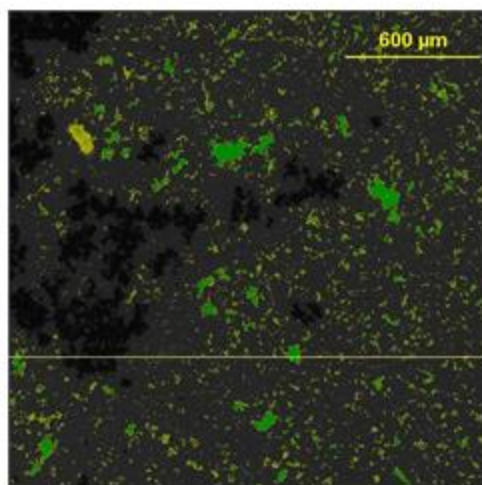
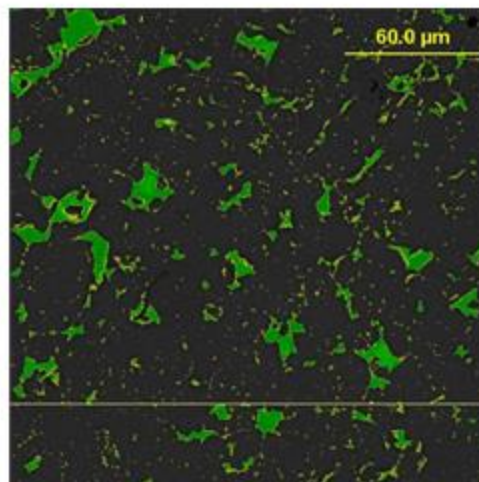
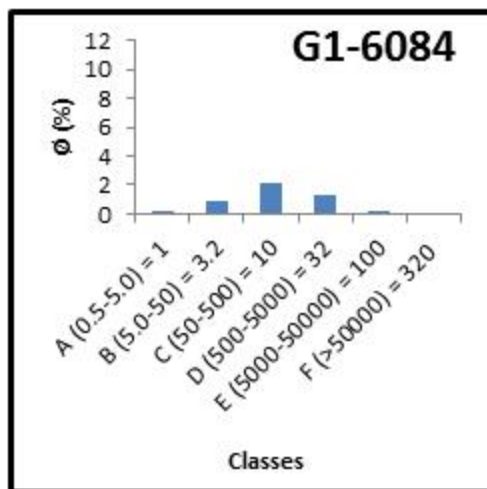
	Contribution	Shape Parameter
Microporosity	12.46%	3.160
Macroporosity	0.81%	1.956
Total Porosity	13.27%	2.921



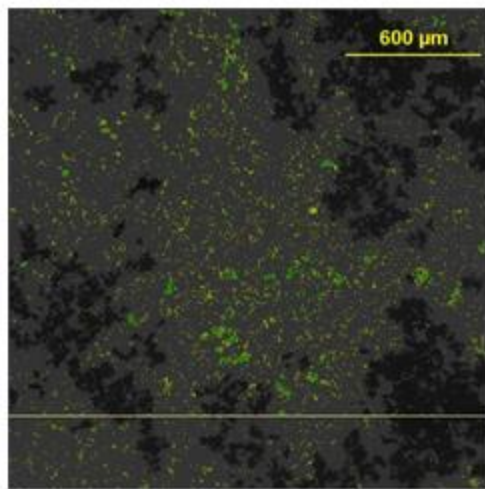
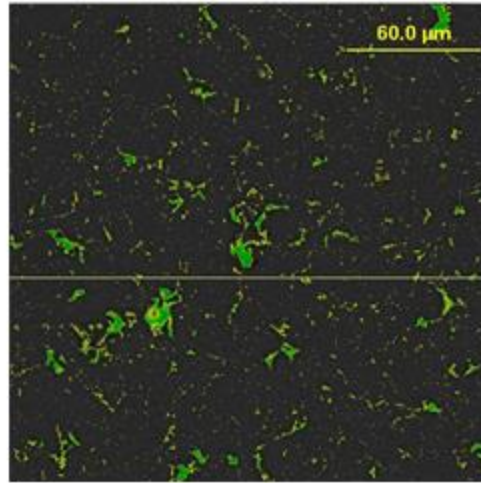
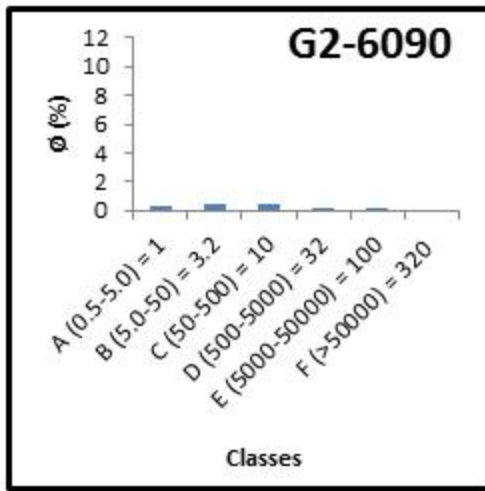
	Contribution	Shape Parameter
Microporosity	2.00%	1.812
Macroporosity	7.27%	3.662
Total Porosity	8.75%	3.541



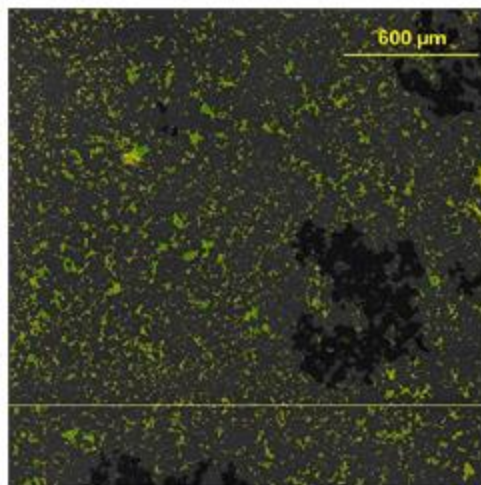
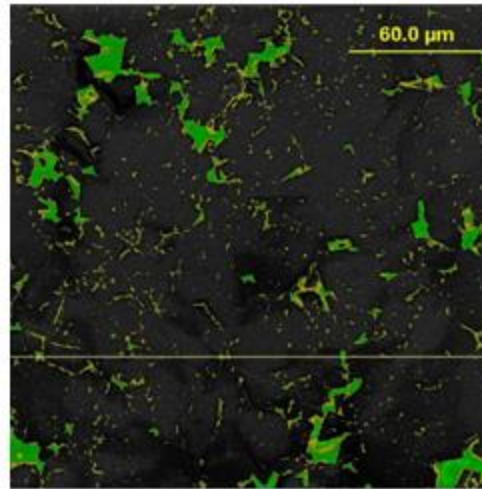
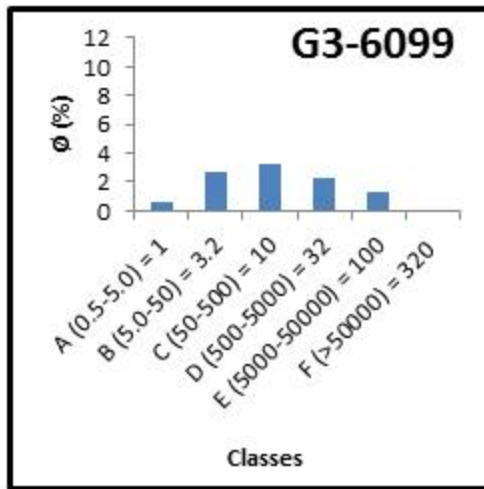
	Contribution	Shape Parameter
Microporosity	1.82%	1.961
Macroporosity	0.52%	2.027
Total Porosity	2.34%	1.993



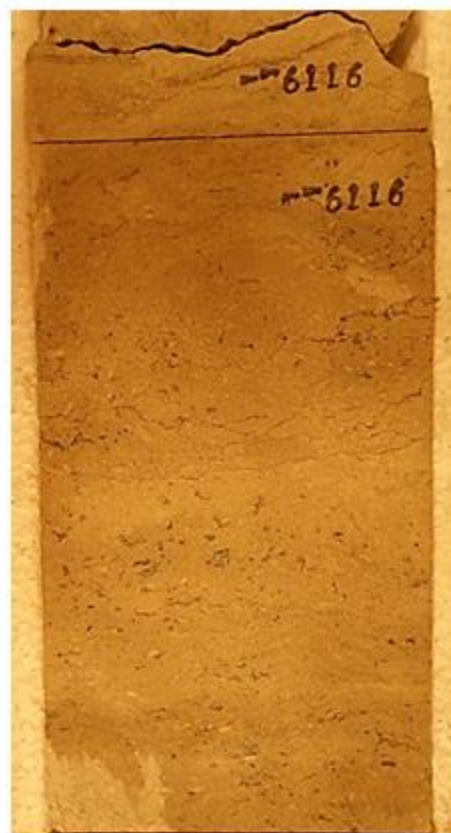
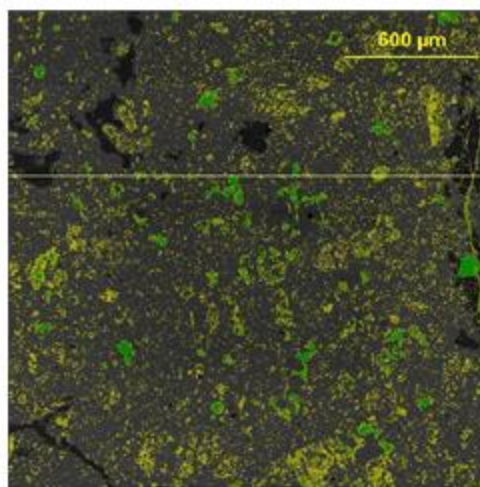
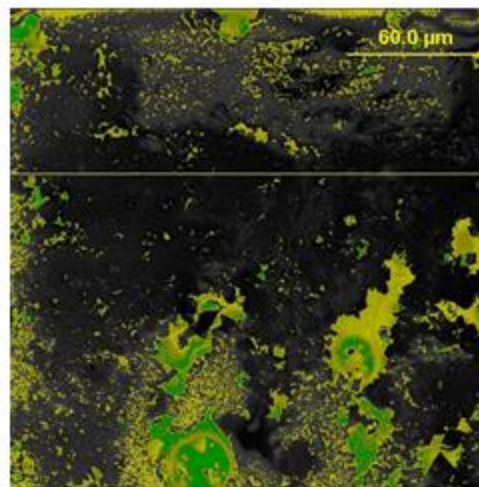
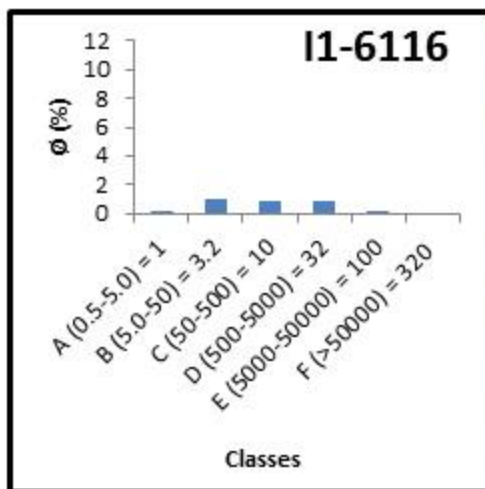
	Contribution	Shape Parameter
Microporosity	3.03%	1.758
Macroporosity	1.55%	2.131
Total Porosity	4.56%	2.011



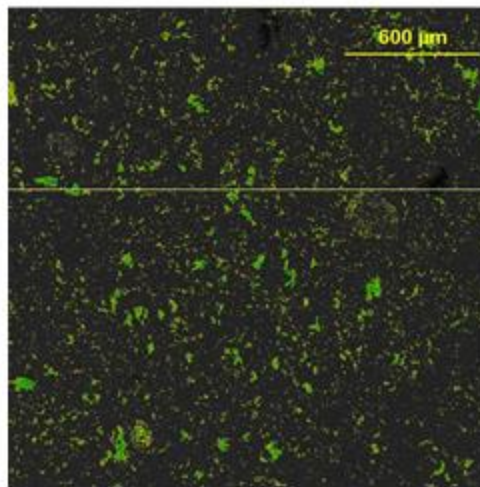
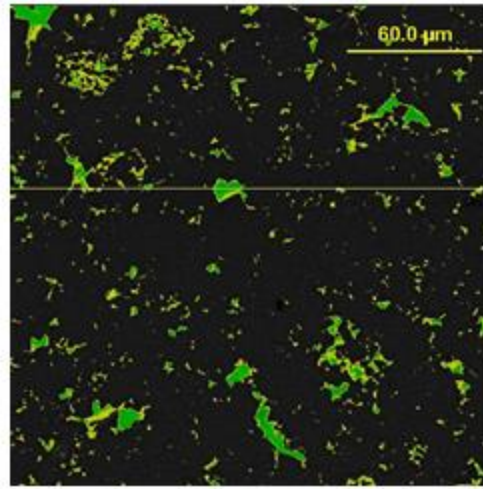
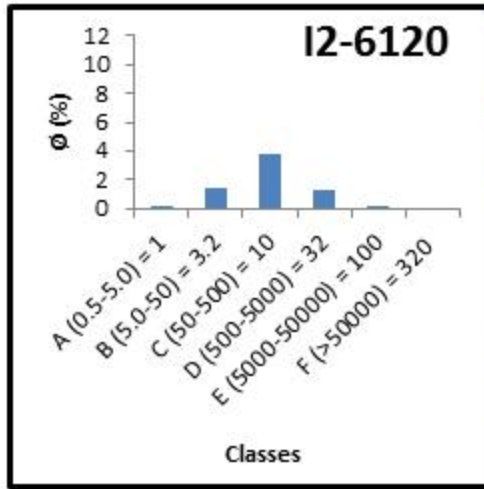
	Contribution	Shape Parameter
Microporosity	1.32%	2.633
Macroporosity	0.08%	2.704
Total Porosity	1.39%	2.646



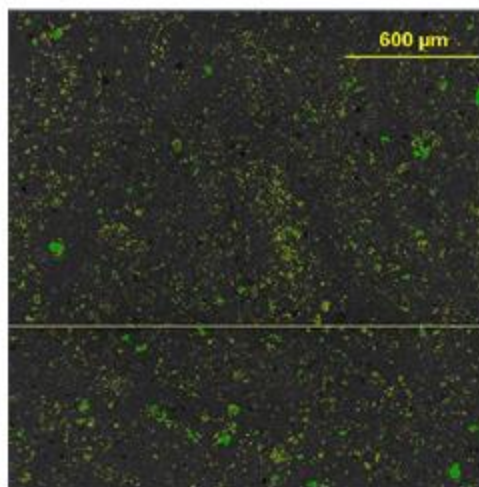
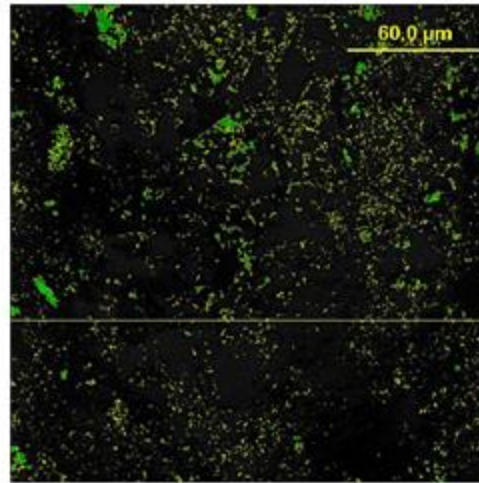
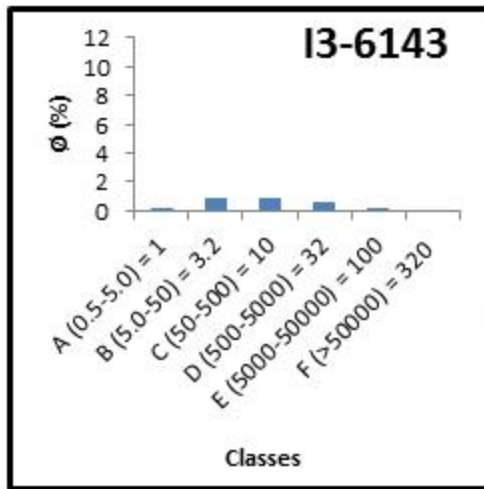
	Contribution	Shape Parameter
Microporosity	6.57%	2.053
Macroporosity	3.70%	2.368
Total Porosity	10.13%	2.270



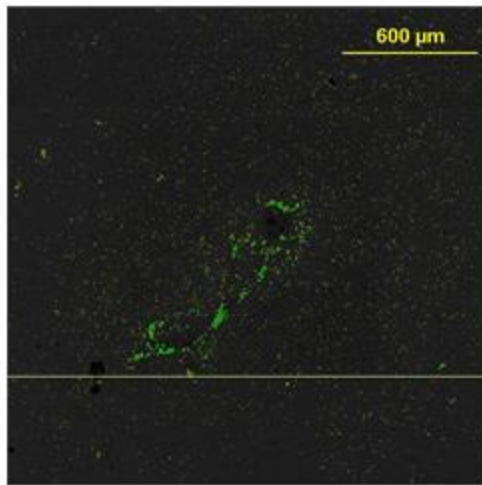
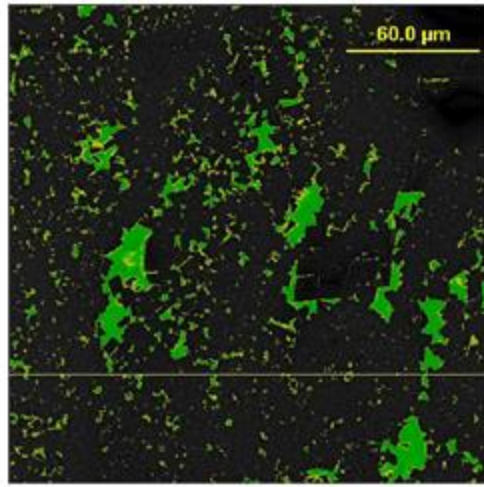
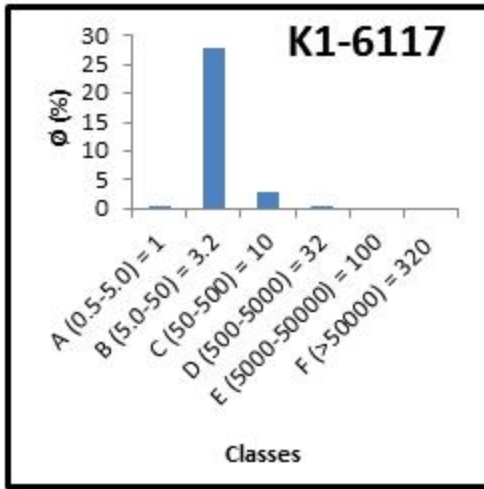
	Contribution	Shape Parameter
Microporosity	1.99%	1.815
Macroporosity	0.95%	2.285
Total Porosity	2.93%	2.156



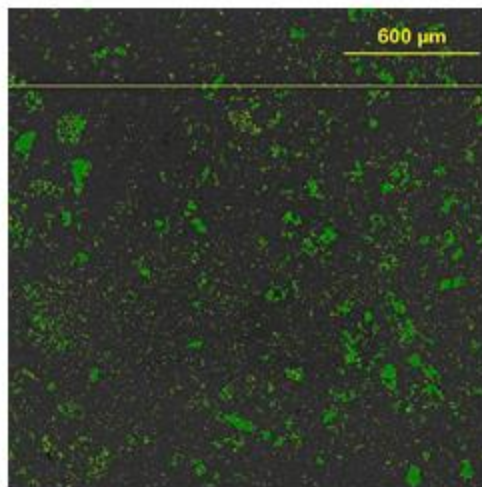
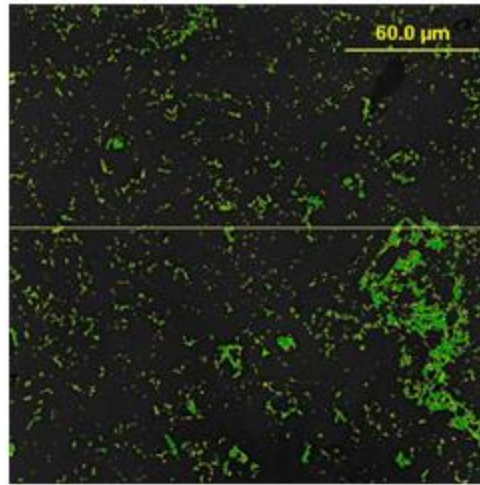
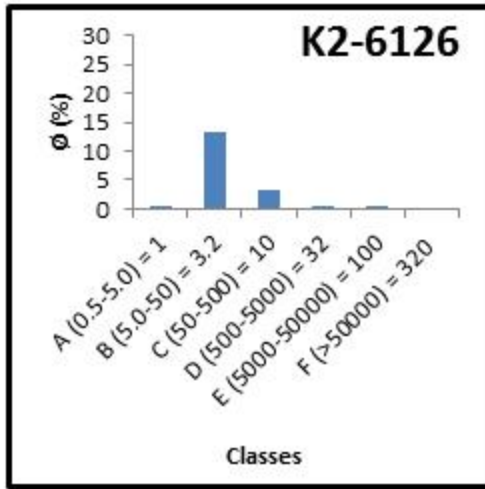
	Contribution	Shape Parameter
Microporosity	5.31%	3.019
Macroporosity	1.36%	2.063
Total Porosity	6.65%	2.535



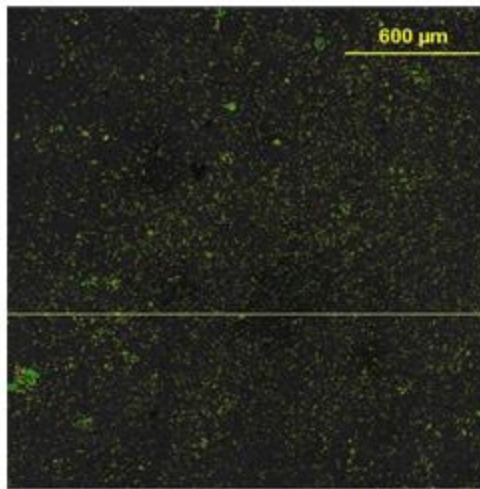
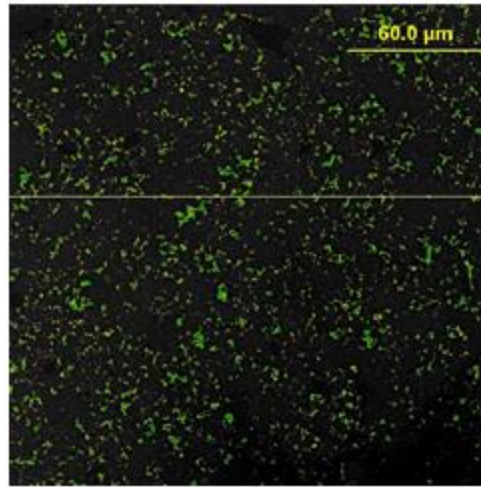
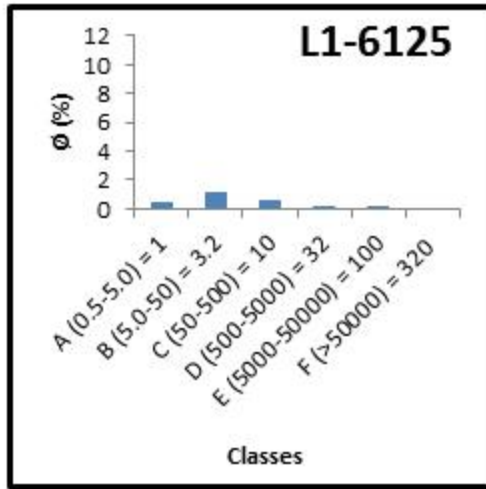
	Contribution	Shape Parameter
Microporosity	1.89%	2.053
Macroporosity	0.77%	2.209
Total Porosity	2.65%	2.149



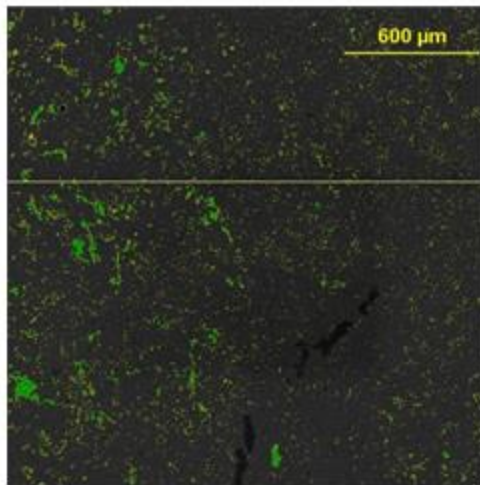
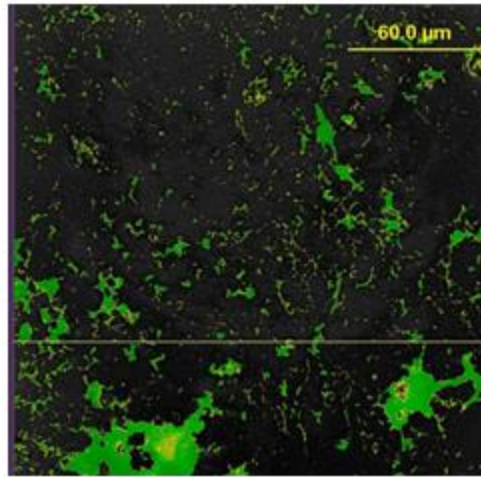
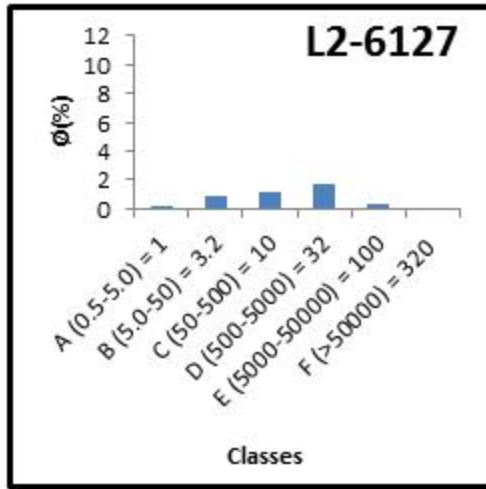
	Contribution	Shape Parameter
Microporosity	31.53%	2.747
Macroporosity	0.04%	2.033
Total Porosity	31.57%	2.742



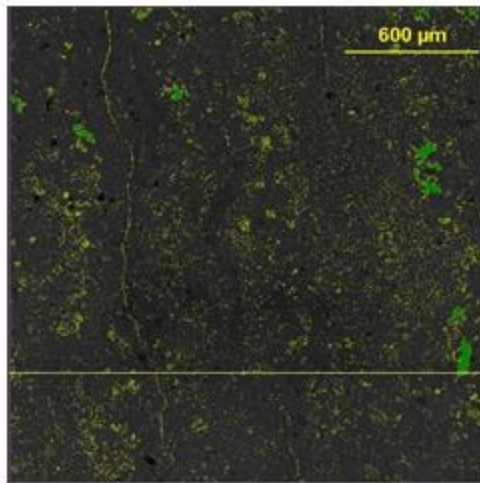
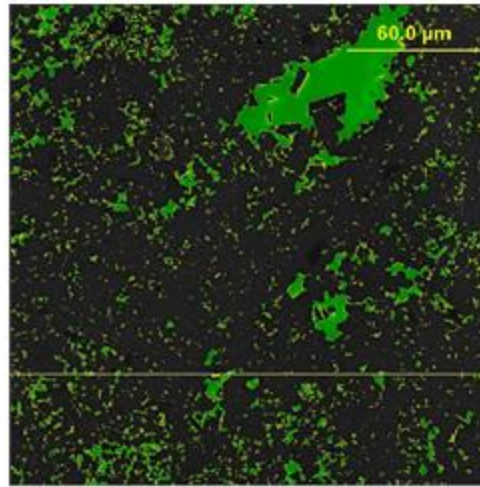
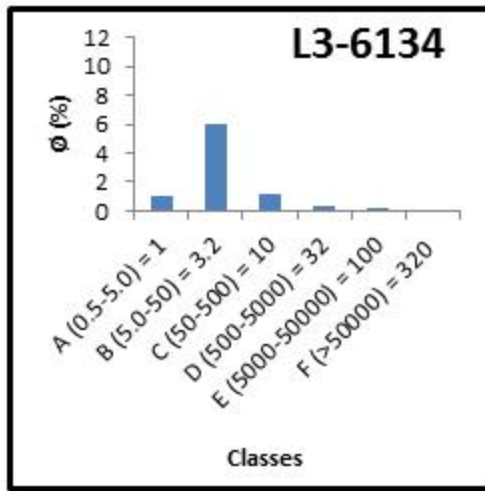
	Contribution	Shape Parameter
Microporosity	16.94%	2.834
Macroporosity	0.73%	1.758
Total Porosity	17.67%	2.677



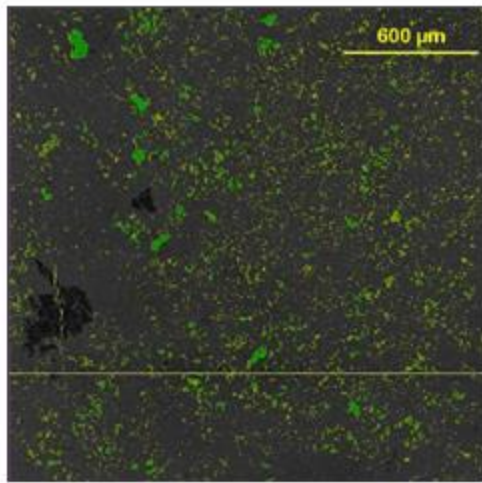
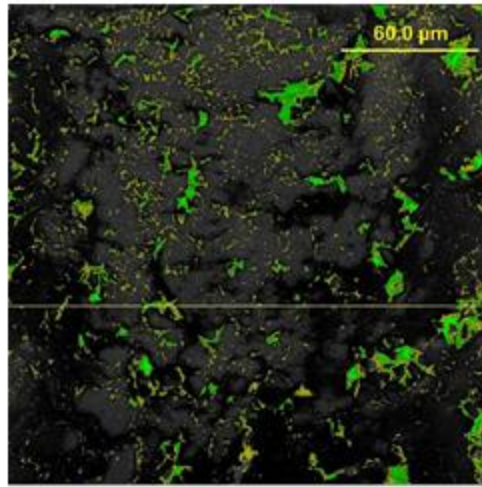
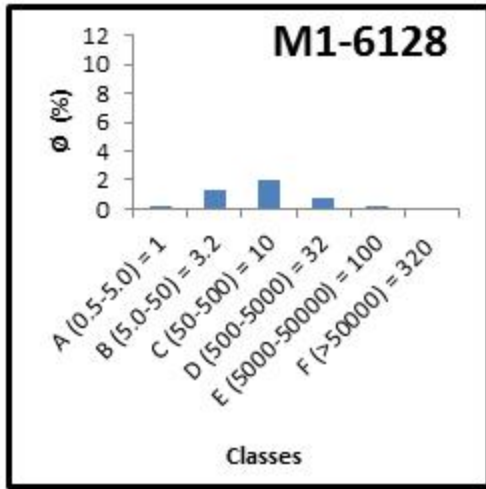
	Contribution	Shape Parameter
Microporosity	2.20%	2.121
Macroporosity	0.19%	1.875
Total Porosity	2.40%	2.060



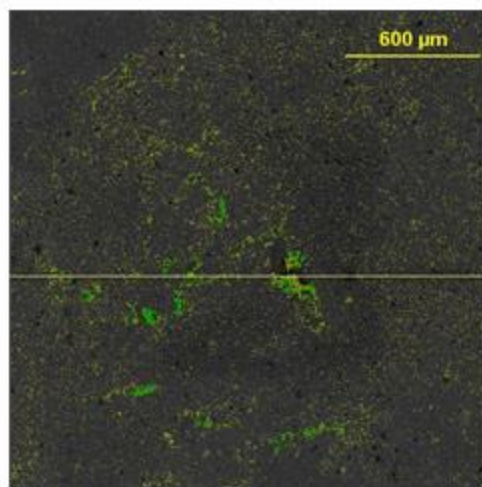
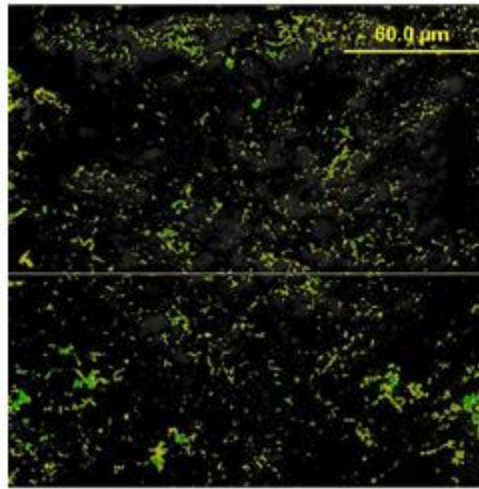
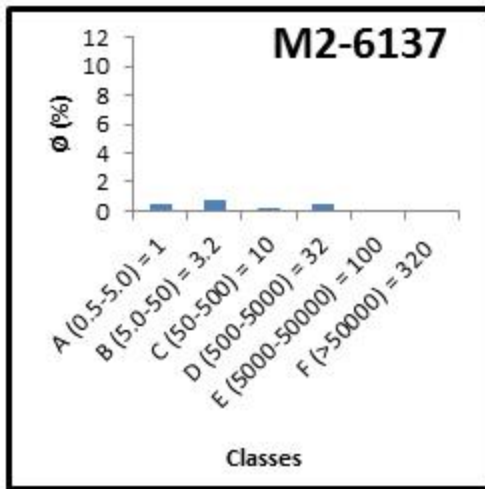
	Contribution	Shape Parameter
Microporosity	2.13%	1.859
Macroporosity	2.11%	1.922
Total Porosity	4.20%	1.909



	Contribution	Shape Parameter
Microporosity	8.27%	2.346
Macroporosity	0.30%	1.959
Total Porosity	8.57%	2.295



	Contribution	Shape Parameter
Microporosity	3.49%	1.807
Macroporosity	0.93%	1.731
Total Porosity	4.40%	1.768



	Contribution	Shape Parameter
Microporosity	1.46%	2.091
Macroporosity	0.50%	1.994
Total Porosity	1.96%	2.077

References

- Adams, D.C., and Keller, R.G., 1996, Precambrian Basement Geology of the Permian Basin Region of West Texas and Eastern New Mexico, A Geophysical Perspective, American Association of Petroleum Geologists Bulletin, V. 80, No. 3 (March 1996), P. 410–431.
- Ahr, W.M., 2008, Geology of Carbonate Reservoirs. The Identification, Description, and Characterization of Hydrocarbon Reservoirs in Carbonate Rocks, Wiley-Interscience, 280 P.
- Anselmetti, F.S., Luthi, S., and Eberli, G.P., 1998, Quantitative Characterization of Carbonate Pore Systems by Digital Image Analysis, American Association of Petroleum Geologists Bulletin, V. 82, No. 10 (October 1998), P. 1815- 1836.
- Archie, G.E., 1942, Electrical Resistivity Log as an Aid in Determining Some Reservoir Characteristics, Transactions of The American Institute of Mining, Metallurgical, and Petroleum Engineers, V. 146, P. 54-62.
- Armstrong, H.A. and Brasier, M.D., 2005, Microfossils, 2nd edition, Malden, Oxford, Carlton, Blackwell Publishing, 296P.
- Asquith, G.B., and Gibson, C.R., 1982, Basic well log analysis for geologists, American Association of Petroleum Geologists, Methods in Exploration No. 3, 216 P.

- Atchley, S.C., Kozar, M.G., and Yose, L.A., 1999, A Predictive Model for Reservoir Distribution in the Permian (Leonardian) Clear Fork and Glorieta Formations, Robertson Field Area, West Texas, American Association of Petroleum Geologists Bulletin, V. 83, No. 7, P. 1031-1056.
- Bane, R.K., Parker, R.A., Storbeck, W.G., and Sunde, R.L., 1994, Reservoir management of the Fullerton Clearfork Unit: SPE Permian Basin oil & gas recovery conference, Society of Petroleum Engineers 27640, P. 259-274.
- Blakey, R., 2013, Regional Paleogeography, North American Paleogeography, Middle Permian (275Ma): <http://www2.nau.edu/rcb7/namP275.jpg>
- Choquette, P.W., and Pray, L.C., 1970, Geologic nomenclature and classification of porosity in sedimentary carbonates, American Association of Petroleum Geologists Bulletin V. 54 (2), P. 207-250.
- Dickson, J.A.D., and Saller, A.H., 1995, Identification of subaerial exposure surfaces and porosity preservation in Pennsylvanian and Lower Permian shelf limestones, eastern Central Basin platform, Texas: *In* Budd, D.A. Saller, A.H., and Harris, P.M., eds., Unconformities in carbonate strata—their recognition and the significance of associated porosity, American Association of Petroleum Geologist Memoir 57, P. 239–257.
- Dumble, E.T., and Cummins, W.F., 1890, Texas Geological Survey First Annual Report, 188 P.

- Dunbar, C.O., Baker, A.A., Cooper, G.A., King, P.B., McKee, E.D., Miller, A.K., Moore, R.C., Newell, N.D., Romer, A.S., Sellards, E.H., Skinner, J.W., Thomas, H.D., and Wheeler, H.E., 1960, Correlation of the Permian formations of North America, Geological Society of America Bulletin, V. 71, P. 1763-1806.
- Dunham, R.J., 1962, Classification of carbonate rocks according to texture: *In* Ham, W.E., ed., Classification of carbonate rocks—a symposium, American Association of Petroleum Geologists Memoir 1, P. 108–121.
- Ehrlich, R., Crabtree, S.J., Kennedy, S.K., and Cannon, R.L., 1984, Petrographic image analysis I; analyses of reservoir pore complexes, Journal of Sedimentary Petrology, V. 54, P. 1365–1376.
- Ehrlich, R., Crabtree, S.J., Horkowitz, K.O, and Horkowitz, J.P., 1991(a), Petrography and reservoir physics III: physical models for permeability and formation factor: American Association of Petroleum Geologists Bulletin, V. 75, P. 1547–1562.
- Ehrlich, R., Crabtree, S.J., Horkowitz, K.O, and Horkowitz, J.P., 1991(b), Petrography and reservoir physics III: physical models for permeability and formation factor: American Association of Petroleum Geologists Bulletin, V. 75, P. 1579–1592.
- Flügel, E., 2010, Microfacies of Carbonate Rocks, second edition, Springer-Verlag Berlin, Germany, 984 P.

Gerard, R.E., Philipson, C.A., Manni, F.M. and Marshall, D.M., 1992, Petrographic image analysis: an alternate method for determining petrophysical properties: *In* Palaz, I., and Sengupta, S.K., eds., Automated pattern analysis in petroleum exploration, New York, Springer Verlag, P. 249–263.

Hanford, C.R., 1981, Sedimentology and genetic stratigraphy of Dean and Spraberry Formations (Permian), Midland Basin, Texas, American Association of Petroleum Geologists Bulletin, V. 65, P. 1602-1616.

Hardie, L., 1967, The Gypsum-Anhydrite Equilibrium At One Atmosphere Pressure, American Mineralogist, V. 52, P. 171-200.

Harrington, R.R., and Lucia, J.F., 2011, Integration of Rock Fabrics and Stratigraphy for Petrophysical Quantification of reservoir framework: *In* Ruppel, S.C., Lucia, F.J., Harrington, R.R., Wang, F., Zeng, H., Kane, J. and Jennings Jr, J.W., eds., Anatomy of a giant carbonate reservoir; Fullerton Clear Fork (Lower Permian) field, Texas: Studies in Geology No. 63, P. 1-18.

Lonoy, A., 2006, Making sense of carbonate pore systems, American Association of Petroleum Geologists Bulletin, V. 90, P. 1381-1405.

Lucia, F.J., 1972, Recognition of evaporite-carbonate shoreline sedimentation, p. 160-191: *In* Rigby, J .K., and Hamblin, W.K., eds., Recognition of ancient sedimentary environments, Society Economic Paleontologists and Mineralogists Special Publication No.16, 340 P.

Lucia, F.J., 1999, Carbonate reservoir characterization, New York, Springer Verlag, 226 P.

Lucia, F.J., and Major, R.P., 1994, Porosity evolution through hypersaline reflux dolomitization: *In* Purser, B.H., Tucker, M.E., and Zenger, D.H., eds., Dolomites, a volume in honour of Dolomieu, International Association of Sedimentologists, Special Publication No. 21, P. 325–341.

Lucia, F.J., Kerans, C., and Jennings, Jr., J.W., 2003, Carbonate Reservoir Characterization, Society of Petroleum Engineers, P. 70-72.

Lucia, F.J., Jones, R.H., and Jennings, J.W., 2004, Poikilotopic anhydrite enhances reservoir quality, American Association of Petroleum Geologists 2004 Annual Convention, Abstracts, V. 13, P. A88.

Lucia, F.J., Ruppel, S.C., Jones, R.H., Kane, J.A., Wang, Fred, and Hongliu, Z., 2006, Reservoir characterization of the Fullerton Clear Fork field, Andrews County, Texas: *In* Slatt, R.M., Rosen, N.C., Bowman, M., Castagna, J., Good, T., Loucks, R., Latimer, R., Scheihing, M., and Smith, R., eds., Reservoir characterization-integrating technology and business practices, Proceedings of the 26th Annual GCS Society for Sedimentary Geology Foundation Bob F. Perkins Research Conference, P. 651–683.

Mazzullo, S.J., 1982, Stratigraphy and depositional mosaics of lower Clear Fork and Wichita groups (Permian), northern Midland Basin, Texas, American Association of Petroleum Geologists Bulletin, V. 66, P. 210-227.

Mazzullo, S.J. 1995, Permian stratigraphy and facies, Permian Basin (Texas-New Mexico) and adjoining areas in the Midcontinent United States: *In* Scholle, P.A., ed., The Permian of northern Pangea; V. 2, Sedimentary basins and economic resources, P. 41-60.

McCreech, C.A., Ehrlich, R., and Crabtree, S.J., 1991, Petrography and reservoir physics II-relating thin section porosity to capillary pressure, the association between pore types and throat size, American Association of Petroleum Geologists Bulletin, V. 75, P. 1563–1578.

Montgomery, S.L., 1998, Permian Clear Fork Group, North Robertson Unit: Integrated Reservoir Management and Characterization for Infill Drilling, Part 1-Geologic Analysis, American Association of Petroleum Geologists Bulletin, V. 82, No. 10 (October 1998), P. 1797-1814.

Mosley, B.R., 1990, Deposition and diagenesis of the upper Clear Fork (Leonardian) shelf margin, Palm Sunday Field, Hockley County, Texas (THESIS), The University of Texas at Arlington, 171 P.

No Author, 1998, Fullerton Field - Lower Permian Wichita and Clear Fork Formations, Dolomitised Shoal Grainstones and Lagoonal Lime Mudstones, Proprietary Field Evaluation Report conducted by C&C Reservoirs© for XTO Energy, 33 P.

Presley, M.W., and McGillis, K.A., 1982, Coastal Evaporites and Tidal Flat Sediments of the Upper Clear Fork and Glorieta Formations, Texas Panhandle, University of Texas at Austin, Bureau of Economic Geology Report of Investigations Number 115, 50 P.

Ruppel, S.C., 1992, Styles of deposition and diagenesis in Leonardian reservoirs in west Texas: Implications for improved reservoir characterization, Society of Petroleum Engineers Annual Exhibition and Technical Conference, SPE Paper 24691, P. 313-320.

Ruppel, S.C., 2002, Geologic controls on reservoir development in a Leonardian (Lower Permian) carbonate platform reservoir, Monahans field, west Texas, University of Texas at Austin, Bureau of Economic Geology, Report of Investigations 266, 58 P.

Ruppel, S.C., 2004, Multidisciplinary Imaging of Rock Properties in Carbonate Reservoirs for Flow-Unit Targeting, Final Technical Report, Prepared for U.S. Department of Energy Under Contract No. DE-FC26-01BC15351, 342 P.

Ruppel, S.C., Ward, W.B., Ariza, E.E., and Jennings, J.W. Jr., 2000, Cycle and sequence stratigraphy of Clear Fork reservoir-equivalent outcrops, Victorio Peak Formation,

Sierra Diablo, Texas: *In* Lindsay, R., Trentham, R., Ward, R.F., and Smith, A.H., eds., Classic Permian geology of west Texas and southeastern New Mexico, 75 years of Permian basin oil and gas exploration and development, West Texas Geological Society Publication 108, P. 109-130.

Ruppel, S.C., and Ariza, E.E., 2002, Cycle and sequence stratigraphy of the clear fork reservoir at South Wasson field: Gaines County, Texas: *In* Lucia, F.J. ed., Integrated outcrop and subsurface studies of the interwell environment of carbonate reservoirs: Clear Fork (Leonardian-age) reservoirs, West Texas and New Mexico, Final technical report to the Department of Energy, Contract No. DE-AC26-98BC15105, P. 59-94.

Ruppel, S.C., and Jones, R.H., 2006, Key role of outcrops and cores in carbonate reservoir characterization and modeling, Lower Permian Fullerton field, Permian basin, United States: *In* Harris, P.M., and Weber, L.J. eds., Giant hydrocarbon reservoirs of the world: From rocks to reservoir characterization and modeling: American Association of Petroleum Geologists Memoir 88/Society for Sedimentary Geology Special Publications, P. 355-394.

Ruppel S.C., 2006, Description and Analysis of Cored Wells in the Russell Clear Fork Reservoir, Gaines County, Texas, Bureau of Economic Geology, 62 P.

Saller, A.H., Dickson, J. A.D., and Boyd, S.A., 1994, Cycle stratigraphy and porosity in Pennsylvanian and Lower Permian shelf limestones, eastern Central Basin

platform, Texas, American Association of Petroleum Geologists Bulletin, V. 78, P. 1820–1842.

Saller, A.H., and Henderson, N., 1998, Distribution of porosity and permeability in platform dolomites: insight from the Permian of west Texas, American Association of Petroleum Geologists Bulletin, V. 82, P. 1528-1550.

Scholle, P.A., Bebout, D.G., Moore, C.H., 1983, Carbonate Depositional Environments: Chapter 4: American Association of Petroleum Geologists Memoir 33, P. 171-210.

Scholle, P.A., and Ulmer-Scholle, D.S., 2003, A Color Guide to the Petrography of Carbonate Rocks: Grains, Textures, Porosity, Diagenesis, American Association of Petroleum Geologists Memoir 77, 474 P.

Shields, M.J., and Brady, P.V., 1995, Mass balance and fluid flow constraints on regional-scale dolomitization, Late Devonian, Western Canada Sedimentary Basin, Bulletin of Canadian Petroleum Geology, V. 43, P. 371-392.

Shinn, E.A., 1968, Practical significance of birdseye structures in carbonate rocks, Journal of Sedimentary Petrology, V. 38, P. 215-223.

Shinn, E.A., 1986, Modern carbonate tidal flats: their diagnostic features, Colorado School of Mines Quarterly, V. 81, P. 7–35.

Silver, B.A., and Todd, R.G., 1969, Permian Cyclic strata, northern Midland and Delaware basins, west Texas and southeast New Mexico, American Association of Petroleum Geologists Bulletin, V. 53, P. 2223-2251.

Sun, Q.S., 1995, Dolomite Reservoirs: Porosity Evolution and Reservoir Characteristics, American Association of Petroleum Geologists Bulletin, V. 79, No. 2 (February 1995), P. 186-204.

Wright, V.P., 1984, Peritidal carbonate facies models; a review, Geological Journal, V. 19, P. 309–325.

XTO Energy a subsidiary of ExxonMobil, 2012-2013, Information and data gathered from communication with company employees, as well as the use of company production reports, software, maps, cross sections, and other data.

Yang, K.M., and Dorobek, S.L., 1995, The Permian Basin of West Texas and New Mexico: Tectonic history of a 'composite' foreland basin and its effects on stratigraphic development: *In* Dorobek, S.L., and Ross, G.M., eds., Stratigraphic evolution of foreland basins, Society for Sedimentary Geology Special Publication, No. 52, P. 149-174.

Biographical Information

Tore Wiksveen is a graduate student at the University of Texas Arlington and will have graduated as of December 2013. Tore attended Florida Atlantic University for his undergraduate career where he obtained a Bachelor of Science degree in Geology. After completing his undergraduate studies he moved to Fort Worth, TX to follow his passion in the energy industry. He began working for μ Energy in January of 2011 and has been a year round intern since. Most of his work at XTO deals with petroleum systems of the Permian Basin. He holds a particular interest in shallow-water carbonate oil fields on the Central Basin Platform such as the one in his thesis work. In the spring of 2013 he received a scholarship from the Fort Worth Geological Society for his thesis work which pertains directly to the energy industry, and hydrocarbon production. Tore's future plans are to continue working in the energy industry where he can do what he loves while providing a great life for his family and friends.